Atomistic simulation and electron microscopy to characterize grain boundaries in doped β-tricalcium phosphate ceramics

Gabrielle Anne Laguisma SBLENDORIO

Acknowledgements

Abstract

The limitations and potential complications correlated with autogenous bone grafts have raised interest in the development of synthetic bone graft substitutes. β-tricalcium phosphate (β-TCP, $Ca_3(PO_4)_2$) is one of the most promising materials for synthetic bone graft substitutes because it is readily resorbed and replaced by new bone. However, even though β-TCP has been clinically used since 1920, various studies have reported inconsistent biological responses for this bioceramic. This is most likely because the mechanisms by which β-TCP is resorbed into the human body are still far from being completely understood. In order to better understand the *in vivo* behavior of β-TCP, this thesis sets out to explore aspects of grain boundaries and ion-doping in β-TCP via atomistic simulations and electron microscopy. The knowledge gained from this aims towards achieving a better understanding of how they in turn influence the resorption and healing processes of β-TCP bone graft substitutes.

For correct atomistic simulations, the β-TCP crystal lattice presents a particular challenge, in that there is an incommensurate aspect of its structure tied to a specific, partially-filled calcium site in the conventionally-defined unit cell. Before considering the simulations of doped structures and interfaces, detailed molecular dynamics and Monte Carlo atomistic simulations are made in order to study the arrangements of calcium ion occupations of this site, going from the scale of the unit cell up to large supercell systems.

The β-TCP crystal structure contains five unique Ca sites in the unit cell, with the Ca(4) site being 50% partially occupied. It therefore presents twenty possible unit cell configurations. Using molecular dynamics simulations, the twenty configurations could be categorized into three energetic classes: the low (LEC), intermediate (IEC), and high (HEC) energy configurations. These energetic classes were found to be in agreement with previous computational studies. However, different combinations of the three energetic unit cell types into supercell systems presented roughly equivalent energies as a supercell solely composed of the LEC unit cell. The conclusion was that the Ca(4) site of the β-TCP structure cannot be adequately described with a single unit cell description.

This was further studied by considering unit cells with varying Ca(4) occupancy. The 50% occupancy of the Ca(4) site was maintained on the level of the supercell with proper combinations of variable Ca(4) unit cells in a 3D-checkerboard arrangement. This

presented domains of occupancy that could be energetically-related to changes in the a-and c-lattice parameters, an effect that could be correlated to experimental findings. Monte Carlo (MC) simulations were then used to check if any bias was introduced to the chosen checkerboard arrangements by sampling much larger supercells. In the subsequent MC simulations, no long-range order or patterning of the partially occupied Ca(4) was observed. Rather, the Ca(4) sites appear to be randomly occupied, but on the scale of the supercell, not the individual unit cell — explaining to some degree the incommensurate nature of the X-ray and neutron diffraction results.

Following this analysis, I treat the question of dopant behavior in the bulk lattice and interface structures (surfaces, grain boundaries). A framework is detailed for simulating β-TCP as interface structures, which allows us to study the distribution of dopants across them. As strontium is known to be biologically relevant, it is the ion of focus in the pilot study of this framework. The energy minimized (EM) surfaces and grain boundary structures were first created using a slab model. The behavior of Sr^{2+} ions was then investigated using a recently-developed Monte Carlo method. The preliminary results of this framework give access to interfacial energies and enthalpies of segregation for both surfaces and grain boundaries, quantities that have not been reported before. The results suggest that Sr-segregation can be expected for certain β-TCP grain boundaries but probably not all, and that the relative level of segregation will actually decrease as total dopant concentration in the ceramic is increased. Complementary microstructural characterizations were carried out using analytical electron microscopy to try and characterize a small number of grain boundaries of Sr-doped β-TCP ceramics. Those identified did not show any apparent segregation. Because of the limited sensitivity of the scanning transmission electron microscopy-energy dispersive X-ray spectroscopy (STEM-EDXS) technique applied here, correlated transmission electron microscopy and atom probe tomography measurements are proposed as the most suitable method for experimentally detecting grain boundary dopant segregation in the future.

Beyond the characterization of Sr-dopant distributions by STEM-EDXS, this thesis involved other electron microscopy analyses of various β-TCP samples. The β-TCP powders and ceramics studied throughout the thesis were prepared by Bastien Le Gars Santoni as part of the SNSF Sinterphos project (No. 200021_169027) that funded the current thesis. One of the main electron microscopy tasks was using scanning electron microscopy (SEM) to document and characterize the β-TCP powders and ceramics during the various stages of production — precipitated powders, calcined powders, sintered ceramics (before and after polishing), after various treatments for X-ray diffraction analysis, and after *in vitro* resorbability tests. This was done successfully and the results are highlighted in recent joint publications. Also, high spatial resolution electron microscopy analyses were carried out on Cu-doped β-TCP samples, where Cu is thought to have antibacterial and wound healing properties. In a 5.00% Cu-doped sample having the highest dopant content, we observed the formation of a secondary phase that is identified as a copper oxide. The presence of this Cu-rich secondary phase has a dramatic influence on the ceramic's biocompatibility, since it is correlated to a strong cytotoxicity

that killed osteoclasts during cell culture medium tests. This probably derives from the "burst release" of Cu^{2+} ions as the copper-rich oxide particles are dissolved. Nevertheless, beyond these secondary phases, this sample showed a uniform distribution of elemental Cu across grains and grain boundaries, similarly to the 5.00% Sr-doped sample.

This thesis has developed a methodology for investigating β-TCP at an atomistic level, from both a structural and microstructural point of view. Further developments and simulations are needed, but the methodology has been shown to be robust and reliable, such that it creates many avenues for future studies. From the electron microscopy front, the beam sensitivity introduced challenges to our investigations, but global powder and ceramic characterization was successful. Further work on how to better sample and characterize grain boundaries in these important biomaterials is needed.

Key words: β-tricalcium phosphate (β-TCP), atomistic simulation, scanning electron microscopy (SEM), scanning transmission electron microscopy (STEM), energy dispersive X-ray spectroscopy (EDXS), Monte Carlo, molecular dynamics, grain boundary, ion-doping.

Résumé

Les limites et les complications potentielles liées aux greffes osseuses autogènes ont suscité l'intérêt pour le développement de substituts de greffes osseuses synthétiques. Le β-phosphate tricalcique (β-TCP, $Ca_3(PO_4)_2$) est l'un des matériaux les plus prometteurs pour les substituts de greffes osseuses synthétiques car il est facilement résorbé et remplacé par de l'os nouveau. Cependant, même si le β-TCP est utilisé cliniquement depuis 1920, diverses études ont rapporté des réponses biologiques incohérentes pour cette biocéramique. Ceci est très probablement dû au fait que les mécanismes par lesquels le β-TCP est résorbé dans le corps humain sont encore loin d'être complètement compris. Afin de mieux comprendre le comportement *in vivo* du β-TCP, cette thèse se propose d'explorer les aspects des joints de grains et du dopage ionique dans le β-TCP via des simulations atomistiques et la microscopie électronique. Les connaissances ainsi acquises visent à mieux comprendre comment ils influencent à leur tour les processus de résorption et de guérison des substituts de greffons osseux β-TCP.

Pour des simulations atomistiques correctes, le réseau cristallin β-TCP présente un défi particulier, dans la mesure où un aspect incommensurable de sa structure est lié à un site spécifique, partiellement rempli de calcium, dans la cellule conventionnelle. Avant de considérer les simulations de structures dopées et d'interfaces, des simulations atomistiques détaillées de dynamique moléculaire et de Monte Carlo sont effectuées afin d'étudier les arrangements d'occupations de ce site par les ions calcium, allant de l'échelle de la maille conventionnelle jusqu'aux systèmes combinant quelques dizaines (centaines ou milliers) de mailles conventionnelle. Ces systèmes sont dénommés supermailles ci-après.

La structure cristalline β-TCP contient cinq sites Ca uniques dans la maille conventionnelle, avec une occupation partielle de 50% des six sites Ca(4). Elle présente donc vingt configurations possibles de la maille conventionnelle. En utilisant des simulations de dynamique moléculaire, les vingt configurations ont pu être classées en trois classes énergétiques : les configurations à faible (LEC), intermédiaire (IEC) et haute (HEC) énergie. Ces classes énergétiques sont en accord avec les simulations ou modélisations ou études théoriques précédentes. Cependant, différentes combinaisons des trois types de configurations dans des systèmes de supermailles ont présenté des énergies à peu près équivalentes à celles d'une supermaille composée uniquement de la maille conventionnelle

LEC. La conclusion est que le site Ca(4) de la structure β-TCP ne peut pas être décrit de manière adéquate dans une description à maille conventionnelle unique.

Ceci a été étudié plus en détail en considérant des mailles conventionnelles avec une occupation variable du Ca(4). L'occupation de 50% du site Ca(4) a été maintenue au niveau de la supermaille avec des combinaisons appropriées de mailles conventionnelles Ca(4) variables dans un arrangement en damier 3D. Cela a présenté des domaines d'occupation qui pourraient être liés énergétiquement à des changements dans les paramètres des réseaux a et c, un effet qui a également été observé expérimentalement. Des simulations de Monte Carlo (MC) ont ensuite été utilisées pour vérifier si les arrangements en damier choisis étaient faussés par l'échantillonnage de supermailles beaucoup plus grandes. Dans les simulations MC suivantes, aucun ordre à longue portée ni aucune configuration du Ca(4) partiellement occupé n'ont été observés. Au contraire, les sites Ca(4) semblent être occupés de manière aléatoire, mais à l'échelle de la supermaille, et non de la maille conventionnelle individuelle, ce qui explique dans une certaine mesure la nature incommensurable des résultats de diffraction des rayons X.

Suite à cette analyse, je traite la question du comportement des dopants dans les grains et les structures d'interface (surfaces, joints de grains). Un cadre est détaillé pour simuler les β-TCP comme des structures d'interface, ce qui nous permet d'étudier la distribution des dopants à ces structures d'interface. Comme le strontium est connu pour être biologiquement pertinent, il est l'ion ciblé dans l'étude pilote de ce cadre. Les surfaces à énergie minimisée (EM) et les structures des joints de grains ont d'abord été créées en utilisant un modèle de dalle. Le comportement des ions Sr a ensuite été étudié à l'aide d'une méthode de Monte Carlo récemment mise au point. Les résultats préliminaires de ce cadre donnent accès aux énergies interfaciales et aux enthalpies de ségrégation pour les surfaces et les joints de grains, des quantités qui n'ont pas été étudiées auparavant. Les résultats suggèrent que la ségrégation du Sr peut être attendue pour certains joints de grains β-TCP mais probablement pas pour tous, et que le niveau relatif de ségrégation diminuera en fait au fur et à mesure que la concentration totale de dopant dans la céramique augmente. Des caractérisations microstructurales complémentaires ont été effectuées en utilisant la microscopie électronique analytique pour essayer de caractériser un petit nombre de joints de grains de céramiques β-TCP dopées au Sr. Ceux qui ont été identifiés n'ont pas montré de ségrégation apparente. En raison de la sensibilité limitée de la technique de microscopie électronique à transmission à balayage et de spectroscopie de rayons X à dispersion d'énergie (STEM-EDXS) appliquée ici, des mesures corrélées de microscopie électronique à transmission et de tomographie par sonde atomique sont proposées comme la méthode la plus appropriée pour détecter expérimentalement la ségrégation des dopants aux joints de grains à l'avenir.

Au-delà de la caractérisation des distributions de Sr-dopant par STEM-EDXS, cette thèse a comporté d'autres analyses en microscopie électronique de divers échantillons de β-TCP. Les poudres et céramiques β-TCP étudiées tout au long de la thèse ont été préparées par Bastien Le Gars Santoni dans le cadre du projet Sinterphos du SNSF (No. 200021_169027) qui a financé la thèse présentée ici. L'une des principales tâches de la

microscopie électronique a été l'utilisation de la microscopie électronique à balayage (MEB) pour documenter et caractériser les poudres et céramiques β-TCP au cours des différentes étapes de production — poudres précipitées, poudres calcinées, céramiques frittées (avant et après polissage), après divers traitements pour l'analyse par diffraction des rayons X, et après les tests de résorbabilité *in vitro* . Ces travaux ont été réalisés avec succès et les résultats sont présentés dans des publications conjointes récentes. De plus, des analyses de microscopie électronique à haute résolution spatiale ont été effectuées sur des échantillons de β-TCP dopés au Cu, où le Cu est censé avoir des propriétés antibactériennes et de cicatrisation. Dans un échantillon dopé au Cu à 5,00% ayant la teneur en dopant la plus élevée, nous avons observé la formation d'une phase secondaire qui est identifiée comme un oxyde de cuivre. La présence de cette phase secondaire riche en Cu a une influence considérable sur la biocompatibilité de la céramique, puisqu'elle est corrélée à une forte cytotoxicité qui a tué les ostéoclastes lors des tests sur milieu de culture cellulaire. Cela provient probablement de la "libération en rafale" d'ions Cu^{2+} lors de la dissolution des particules d'oxyde riches en cuivre. Néanmoins, au-delà de ces phases secondaires, cet échantillon a montré une distribution uniforme du Cu conventionnelle à travers les grains et les joints de grains, de manière similaire à l'échantillon dopé au Sr à 5,00%.

Cette thèse a permis de développer une méthodologie pour étudier le β-TCP à un niveau atomistique, tant d'un point de vue structurel que microstructurel. Des développements et des simulations supplémentaires sont nécessaires, mais la méthodologie s'est avérée robuste et fiable, de sorte qu'elle ouvre de nombreuses voies pour des études futures. En ce qui concerne la microscopie électronique, la sensibilité du faisceau a posé des problèmes à nos recherches, mais la caractérisation globale des poudres et des céramiques a été réussie. Des travaux supplémentaires sur la façon de mieux échantillonner et caractériser les joints de grains dans ces biomatériaux importants sont nécessaires.

Mots clefs : β-phosphate tricalcique (β-TCP), simulation atomistique, microscopie électronique à balayage (MEB), microscopie électronique à transmission à balayage (STEM), spectroscopie de rayons X à dispersion d'énergie (EDXS), Monte Carlo, dynamique moléculaire, joint de grain, dopage ionique.

Contents

List of Figures

List of Tables

1 Introduction

The repair of bone defects larger than a 'critical' size, that are caused by trauma, tumor, or disease (i.e. osteoporosis), requires the use of bone grafts to help enhance regeneration. Among all clinically-available grafts, autologous bone (bone taken from the patient) is still considered the "gold standard" since it combines all necessary properties required in bone regeneration [1]. However, only a limited amount of bone can be taken from the patient, and the bone grafting procedure is far from risk free. Indeed, the surgical procedure is associated with a complication rate ranging from 9.4% to 40% [2].

Over the past decades, synthetic bone substitutes have been developed to address these limitations. Calcium phosphates (CaPs) are the main constituents of bone and teeth, making them the material of choice to repair damaged bone. Most of the efforts to use calcium phosphate bone grafts have been focused on hydroxyapatite (HA, $Ca_5(PO_4)_3OH$), β-tricalcium phosphate (β-TCP, $Ca_3(PO_4)_2$), or their composites called biphasic calcium phosphate (BCP). From numerous studies investigating the *in vivo* behavior of calcium phosphates, β-TCP is readily resorbed and replaced by new bone [3], while HA has proved to be fairly inert *in vivo* [4]. Further, while β-TCP and BCP are resorbed by cell-mediated acid-driven dissolution, BCP resorption is a function of its HA content: the higher the HA content, the slower the resorption [5]. For these reasons, β-TCP is proposed to be the most promising of the calcium phosphate candidates, and is therefore the phase of focus in this thesis.

A prerequisite for the effectiveness of synthetic bone substitutes is bio-resorption. Calcium phosphate resorption can occur either by spontaneous chemical dissolution or by cell-mediated chemical dissolution. It was thought that the cut-off between these two processes was defined by the solubility constant of the CaP phase. However, this schematic explanation has been questioned in recent years, by various experimental observations suggesting that mixed resorption processes can occur [6]. Nonetheless, the resorption mechanisms are still far from being completely understood, and it is therefore

crucial to develop a better understanding of the mechanisms by which calcium phosphate is resorbed into the human body.

<div align="center">(a)   (b)</div>
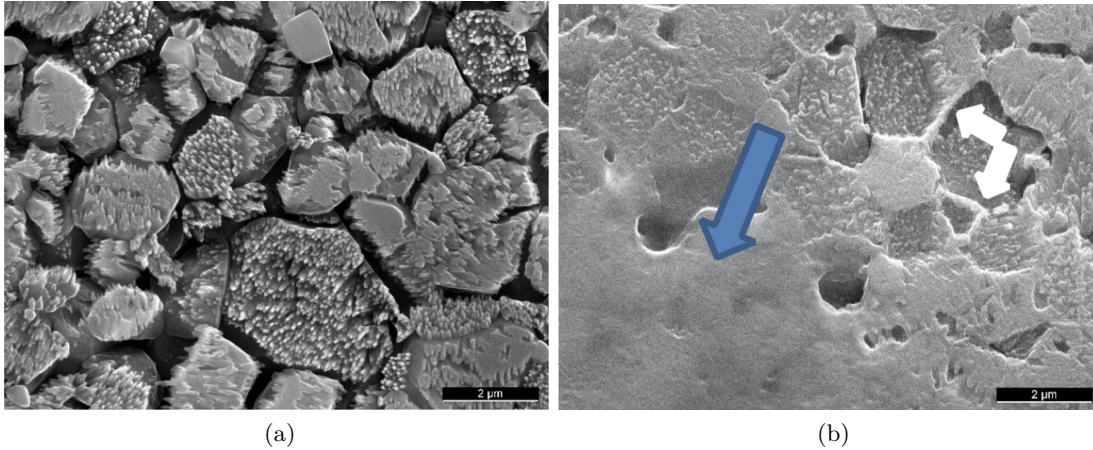
Figure 1.1 – Resorbed β-TCP surface with (a) grain boundary dissolution and (b) remnants of grain walls.

From a scientific point of view, a thorough understanding of the link between grain boundary composition and the *in vitro* behavior of ion-doped calcium phosphates will help render the design of CaP bone graft substitutes with enhanced bone-forming capabilities. For instance, various experimental results suggest that spontaneous grain boundary dissolution of β-TCP occurs when it is saturated in cell culture media [7, 8]. Dense β-TCP samples incubated in the presence of osteoclasts show a similar behavior. The osteoclasts are able to attack the ceramic surface, leaving behind a resorption track. Figure 1.1 shows two examples of the resorbed surfaces left by osteoclasts that, interestingly, display the existence of morphological differences in the attacked β-TCP surfaces. Figure 1.1a displays grain boundary dissolution along the resorption track, exposing pillar-like structures with the formation of gaps between the "grains". On the other hand, some areas of Figure 1.1b displayed preferential grain dissolution resulting in the formation of walls between grains, suggesting that an alternative behavior in which the grain boundaries are thermodynamically more stable than the grains. Unfortunately, it is unclear why these different behaviors occur and, as a result, how they can be modified or controlled. Thus, understanding the link between dissolution and grain boundaries is essential in order to design calcium phosphate bone graft substitutes with enhanced bone-forming capabilities.

Grain boundaries are essential in the resorption of sintered calcium phosphate ceramics. In a low pH *in vitro* study, Koerten and van Meullen [9] observed dissolution of the necks between the grains and preferential degradation marks present at the surface of individual grains. The degradation pattern of the *in vitro* experiment was similar to their *in vivo* experiment. Koerten and van Meullen mention that the first step of the dissolution process preferentially attacks the grain boundaries, consequently leading to the

deterioration of grains and the formation of cracks and irregularities. An *in vitro* study conducted by Seo et al. [10] investigated the dissolution of hydroxyapatite powders. Grain boundaries of hydroxyapatite were predominantly dissolved, with dissolution then extending into the bulk. This dissolving behavior generates hydroxyapatite particles, disintegrates dense microstructure, and forms µm-scale cavities. In other words, grain boundaries play an important role in the cell mediated dissolution of calcium phosphate ceramics.

Rather than being "pure", calcium phosphate ceramics are often ion-doped in order to exploit therapeutic properties and to trigger favorable biological reactions during ceramic resorption. For example, silicon doping has been suggested to have positive effects on osteogenesis [11, 12]. However, a release of Si ions in therapeutic doses is hard to imagine as it is essentially inert [13]. A proposed explanation for the resorption of therapeutic ions is that the dopants are partly located at the grain boundaries, and fast grain boundary dissolution then leads to the release of dopants and/or loose particles [14–16]. The few studies looking at ion-doped calcium phosphate dissolution often detect a larger ratio between dopant and Ca ions in the dissolution than in the bulk. To draw conclusions about the mechanism of action of the ions, their precise location must be known and, despite preliminary work [17], there are currently no such studies. Experimental and theoretical results suggest that β-TCP doping should not lead to grain boundary segregation because doping is not only easy, but energetically favorable according to first principle calculations. This conclusion is supported by the fact that β-TCP doping with monovalent and divalent cations tends to increase rather than decrease the thermal and mechanical stability of β-TCP [18].

From the above, the scientific literature provides clear evidence of the respective importance of grain boundaries and ion-doping for the *in vivo* behavior of β-TCP ceramics. However, many aspects and connections between the two have either not been investigated or remain obscure. This makes it difficult to interpret *in vivo* studies performed with β-TCP ceramics, in particular the still inexplicable 'osteoinductivity' of ion-substituted calcium phosphate ceramics, or the relative importance of cell-mediated resorption of calcium phosphate ceramics.

In order to address the above knowledge gaps and deficiencies, this thesis set out to explore the following hypotheses, within a Swiss National Science Foundation project (Project n° 200021_169027): (1) the grain boundary stability of β-TCP ceramics can be modified by the use of dopants, and (2) the change in grain boundary stability strongly influences the resorption and healing processes of β-TCP bone graft substitutes. The project involved two PhD studies. The first was dedicated to producing, characterizing and testing β-TCP ceramics with controlled purity and ion doping [19]. The second — as presented in this thesis — worked with these controllably-produced ceramics to investigate these hypotheses, with recourse to a combination of atomistic simulations and electron microscopy characterization. Specifically, it concerns the following objectives:

- Obtaining an improved understanding of the β-TCP crystal structure with atomistic simulations, as powder X-ray diffraction and synchrotron analyses have not been able to fully resolve the structure.

- Characterizing the grain structures and grain boundaries of the synthesized ceramics, and observing the effects of the dissolution and cell-culture tests (in collaboration with other project partners).

- Developing a computational framework that can be used to investigate dopant behavior at grain boundaries and eventually relate these to experimental observations from the electron microscopy work.

To investigate these aims, the thesis is structured as follows:

- **Chapter 1** – Introduces the aims and structure of the thesis.

- **Chapter 2** – Briefly describes the computational methods used in the thesis.

- **Chapter 3** – Briefly introduces the electron microscopy techniques used in the thesis.

- **Chapter 4** – Investigates the crystal structure of pure β-TCP by atomistic simulations in order to clarify the reasons behind the inconclusive powder diffraction and synchrotron structure analyses.

- **Chapter 5** – Develops and applies the framework for simulating interfaces in pure and ion doped β-TCP, namely surfaces and grain boundaries. Presents first simulation and experimental results on the segregation of strontium, as a model ion-doping system.

- **Chapter 6** – Describes the main studies of the electron microscopy work, by summarizing the successful documentation of multiple samples in collaborative work with project partners, and presents an in-depth analysis of one of the ion doped samples.

- **Chapter 7** – This chapter concludes the thesis with a summary of critical findings. Future avenues to be explored will also be discussed.

2 Computational Methods

This chapter briefly describes the computational methods used in this thesis. It begins by describing the types of structures typically investigated in Chapters 4 and 5. The force fields used throughout the thesis are briefly described after, followed by the workhorse computational methods.

2.1 Simulation cell types

Unit cells and supercells. The simplest description of crystalline material is with the unit cell. However, the size of the unit cell is generally insufficient for satisfying computational simulations. The typical rule of thumb is for the dimensions of the simulation box to be greater than twice the cutoff-radius of the force field. This is generally achieved by replicating the unit cell in the three dimensions to create a suitably-sized supercell system. Chapter 4 is dedicated to illustrating that, in the case of the β-TCP crystal structure, this is not a straightforward task.

Slabs. Slab structures are considered the basic building blocks for creating surface and grain boundary structures. Slabs are constructed by cleaving the unit cell along a desired crystallographic plane. The cut-away atoms are "re-packaged" such that the volume and the number of atoms in the unit cell remain constant. A unit cell can be cut at different depths, resulting in a plethora of terminations. However, for practical reasons, only the lowest energy termination is considered for creating surfaces and grain boundary structures. In this thesis, the METADISE code [20] is typically used for creating the interface structures via the defined slab method.

Surface structures. The surface structures are created by stacking slabs to an appropriate thickness such that there is a bulk-like region that separates the surface regions from interacting with each other. Simulations involving surface structures apply 3D-periodic boundary conditions. This means that the introduced vacuum gap must be big enough to exclude interactions from the opposing surface through the vacuum gap.

The typical surface structure sizes stack m slabs to an approximate structure depth of ~ 75 Å, with a vacuum gap of 35 Å.

Grain boundary structures. The vacuum-surface slab set up can be adapted to other interface types by filling the vacuum gap with the material of interest. In the case of creating grain boundaries, this is done by mirroring an image of the surface structure across the surface plane, with an introduced 2 Å gap between the bodies. The interface between the two structures is scanned by energy minimizing at each rigid body displacement step taken. This results in a potential energy map (Figure 2.1), and the minimum of the map determines the displacement vector for the ideal arrangement of the two surfaces. The appropriately arranged surfaces are relaxed until convergence, resulting in a near coincidence grain boundary.
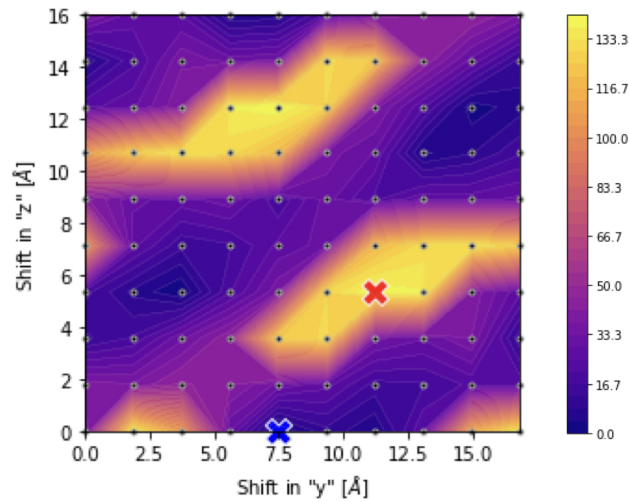
Figure 2.1 – Energy map of the scanned interface. The ideal displacement vector is defined by the potential energy minimum indicated by the blue cross. The highest energy arrangement is identified with the red cross.

2.2 Force fields

As the various simulations cell types have now been explained, the forces acting on the atoms of the simulation must be defined. This is done by employing a force field. The force field describes the various components in a system and their interactions with respect to one another. Many functional forms exist for describing intermolecular forms. Two frequent forms used throughout this thesis are the Buckingham potential (Equation 2.1) and the Lennard Jones potential in the A/B form (Equation 2.2):

$$E_{\text{Buck}}(r) = A_{\text{Buck}} e^{-r/\rho_{\text{Buck}}} - \frac{C_{\text{Buck}}}{r^6} \tag{2.1}$$

$$E_{\mathrm{LJ}}(r) = 4\epsilon \left[\left(\frac{A_{\mathrm{LJ}}}{r} \right)^{12} - \left(\frac{B_{\mathrm{LJ}}}{r} \right)^6 \right] \tag{2.2}$$

The potential energy, E_{Buck} of Equation 2.1 and E_{LJ} of Equation 2.2, is evaluated as a function of r, the distance between the two interacting particles. The constants $\{A_{\mathrm{Buck}}, \rho_{\mathrm{Buck}}, C_{\mathrm{Buck}}\}$ of Equation 2.1 and $\{\epsilon, A_{\mathrm{LJ}}, B_{\mathrm{LJ}}\}$ of Equation 2.2 are refined parameters that define the shape of the functional form. In both cases, the functional forms describing interatomic interactions contain a repulsive and attractive term. The repulsive term repels two interacting particles, due to the overlap of electron orbitals at very short distances. The attractive term describes the attraction between two interacting particles at moderate distances, which quickly vanishes at long distances.

Intramolecular interactions are used in cases when a molecular entity must be maintained. For example, a phosphate tetrahedron is described by two quantities: the relative positioning of P–O bond lengths, $r_0 = 1.5946$ Å, and the O–P–O angle, θ_0 = 109.5°. These features are preserved by associating an increase in energy with any deviations from these equilibrium values. The bond stretching potential can be defined by a simple harmonic of Equation 2.3, and the angle bending can be defined by a three-body functional form of Equation 2.4:

$$U_{ij} = \frac{1}{2} k_2 (r_{ij} - r_0)^2 \tag{2.3}$$

$$U_{ijk} = \frac{1}{2} k_3^{\mathrm{angle}} (\theta_{ijk} - \theta_0)^2 + k_3^{\mathrm{bond\text{-}bond}} (r_{ij} - r_{0ij})(r_{jk} - r_{0jk}) + $$
$$k_3^{\mathrm{bond\text{-}angle}} [(r_{ij} - r_{0ij}) + (r_{jk} - r_{0jk})](\theta_{ijk} - \theta_0) \tag{2.4}$$

The two-body potential of Equation 2.3 considers a harmonic spring potential of constant k_{ij} that imparts an energetic penalty if the relative distance, r_{ij}, between particles i and j deviates from the equilibrium bond distance, r_0. The three-body potential of Equation 2.4 imposes an equilibrium bond angle, θ_0, and equilibrium bond distances, r_{0ij} and r_{0jk}. Deviations from these values are penalized by the constants k_3^{angle}, $k_3^{\mathrm{bond\text{-}bond}}$, and $k_3^{\mathrm{bond\text{-}angle}}$.

2.3   Simulation techniques

The two methods in molecular simulations typically used in this thesis are Molecular Dynamics (MD) and Monte Carlo (MC). All MD simulations in this thesis were performed with the LAMMPS computational suite [21]. As the forces acting on the system have now been defined, the classical Newton's law of motion is used to calculate accelerations and velocities and to update the atom positions. The integration of movement is done numerically. Therefore, the time step must be chosen with care to avoid instability. The bottleneck of MD simulations is generally the length of simulation time needed. Given the potential complexity of a free energy landscape, this typically means most simulations explore only a small region around the energy minimum closest to the initial configuration. One method for overcoming the consequent sampling issues that occur in the presence of rough energy landscapes is by Monte Carlo simulations.

All MC simulations in this thesis were performed using DL_MONTE [22, 23]. MC simulations can attempt a number of different moves, such as (1) atomic and molecular displacements, (2) molecular rotations, or even the (3) pairwise exchange of atomic coordinates. An MC move is accepted or rejected according to the Metropolis algorithm [24] based on the change in energy, ΔE, of the system. If the move brings the system to a state of lower energy ($\Delta E < 0$), the move is accepted and the particle is moved to the new position. If $\Delta E > 0$, the move is allowed with a probability given by $\exp(-\Delta E/k_{\mathrm{b}}T)$, where T is the defined temperature of the system.

MC simulations are typically more powerful than MD in addressing the sampling issues which arise from rough energy landscapes. Nevertheless, while low temperature systems precisely sample across a region of the energy landscape, even with MC they may become trapped in a local energy minimum during the timescale of a typical computer simulation. In this case, the replica exchange method (REM) [25, 26] accelerates sampling of energy landscapes by allowing the systems at different temperatures to exchange complete configurations. This is typically implemented by initializing M replicas, each at different temperatures T_i: from $T_1 < T_2 < \ldots < T_M$. Temperatures are chosen to ensure the best possible sampling with the minimum amount of computational cost. T_1 is typically the temperature of interest. T_M is the highest temperature and must be chosen sufficiently high to ensure that no replicas become trapped in local energy minima, and M the number of replicas used must be large enough to ensure swapping between all adjacent replicas.

Application details of the different methods are given in more detail in the relevant sections of the thesis and appendices.

3 Electron microscopy characterization techniques

The thesis work involved two main electron microscopy activities. The first was documenting the β-TCP powders and ceramics synthesized by Dr. Bastien Le Gars Santoni during his thesis [19]. In this catalogue, the samples were documented at various stages (e.g. powders in certain states, sintered ceramics), following different synthesis conditions (e.g. variable pH, variable dopant content). Polished sections of sintered ceramics were also imaged after exposure to various media such as cell cultures and osteoclasts. The second was higher resolution analysis of dopant distributions across sintered ceramic grain boundaries.

This chapter introduces the electron microscopy methods used for executing the microscopy activities. The instruments used for observing the samples will be described, followed by the typical methods used for preparing the studied materials, and the electron microscopy data acquisition parameters. All electron microscopy investigations were performed at the Interdisciplinary Centre for Electron Microscopy (CIME) at EPFL.

3.1   Scanning electron microscopy (SEM)

The documenting work on powders, ceramics, and cell culture tests utilized a Zeiss Merlin Field Emission scanning electron microscope. The microscope is equipped with numerous detectors, the main ones used being the Everhart Thornley (ET) Secondary Electron (SE) detector, the In-Lens SE detector, and the insertable Oxford Instruments energy dispersive X-ray spectroscopy (EDXS) detector.

3.1.1   Powder preparation and imaging

A major imaging effort through the thesis was the documentation of powders. This requires the proper preparation techniques for high resolution SEM imaging. Viewing the β-TCP powders in SEM is a challenging task. These samples are non-conductive and hence charge while imaging with the electron beam. It is therefore not possible to obtain high-resolution images that capture the detailed morphological features of the powders without applying a conductive coating to them. To solve this problem, the application of two different conductive coatings was compared: (1) 10 nm of sputtered carbon, and (2) 5 nm of osmium (OsO$_4$), see Figure 3.1.

Carbon films are commonly used in electron microscopy for their low background signal and their relatively good electron conductivity. However, inspection of Figure 3.1a shows that the structural features of the sample were smothered by the 10 nm carbon coating. Additionally, the charging effect was not fully alleviated, even with a low probe current of 50 pA. This is seen by the bright contrast at the top right corner of Figure 3.1a. In contrast, Figure 3.1b shows that the osmium coating conforms much better to the powder surface topography. It therefore presents the structural features of the powder more faithfully, and further showed no problems of charging, even when the probe current was increased to 80 pA. In consequence, all SEM studies of doped and un-doped β-TCP powders were made with the samples coated with 5 nm of osmium. We note that this was done by a technician personnel at CIME, who had received the training necessary for handling this toxic substance. The SEM images were typically recorded using the In-Lens detector, with an accelerating voltage of 1.00 kV and a probe current of 80 pA, and a working distance between 2.0–3.0 mm. These conditions were chosen to maximize spatial definition of the surface topography.

3.1.2   Slipcast and sintered ceramics

The polished slipcast and sintered ceramics were typically imaged in SEM by appending the sample to an aluminum stub using a conductive carbon tape. The β-TCP ceramics are more conductive than the powders, and typically do not need to be coated to view in SEM at the standard imaging setting with an accelerating voltage of 1.00 kV and a probe current of 80 pA, with a working distance between 5.0–6.0 mm to increase signal
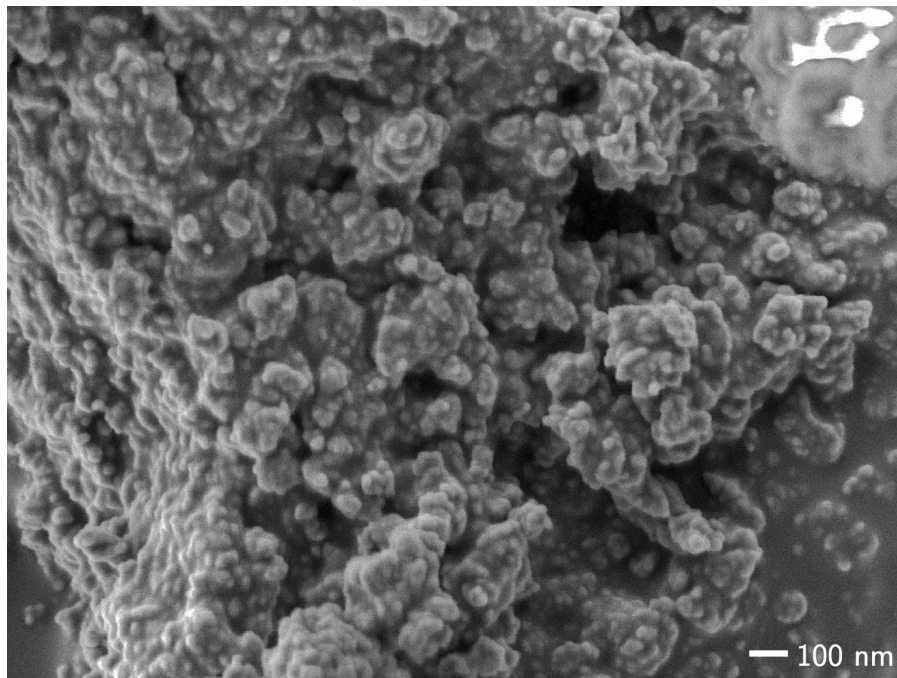
(a)
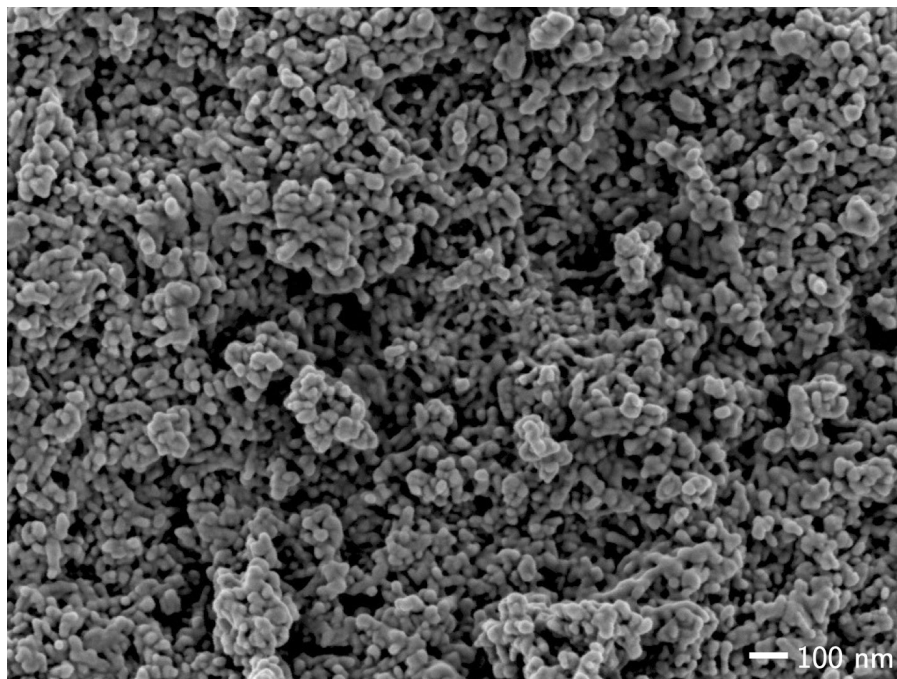
(b)

Figure 3.1 – Two conductive coatings on pure β-TCP powders after synthesis and drying: (a) 10 nm of carbon coating and (b) 5 nm of osmium coating. Both overviews are imaged in SEM with the following parameters: 1.00 kV high tension, 50 pA probe current, at working distances between 2.3–3.0 mm, using the In-Lens SE Detector.

detection by the ET detector. Note that, here, the ET detector was preferred over the In-Lens SE detector in order to achieve a stronger topographical contrast, for instance when imaging resorbed surfaces. However, some samples were trickier to image, with some charging experienced. In this case, the edge and top lip of the ceramic were painted with silver paint. This was usually enough to alleviate charging in order to observe the surfaces. Figure 3.2 provides typical SEM images of such slipcast and sintered ceramics, showing polished and thermally-etched surfaces as now described.

The resorption experiments using exposure to different media, such as cell cultures or osteoclasts, required the preparation and imaging of polished sections of slipcast and sintered dense ceramic pillars. This sample preparation was performed by Dr. Le Gars Santoni during his PhD thesis, according to the following procedure. First, the ceramics are fractured down the middle in order to expose the interior of the volume. The fractured face is then polished with 30 µm diamond lapping film until the fracture surface is basically flattened. The polishing process is next continued with 15 µm, 6 µm, 3 µm, 1 µm, 0.5 µm lapping paper in order to increase the surface smoothness. The lapping paper is exchanged to a higher grade after a depth of three times the grain size of the previous lapping paper grade is removed. The polishing is finished with a final polish using 0.1 µm silica colloid suspension. This gives a final high grade polished surface, as for instance shown in Figure 3.2a of a 0.10% Sr-doped sintered sample.

While some individual grains can be observed in Figure 3.2a, thanks to some electron channeling contrast, differentiating all the grain boundaries on the polished surface is challenging. It was attempted to increase the channeling contrast by using an in-lens electron backscattered detector on the Zeiss Merlin, but this was not successful. However, two different analyses required reliable grain boundary visualization on the polished sections. The first was for the statistical analyses of grain sizes by Dr. Le Gars Santoni using the line intercept method. The second was for serving one of the major initial aims of the electron microscopy characterization in this thesis, namely the study of dopant distributions across grain boundaries. In order to pursue these aims, the grain boundaries of the sintered and polished sections were exposed by thermally treating the polished samples at 1000°C for 1 h. This treatment leads to a thermal etching at the grain boundaries, after which they are visible in SE SEM images, as for example shown in Figure 3.2b.
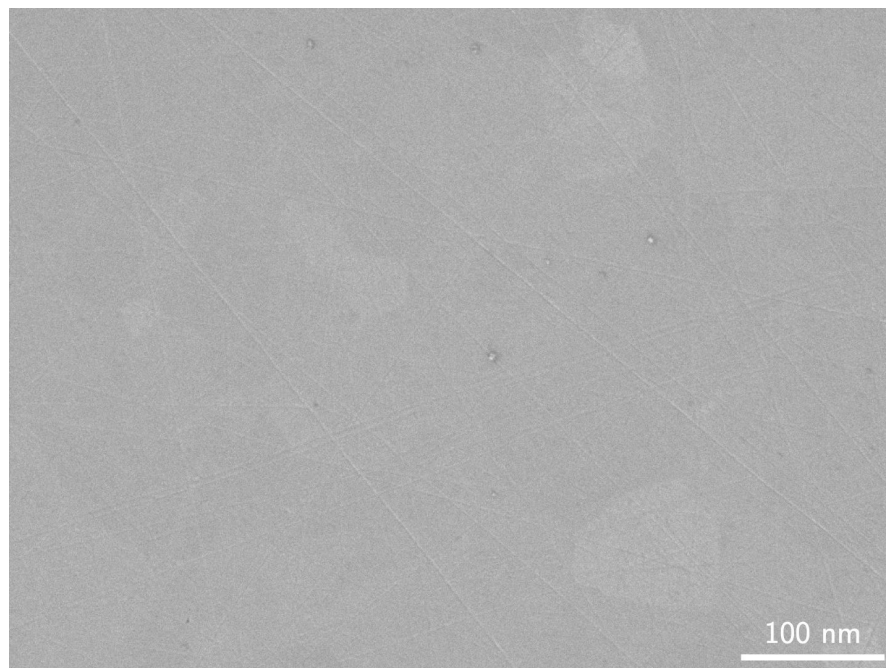
(a)
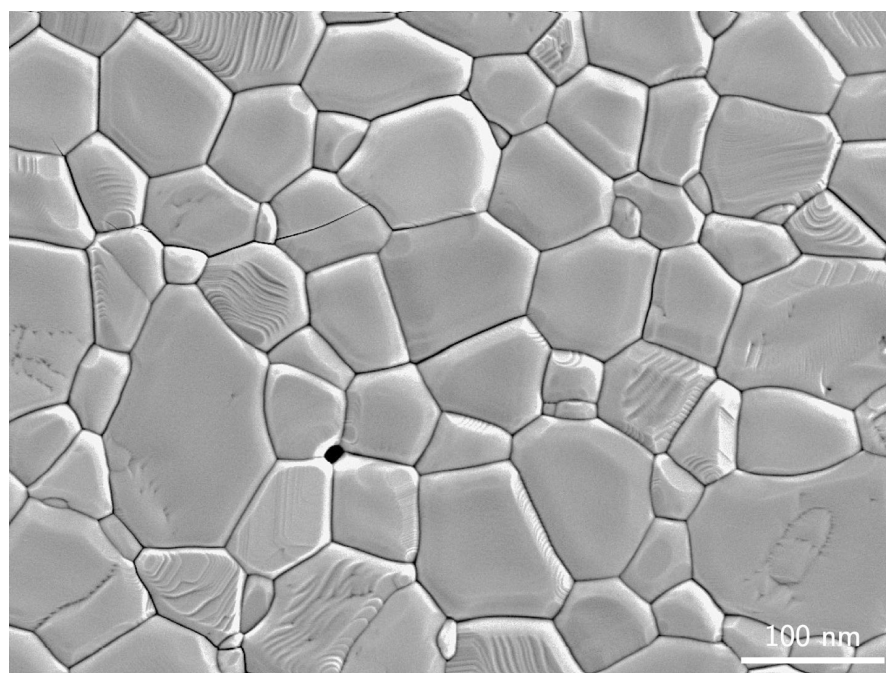
(b)

Figure 3.2 – SEM images of the (a) polished ceramic surface, imaged with the following parameters: 1.00 kV high tension, 85 pA probe current, at working distance between 5.0–5.5 mm, using the ET Detector. The (b) thermally etched surface reveals the grain boundaries of the ceramics, imaged at: 3.00 kV high tension, 1 nA probe current, at working distance between 5.0–5.5 mm, using the ET Detector.

3.1.3 SEM-EDXS

SEM-EDXS was used as a first approach to characterizing dopant distributions in the doped β-TCP powders and ceramics. These analyses were made in SEM mapping mode using an insertable EDXS detector, and acquiring the data using the Aztec software from Oxford Instruments. The EDXS detector used was a windowless Oxford Instruments X-Max Extreme silicon drift detector (SDD) that is optimized for acquiring low energy X-rays. The reason behind this choice was to maximize the spatial resolution of the EDXS maps by reducing the interaction volume from which the X-rays are emitted, through the application of a relatively low beam energy of 8 keV and then selecting the lower energy L-peaks for mapping the Sr and Cu dopants studied.

3.2 Transmission electron microscopy (TEM)

In this thesis, TEM was mainly used to perform high spatial resolution chemical analyses by EDXS mapping in scanning transmission electron microscopy (STEM) mode in order to study dopant distributions. Both powder and sintered ceramic samples were studied. While SEM-EDXS is a useful tool of characterizing elemental composition, even with the acquisition conditions described above, the spatial resolution of the analytical X-ray signal was likely insufficient for a faithful characterization of dopant distributions. In comparison, the spatial resolution of the STEM-EDXS signal measures on the order of 1–2 nm. All TEM/STEM investigations were performed using either an FEI Tecnai Osiris microscope or an FEI Talos F200S microscope.

3.2.1 Powder preparation and imaging

Imaging the powders was non-trivial. Due to the material sensitivity, the only powders that could be observed in TEM without rapid beam-induced degradation or transformation were ones that had been thermally treated at 1000°C, 15 h, followed by 840°C, 15 h (as used for XRD studies). These powders were fine enough to be freely dispersed onto a holey-carbon TEM grid for observation. Figure 3.3 shows an example STEM image of such a powder sample. Ultimately, no dopant segregation was observed in any of these powder samples by STEM-EDXS: Sr-doped (1.00%, 2.92%, 5.00%) and Plasma Biotal powders. Rather, dopant distributions always appeared homogeneous. However, compared to simulated dopant distributions, the powder samples were not produced by a representative heat treatment. Further, their complicated morphology limits precise interpretability of the dopant distributions. Therefore, for compactness, STEM-EDXS results from the powder samples are not presented in this thesis.

Figure 3.3 – HAADF-STEM image of a 2.92% Sr-doped β-TCP powder, thermally treated for XRD.

3.2.2   Slipcast and sintered ceramics

In order to solve the above limitations of STEM-EDXS analysis of powder samples, we instead need to study samples prepared from slipcast and sintered β-TCP ceramics. In order to prepare electron transparent lamellae from such sintered ceramics, a Focused Ion Beam (FIB) methodology was applied. The lamellae were prepared from sintered β-TCP ceramics that had been polished and thermally etched, such that possible grain boundaries (or secondary-phases in the case of heavily Cu-doped ceramics) could be selected by imaging with the SEM column and then sectioned with the FIB milling. After protecting the sample surfaces using electron beam and then ion beam deposited amorphous carbon, a standard FIB lift-out of the region of interest was performed using a nano-manipulator. Afterwards, the lifted-out pieces were attached to suitable half-moon support grids, and then thinned to electron transparency using a 30 kV Ga ion beam. This was typically followed by a final polishing with a 5 kV Ga ion beam. Prior to the lift-out, the polished and thermally etched β-TCP cylinders were coated with 5 nm OsO_4 to prevent (excessive) charging during the FIB milling processes. The target sample thicknesses for the lamellae were $\sim$100 nm in order to increase analytical X-ray signal over a very thin sample, while remaining electron transparent. Producing an artifact-free, uniformly thick sample could be challenging, as seen in Chapter 5 Section 4. All lamellae were prepared by Dr. Barbora Bártová of CIME, EPFL.

3.2.3   TEM, STEM, and EDXS data acquisition and data processing

TEM images were acquired using either a Gatan Orius camera with Gatan Digital Micrograph software (FEI Osiris) or an FEI CETA camera with Thermoscientific Velox software (FEI Talos).

The STEM images were predominantly acquired using a Fischione photomultiplier tube "high angle annular dark-field" (HAADF) detectors, either with FEI TEM Image and Analysis (TIA)/Bruker Esprit softwares (FEI Osiris) or Thermoscientific Velox software (FEI Talos). We note that, for imaging grain structures, the camera length for the HAADF STEM detector was sometimes reduced in order to increase diffraction contrast/decrease atomic number Z-contrast compared to typical HAADF imaging conditions.

The analytical EDX signals were captured using FEI "ChemiSTEM" SDD detectors, of which there are four on the FEI Osiris and two on the FEI Talos microscopes used in the thesis. Osiris STEM-EDXS data were recorded using Bruker Esprit software, and Talos STEM-EDXS data with Thermoscientific Velox software. The same softwares were used offline for the processing of their respectively acquired data.

3.2.4   Acquisition complications for STEM-EDXS data

One of the primary aims of the electron microscopy characterization is to measure the distribution of dopants at the grain boundaries by STEM-EDXS mapping. However, numerous difficulties were encountered during these investigations. Short pixel dwell times and multi-frame mapping was required in order to reduce or limit the sample damage caused by the focused STEM electron probe. For instance, resting the probe in one location for a few seconds will create a hole in the TEM sample. However, during this multi-frame mapping, because of the insulating nature of the β-TCP ceramics, problematic charging was often observed when studying the FIB lamellae. Essentially, after acquiring, say, 10 frames, the image of the lamella would suddenly jump spontaneously. Since the mapping would continue, without being able to remove any frame(s) from the data-set occurring after the jump, a thusly acquired data-set was rendered useless. In order to mitigate this issue, we acquired most of the STEM-EDXS data on the Talos F200S. While this has half the number of SDD detectors as the Osiris, and so with about half the X-ray collection efficiency, unlike Bruker Esprit its Velox acquisition software saves multi-frame EDXS mapping data in a frame-by-frame format. Therefore, when the mapping area 'jumps', the acquisition can be stopped, and the displaced frames can be removed from the acquired data-set.

The second difficulty encountered involves the degradation/transformation of the sample under the electron beam in the mapping area. Figure 3.4 shows an example of this. This is clearly seen in the pits formed at the bottom of the mapping acquisition area, where sample material has been lost. In addition, another unwanted effect is a transformation of the sample under the electron beam. Judging by the contrast of the HAADF–STEM image, this has led to a redistribution of elements in the mapped area (e.g. the white spots seen in the acquisition area are proposed to indicate the induced local segregation of copper in the matrix and at the grain boundary).

(a)   (b)
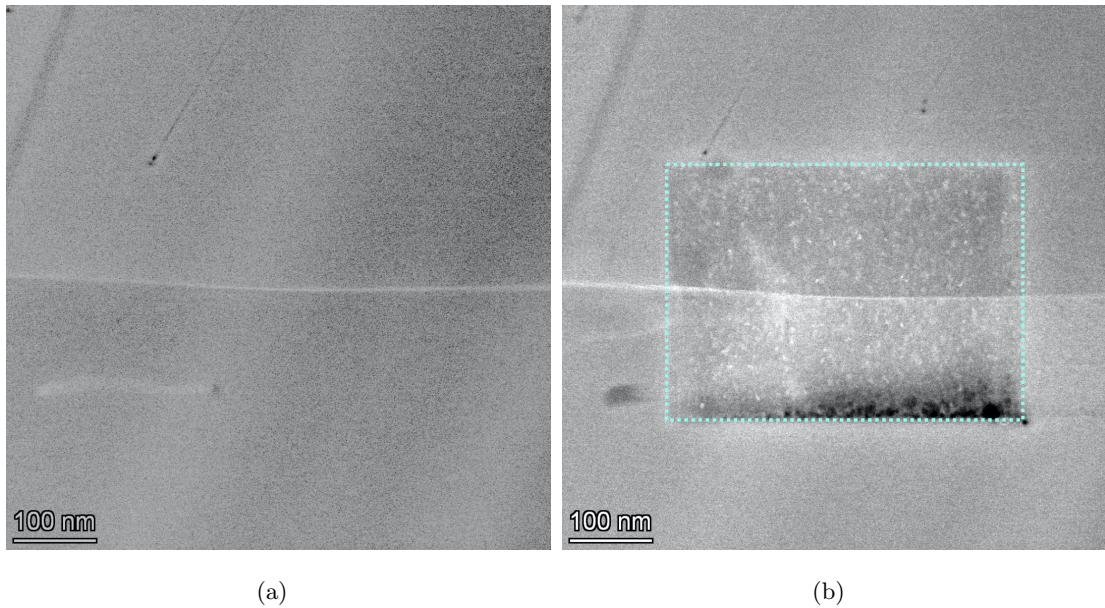
Figure 3.4 – HAADF-STEM overview of an acquisition area (a) before and (b) after
mapping acquisition. The mapped area, indicated by the dashed line, shows the
degradation of the 5.00% Cu-doped TEM lamella under the electron beam.

Different strategies were tried to ameliorate this problem. The first attempted
solution was to lower the high tension of the beam to 80 kV. This, however, actually
accelerated the problems of both charging and sample damage. A better option found
was to reduce the flux of the incident electron beam by both reducing the spatial sampling
frequency of the mapping, and reducing the pixel dwell time (i.e. faster scanning). For
instance, by increasing the pixel size from 0.32 to 1.30 nm and decreasing the dwell time
from 10.0 to 5.0 µs, it was possible to increase the total mapping time of the 5.00%
Cu-doped lamella to ∼20 minutes without significant visible sample degradation, all while
keeping the same electron probe current of ∼0.8 nA. Figure 3.5 shows how application
of these settings significantly reduces damage in the mapped area of a "Plasma Biotal"
sample that proved to be particularly beam sensitive, even though the edges of the
acquisition area still show pitting from the beam.

Aside from this type of pitting, the fact that the sample degradation increases as
the high tension is reduced suggests that the damage mechanism is primarily radiolysis
(i.e. ionization), rather than knock-on damage [27]. In this case, it may be possible to
stabilize the sample further by cooling it in-situ using a liquid nitrogen cooled specimen
stage. This would be an interesting strategy to test in the future.

(a)   (b)
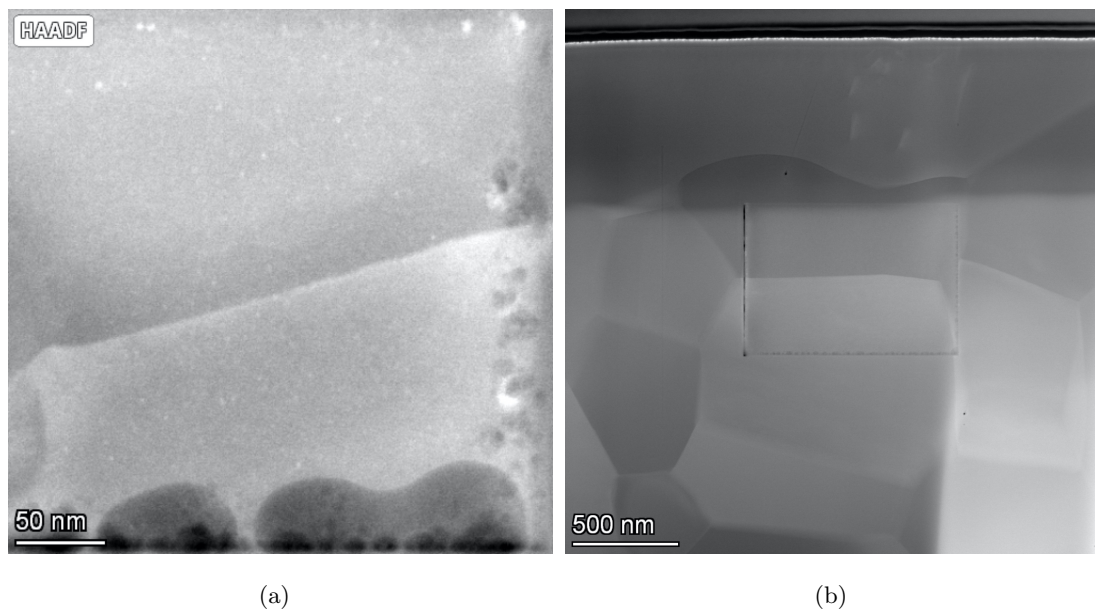
Figure 3.5 – (a) HAADF-STEM image of the "Plasma Biotal" sample after 4 min acquisition time (647.5 pm pixel size, 5.00 µs pixel dwell time) shows significant sample degradation at the edges of the map. (b) Overview of the acquisition area shows damage to the "Plasma Biotal" sample is significantly reduced with a 1.295 nm pixel size and 5.00 µs pixel dwell time. Acquisition time was increased to 20 min.

4 Study of the β-TCP crystal structure with atomistic simulations

The β-TCP unit cell is traditionally reported as rhombohedral, with the space group $R3c$ and lattice dimensions: $a = b = 10.4352$ Å, $c = 37.4029$ Å. The unit cell contains 273 atoms that are distributed among five Ca sites, three P sites, and 10 O sites. These sites are arranged in two repeating columns down the c-axis, referenced as the A-column and B-column, as shown in Figure 4.1. The A-column hosts the —P(1)O$_4$ ⋯ Ca(4) ⋯ Ca(5)— sites, and the B-column tightly packs the —P(2)O$_4$ ⋯ Ca(1) ⋯ Ca(3) ⋯ Ca(2) ⋯ P(3)O$_4$— sites [28]. Every A-column is surrounded by six B-columns, and every B-column is surrounded by four A-columns and two B-columns.

Despite the above understanding of the β-TCP lattice, obtaining an accurate description of the structure presents a surprising challenge, which is connected with the partial occupation of the Ca(4) site. Dickens et al. [29] first reported difficulties in refining the Ca(4) site, which they resolved by half occupying each of those sites in their fit of single-crystal X-ray data. Yashima et al. also reported difficulties in characterizing the β-TCP structure by refinement of neutron power diffraction data [28]. The occupancies of the five Ca sites were allowed to vary freely in the preliminary refinement, while the isotropic thermal parameters were fixed to be equivalent for all sites. However, there were difficulties in convergence when applying anisotropic thermal parameters. Therefore, the final refinement applied a restriction of the thermal parameters such that the occupancies of Ca(1), Ca(2), Ca(3), and Ca(5) were set equal to 1 and the isotropic thermal parameters were allowed to vary along with the occupancy of the Ca(4) site. This resulted in an estimated Ca(4) site partial occupancy of 0.434 [28]. Nevertheless, in both cases, the performed refinements still present inconsistencies in the fits between the experimental X-ray diffraction data and the refined β-TCP structure.

Given the failure of experimental studies to solve the mystery surrounding the Ca(4) site of the β-TCP crystal structure, this chapter aims to do so by applying suitable atomistic simulations. On this basis, the approach taken to gain further insights into the Ca(4) site is as follows:
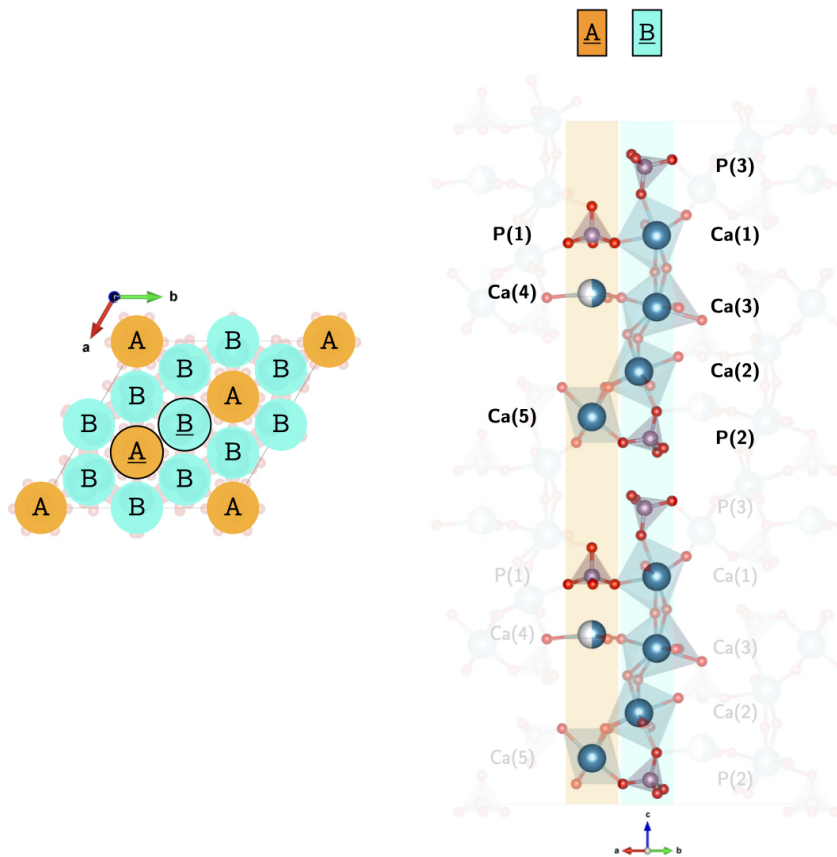
Figure 4.1 – The β-TCP crystal structure displayed down the c-axis, shows the unit cell is composed of two repeating columns: the A-column, and B-column.

- **Section 1** – Explores the β-TCP structure on the level of a single unit cell, and validates the potential set that will be used for future atomistic modeling studies, using molecular dynamics (MD) and Monte Carlo (MC) simulations.

- **Section 2** – Describes a first approach of tackling the Ca(4) site occupancy over longer ranges than the single unit cell, through various supercell compositions, where 50% occupancy of the Ca(4) site is maintained on the level of the unit cell.

- **Section 3** – Explores a second approach that is an extension of Section 4.2. Stimulated by recent experimental findings, checkerboard combinations of unit cells that have variable Ca(4) site occupancy are considered. The 50% occupancy of the Ca(4) site is globally preserved in the supercell by considering appropriate combinations of unit cells that each have variable Ca(4) site occupancy.

- **Section 4** – Employs Monte Carlo simulations to explore the Ca(4) site occupancy while removing pre-existing constraints, e.g. from pre-defined unit cell domains, and investigates the structural outputs by applying the tools that have been developed in the previous sections.

4.1   The β-TCP unit cell

4.1.1   Introduction

The experimentally-derived occupancies suggest that the Ca(4) site is partially occupied by about 50%. In the context of atomistic simulations, this Ca(4) site must be defined to maintain charge neutrality of the simulation box. The experimentally-reported structure has six calcium sites available for three calcium atoms to occupy. This results in ($_6C_3 =$) 20 possible ways of distributing these three Ca atoms among the six sites within the unit cell. In this section we explore these twenty possible unit cell configurations, on the level of the single unit cell.

4.1.2   Methods

The basic β-TCP crystal structure determined by Yashima et al [28] was used to construct the twenty possible unit cells. The simulations in this study were carried out with the LAMMPS computational suite used for molecular dynamics (MD) simulations [21]. An input requirement of such simulations is a potential field that describes the forces between the various atoms in the crystal structure. Here, we apply the potentials that were derived by Demichellis et al. for calcium phosphate systems, which includes the β-TCP structure [30]. These Demichellis potentials describe the short-range interactions between all pairs with the Buckingham potential. The long-range interactions that act between all pairs of atoms, except those within the same phosphate tetrahedron, are described by Coulombic forces with a cut-off distance of 13 Å and the Ewald summation for the long-range interactions. Systems were first relaxed by energy minimization using the conjugate gradient method [31], followed by the application of the Nosé-Hoover thermostat [32] to bring the simulation box to 300 K. Using the isothermal-isobaric ensemble, simulations were performed with a combination of the Nosé-Hoover thermostat with a Martyna-Tuckerman-Tobias-Klein (MTTK) barostat [33] to maintain a temperature of 300 K and pressure of 1 bar. Simulation boxes were equilibrated for 2 ns, followed by a production period of 2 ns using a 1 fs timestep. Three-dimensional periodic boundary conditions were applied to the simulation box. Details of how to construct the simulation boxes and LAMMPS input files can be found in Appendix A.

4.1.3   Results and Discussion

The twenty possible configurations created by filling three of the six Ca(4) sites were explored by MD simulations. We first explore how the energetics of the configurations are affected by the Ca(4) site arrangements. The relative energies of the twenty MD equilibrated configurations are plotted in Figure 4.2, relative to the configuration that was found to be most stable. It is clear that the configurations can be grouped into three
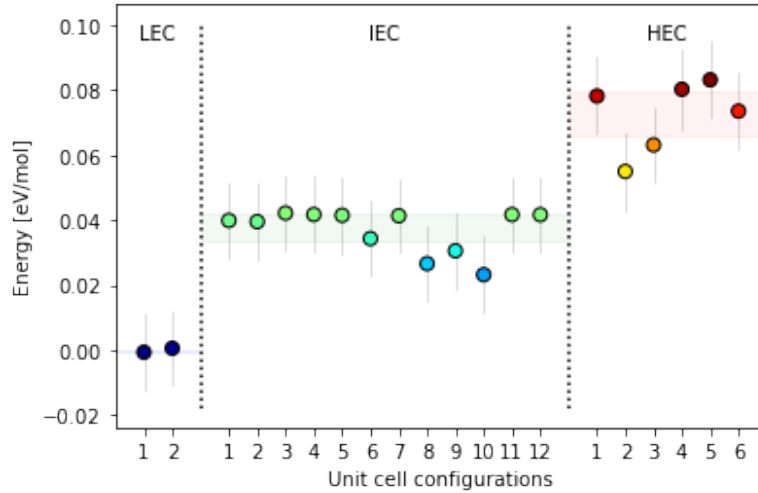
Figure 4.2 – Energies of the twenty primitive unit cell configurations reported relative to the most stable configuration. The split in energetics clearly shows there are two LEC, twelve IEC, and six HEC structures.

energetic classes, which for future reference will be called the low (LEC), intermediate (IEC), and high (HEC) energy configurations; there are two LECs, twelve IECs, and six HECs.

The distinction of the energetic levels is dependent on the placement of the Ca(4) atoms within the structure [34]. Figure 4.3 shows example configurations from each of the energetically distinct groups. The example LEC corresponds to the Ca(4) atoms being separated by the furthest distance of 13.8470 Å (Figure 4.3a), with the other LEC showing the same behavior, just with the occupied and vacant Ca(4) sites being swapped around. The LEC has also been identified from other investigations of the twenty β-TCP unit cell variations by Jay et al. [34] using a classical lattice technique, and Matsunaga et al. [35] using first principles calculations. Other computational studies note the LEC arrangement to be the most favorable, but did not probe all twenty β-TCP unit cell variations. In these studies, Liang et al. [36] identified the LEC using ab initio density functional theory from six investigated models, while a density functional theory by Yin et al. [37] only investigated two Ca(4) site arrangements.

For the twelve IECs, the Ca(4) atoms are arranged closer together, as seen in the example in Figure 4.3c, resulting in a higher average lattice energy of 0.0406 eV/mol relative to the LECs. There are six HECs where the occupied Ca(4) sites are arranged closest together by 8.6694 Å (see example in Figure 4.3b), resulting in the largest lattice energy of 0.0758 eV/mol relative to the LECs. This is complementary to the prediction of Jay et al., that the differences between the three types of occupancies is likely due to the relative differences between the occupied Ca(4) sites.
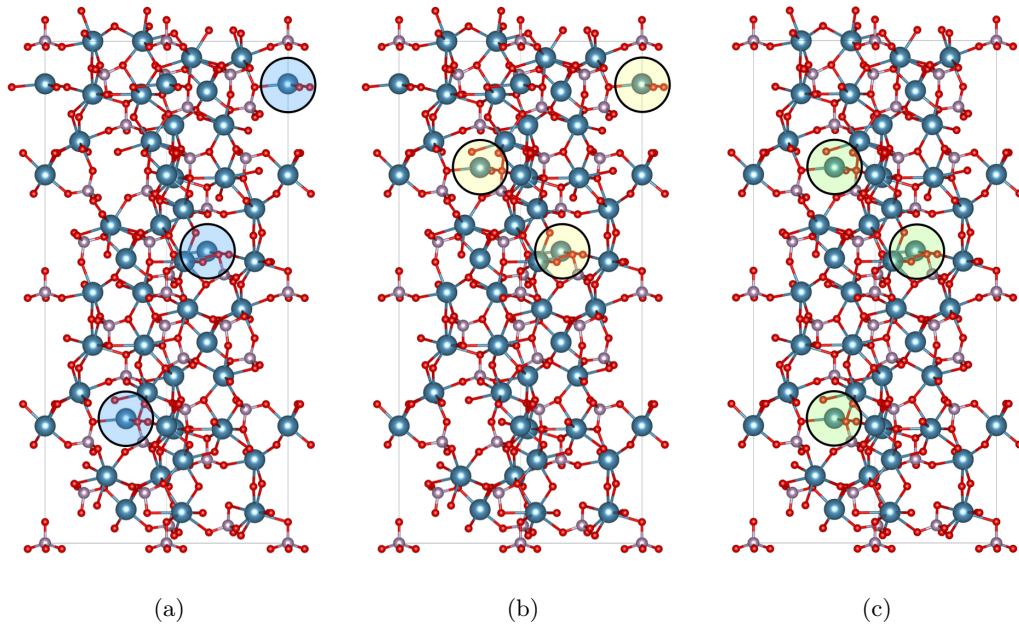
Figure 4.3 – Ca(4) atoms of example (a) LEC, (b) HEC, and (c) IEC unit cells, viewed normal to the (1 1 0). The (a) LEC has the Ca atoms placed furthest apart. The (b) HEC has Ca atoms occupying sites closest together.

A detailed structural study will next be presented for evaluating the potentials. The potentials were verified by comparing the MD equilibrated lattice constants and bond lengths to experimentally-reported values. The representative lattice parameters of the energetic classes are presented in Table 4.1, as the mean from the simulated lattice parameters of the configurations belonging to their respective energetic class. The simulated lattice parameters, although generally elongated compared to the experimental values, are otherwise in good agreement with the experimental values, for instance showing relative differences below 2% with respect to the lattice parameters reported by Yashima et al [28]. Although these simulations use the Demichellis derived potentials, the reported values from these simulations are slightly larger than the lattice parameters reported by Demichellis et al. for their MD simulations, see Table 4.1. This difference can most likely be explained by their MD sampling that is run in an aqueous environment, while these simulations are bulk calculations of the crystal structure.

Interestingly, the lattice parameters vary between the energetic classes. The LEC features the greatest elongation of the *a*-lattice parameter and the smallest elongation of the *c*-lattice parameter. The lattice parameter trend of the HEC trend is opposite to the LEC, with the smallest elongation of the a-lattice parameter and the largest elongation of the *c*-lattice parameter. The IEC structures feature elongations of the *a*- and *c*-lattice parameters that lie between the those of the LEC and the HEC. These elongations of the lattice parameters suggest that the structural features of the β-TCP crystal lattice

Table 4.1 – MD equilibrated lattice parameters for each energetic class.

	Exp. [28]	Demichellis	This Work (MD Equilibrated)		
			LEC ($n = 2$)	IEC ($n = 12$)	HEC ($n = 6$)
a [Å]	10.4352	10.4757	10.5171	10.5015	10.4889
b [Å]			10.5183	10.5034	10.4889
c [Å]	37.4029	37.6414	37.9352	38.0415	38.1472
α [°]	90	-	90.0	90.0	90.0
β [°]		-			
γ [°]	120	-	120.0	120.0	120.0

are influenced by the arrangement of the Ca(4) site. Specifically, that the unit cell is compensating for internal stresses as a result of the Ca(4) site arrangements, resulting in different expansions of the unit cell.

To better understand the elongations seen in the lattice parameters, we look to investigating the local environment of the CaO$_{CN}$ polyhedra, where CN is the coordination of the Ca site, and PO$_4$ tetrahedra. Additional details for determining Ca–O and P–O bond lengths are included in Appendix B.1. We first consider the CaO$_{CN}$ environment, reported in Table 4.2. The calcium atoms of the β-TCP crystal structure are located at five crystallographic sites. The coordination polyhedra were determined by considering Ca–O bond lengths less than 2.8 Å. From the data in Table 4.2, the LEC , IEC , and HEC structures were determined to have the following coordination numbers: CN(Ca(1)) = 7, CN(Ca(2)) = 8, CN(Ca(4)) = 6, CN(Ca(5)) = 6. The IEC and HEC structures report CN(Ca(3)) = 8, while the LEC structure reports CN(Ca(3)) = 7. The determined coordination numbers are generally in good agreement with the experimentally reported values. However, the determined coordination around the Ca(4) site is significantly different than the experimentally reported coordination number of CN(Ca(4)) = 3. In this study, the Ca(4) site is six-fold coordinated. As expected, there are three Ca(4)–O(1,1',1''), but there are also three Ca(4)–O(2,2',2'') bond lengths of 2.4395 - 2.5268 Å.

From the relative differences of the Ca–O bond lengths of the LEC, IEC, and HEC reported in Table 4.2, it can be seen that the bond lengths are generally in good agreement with the experimentally-reported values. The largest relative errors are seen in the following bond lengths: the HEC structure features an elongation of the Ca(1)–O(3) by +5.7%, and the LEC structures feature contractions of the Ca(3)–O(10) and Ca(3)–O(2) bond lengths by -5.2% and -6.5%, respectively, and an elongation of the Ca(4)–O(1) by +5.1%. These respective distortions of the CaO$_{CN}$ polyhedra could explain the different lattice parameters.

Table 4.2 – Determined bond lengths of the Ca environments, reported as relative differences [%] to experimental values.

		Exp. [28]	This Work (MD Equilibrated)		
			LEC ($n = 2$)	IEC ($n = 12$)	HEC ($n = 6$)
Ca(1)	O(6)	2.3277	-0.3	-0.2	-0.1
	O(5)	2.3907	-1.3	-1.2	-1.4
	O(8)	2.4196	1.1	1.3	1.2
	O(4, 4')	2.4518	0.4	-0.5	-0.4
		2.4718	-0.4	-1.3	-1.2
	O(9)	2.4648	1.1	-0.4	-1.3
	O(3)	2.5127	3.8	-0.5	5.7
Ca(2)	O(9)	2.3578	2.5	2.2	1.5
	O(3)	2.3757	-0.2	-0.2	-0.4
	O(1)	2.4067	-2.9	-1.7	0.1
	O(7,7')	2.4228	0.9	1.1	1.2
		2.4247	0.9	1.0	1.1
	O(2)	2.4197	-2.4	-2.9	-2.9
	O(5)	2.7027	1.4	0.4	-0.8
	O(6)	2.7448	-0.6	-0.9	-1.3
Ca(3)	O(3)	2.3547	1.9	2.8	3.4
	O(5)	2.3936	2.2	1.6	0.8
	O(6)	2.5477	-1.6	-2.3	-3.5
	O(8,8')	2.5687	0.4	1.0	2.0
		2.6227	-1.7	-1.1	-0.1
	O(10)	2.5734	-5.2	-4.0	-2.1
	O(2)	2.5997	-6.5	-4.6	-3.8
	O(1)	2.6896	–	2.8	2.3
Ca(4)	O(1, 1', 1'')	2.5316	5.1	-2.4	-3.4
	O(2, 2', 2'')*	–	2.5268	2.4792	2.4395
Ca(5)	O(4, 4', 4'')	2.2119	2.0	2.2	2.5
	O(7, 7', 7'')	2.3129	-2.6	-2.5	-2.3

Note: Ca(4)–O(2, 2', 2'') are reported as absolute values.

Table 4.3 – Determined bond lengths of the phosphate tetrahedra, reported as relative differences [%] to the experimental values.

		Exp. [28]	This Work (MD Equilibrated)		
			LEC ($n = 2$)	IEC ($n = 12$)	HEC ($n = 6$)
P(1)	O(9, 9', 9'')	1.5280	2.44	2.05	2.24
	O(10)	1.5740	-0.46	-0.86	-0.97
P(2)	O(1)	1.5540	-0.02	-0.05	0.11
	O(2)	1.5120	2.91	2.94	3.21
	O(3)	1.5670	-0.02	-0.34	-0.27
	O(4)	1.5180	2.82	2.37	2.52
P(3)	O(5)	1.5360	1.66	1.48	1.53
	O(6)	1.5450	0.63	0.58	0.61
	O(7)	1.5500	0.13	0.31	0.31
	O(8)	1.5100	2.95	3.25	2.90

Now looking at the phosphate tetrahedra, the determined bond lengths from the MD trajectory generally reproduce the experimental P–O bond lengths, as seen in Table 4.3. It is worth noting the simulated phosphate tetrahedra have more symmetric P–O bond lengths, centered around 1.5580 Å. This is most likely due to the two-body intramolecular definition that imparts a large energetic penalty if the bond length deviates from the defined equilibrium bond length of 1.5946 Å. Despite these deviations, the cell parameters and internal structure are preserved with the Demichellis potentials, which compared well to density functional theory (DFT) and polarizable potentials in their paper [30].

4.1.4 Conclusion

In this section, the twenty possible variations of Ca(4) site occupancy of the β-TCP unit cell were explored by MD simulations, using the force field derived by Demichellis et al. The twenty configurations could be grouped into three energetic classes: the LEC ($n = 2$), IEC ($n = 12$), and HEC ($n = 6$). The lattice parameters of the three energetic classes were investigated and found to be within good agreement with the experimentally-reported values. The bond lengths of the Ca–O polyhedra and phosphate tetrahedra were also compared to experimental values. The Ca–O environments were generally well preserved. However, the Ca(4) site was found to be additionally coordinated to O(2) in the three energetic classes, with bond lengths between 2.4395–2.5268 Å.

While these simulations, in line with other computational studies, identify the LEC to be the most favorable on the level of the single unit cell, this does not explain the

mystery of the Ca(4) site. The Ca(4) site as arranged in the LEC would be identified by diffraction studies, since the defined periodicity would be described by an alternative unit cell with different symmetry. That the β-TCP structure instead remains incommensurate with diffraction analyses suggests that the Ca(4) site occupancy is neither fully random, nor fully ordered, on the scale of the single unit cell. It therefore needs to be investigated over larger length scales, as will be addressed in the following sections. However, the good consistency between simulated and experimental structural values indicates that this β-TCP force field can be used for these further studies.

4.2   Case study: 'Patching' supercell systems

4.2.1   Introduction

The previous section explored the structure of β-TCP on the level of the unit cell. It was realized that the partial occupancy of the Ca(4) site introduces twenty variations of the β-TCP unit cell, and identified the low energy configuration (LEC) as the most stable variation of these unit cells by separating the Ca(4) atoms by 13.8 Å. However, in reality the Ca(4) site cannot be arranged in the LEC, as the highly ordered site would be identified by diffraction studies. Therefore, the Ca(4) site occupancy must be investigated over longer ranges. It is the aim of this section to illustrate the complexities introduced with simulating the β-TCP crystal structure as a supercell system.

4.2.2   Methods

Consider a β-TCP supercell system composed of nine unit cells, with approximately equal lattice parameters: $3a = 3b = 31.3056$ Å, $c = 37.6414$ Å, $\alpha = \beta = 90°$, $\gamma = 120°$. With the twenty unit cells presented in Section 4.1, a supercell system containing nine unit cells consists of 5.12×10^{11} possible ways of arranging the constituent unit cells. In this section, a first attempt is made to explore this parameter space by "patching" the supercells systems together by hand. Various combinations of low (LEC), intermediate (IEC), and high (HEC) energy configuration unit cells from Section 4.1 were combined into twenty seven different supercell system using VESTA. The various systems composed are shown in Figure 4.4. The MD sampling protocol implemented in Section 1 was used to equilibrate these supercell structures.
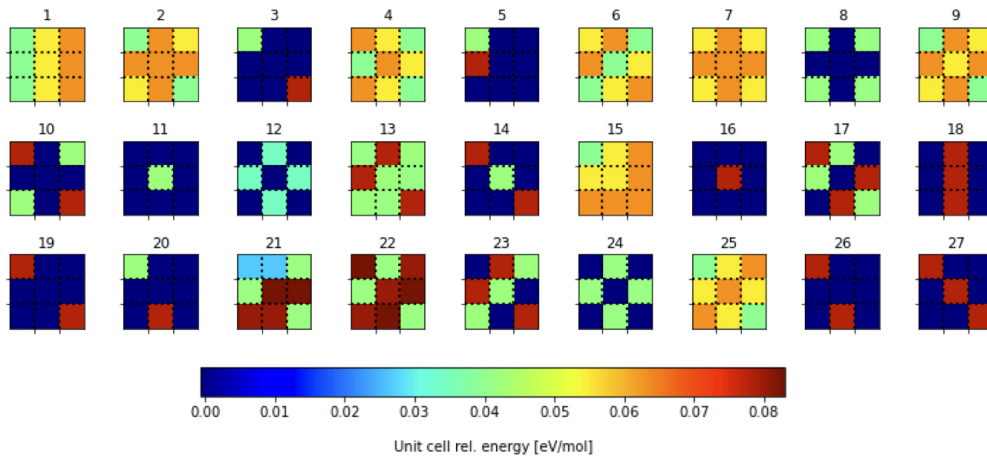
Figure 4.4 – Schematic representation of the "patched" systems represented as a grid, where each cell in the grid is a unit cell. Various supercell systems combine the twenty primitive unit cells into a supercell, where the cell is colored according to the energy of the primitive unit cell.

4.2.3   Results & Discussion

After creating these twenty seven supercell variants, they were equilibrated by MD. In Figure 4.5, the MD equilibrated energies of the supercell structures are plotted relative to the energy of the equilibrated supercell system composed solely of LEC . Interestingly, supercell systems that combine unit cells from the three energetic classes can have similar energies to the supercell system solely composed of LECs. For example, Supercells 1 and 4 are examples of possible ways of combining IEC and HEC unit-cell types in such a way that there is a stabilizing effect, where the equilibrated energies are found to be similar to that of the supercell composed solely of the LEC.
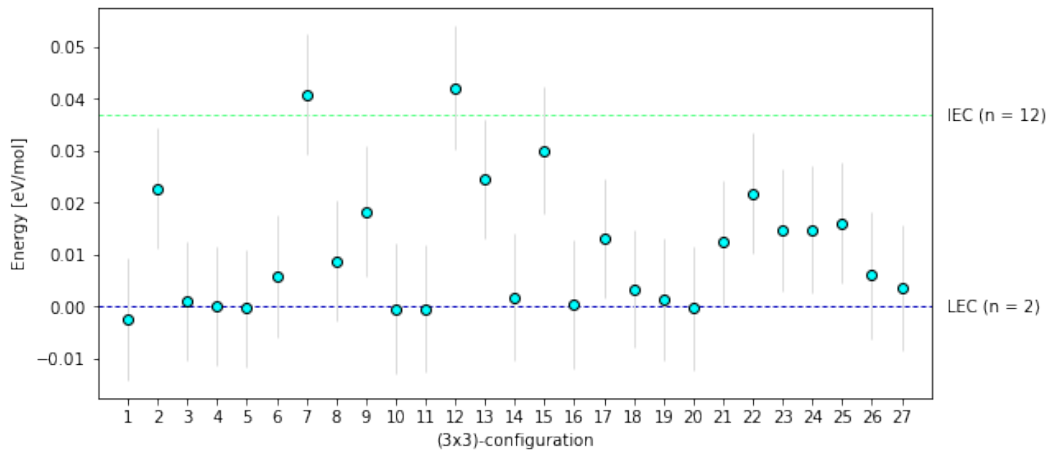
Figure 4.5 – Energies of the patched supercell systems (labelled in Figure 4.4) plotted relative to the energy of a system composed solely of LEC.

We believe that the identification of numerous configurations that are energetically equivalent to the LEC is a first step towards explaining the incommensurate nature of the experimental X-ray diffraction (XRD) pattern. It could be envisaged that numerous small domains of different supercell configurations, each with distinct cation ordering, could be created during the synthesis process, without the thermodynamic driving force to adopt a single, fully ordered crystal structure. As the characterization method samples over long ranges of the material, the observed XRD pattern becomes a superposition of patterns from these many domains, each with their own short to medium range ordering. The composite XRD signal from the different locally-ordered domains may then average to a pattern indicative of neither a completely random ordering of Ca(4) site occupation (with $\sim 50\%$ occupancy per unit cell), nor fully ordered Ca(4) site occupation.

4.2.4   Conclusion

The complexity of correctly simulating the β-TCP crystal structure is illustrated with a simplified case study that considers a supercell system containing 9 unit cells. Twenty
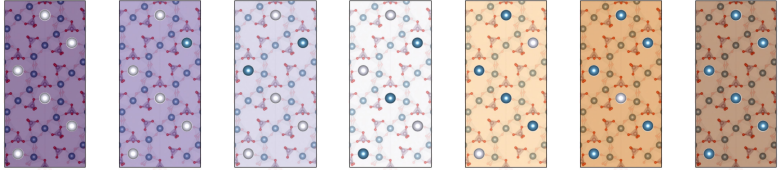
seven supercell systems that "patched" together combinations of the twenty β-TCP unit cell variations were MD equilibrated. Even within the limited sample size investigated, numerous configurations that combined LEC, IEC, and HEC unit cells were identified to be as energetically stable as the supercell system composed solely of LECs. This implies that a single unit cell definition is an inaccurate description of the Ca(4) site in the β-TCP crystal structure. Understanding if and how these domains are ordered will be of crucial importance. It contributes to the compositional flexibility of the β-TCP system that can ultimately determine the behavior of dopants. The following sections will address these questions by probing optimal arrangements of the Ca(4) site at longer ranges.

4.3   Towards an improved understanding of the β-TCP crystal structure by means of "checkerboard" atomistic simulations

4.3.1   Introduction

A recent experimental study raised yet another question concerning the β-TCP structure. In this study, high purity β-TCP powders were synthesized with varying Ca:P molar ratios. Rietveld refinement analyses of powder X-ray diffraction (XRD) patterns identified a general tendency of the a-lattice parameter decreasing linearly and the c-lattice parameter increasing linearly with increasing Ca:P ratio. Surprisingly, however, the curves showed a discontinuity of the lattice parameters at the ideal ratio of Ca:P = 1.50 [38]. An estimated 0.0021 Å difference in the a-lattice parameter, and a 0.0133 Å difference in the c-lattice parameter was extrapolated between these two domains. This step-like behavior of the lattice parameters at Ca:P = 1.50 suggested the existence of two distinct β-TCP variations. Le Gars Santoni et al. [38] proposed that, rather than each unit cell containing exactly 50% filled Ca(4) sites, these domains could be composed of unit cells that range in degree of Ca(4) site occupancy. As summarized in Table 4.4, the unit cells could range from zero to full Ca(4) site occupancy. Describing the site filling by the factor $n = 0, 1, 2, 3, 4, 5, 6$ Ca atoms filling up to the six possible Ca(4) sites, this gives seven unit cell types with respective Ca:P molar ratios of 1.429, 1.452, 1.476, 1.50, 1.524, 1.548, 1.571. Except for the unit cell types with fully occupied and fully empty Ca(4) sites, the unit cell types with $n = 1, 2, 3, 4, 5$ can have different arrangements of calcium ions on the Ca(4) sites, as described by the respective $_6C_n$ values in Table 4.4. If appropriately combined, a lattice made of these seven unit cell types could maintain an average Ca:P molar ratio of 1.50, while offering the possibility of local "domains" that may help resolve the previously discussed structural questions. The present study investigates this hypothesis with appropriately conceived atomistic simulations.

Table 4.4 – Unit cells with varying occupied Ca(4) sites.

Filled Ca(4) sites (n)	0	1	2	3	4	5	6
Ca:P	1.429	1.452	1.476	1.500	1.524	1.548	1.571
$_6C_n$	1	6	15	20	15	6	1

4.3.2   Methods

As a starting point for the simulations, we set up "checkerboard" domain arrangements made up of four pairs of unit cell types having n values that, all together, give an average Ca:P molar ratio of 1.50, i.e. (0&6)-, (1&5)-, (2&4)-, and (3&3)-domains as shown in Figure 4.6. The initial domain configurations are set up to cover 662 combinations of $_6C_n$ values, in order to fully test the combinatorial space, which were then allowed to equilibrate via a molecular dynamics protocol in order to investigate various properties that could be influenced by the arrangement of calcium ions in the Ca(4) sites. Given the extensive combinatorial outcomes of the simulations, the resultant datasets need to be suitably segmented for interpretability. To do this, we apply a clustering algorithm to determine highly correlated configurations. Further study of these highly correlated configurations leads to potentially new concepts for understanding the arrangement of Ca(4) site occupancies in the β-TCP lattice.
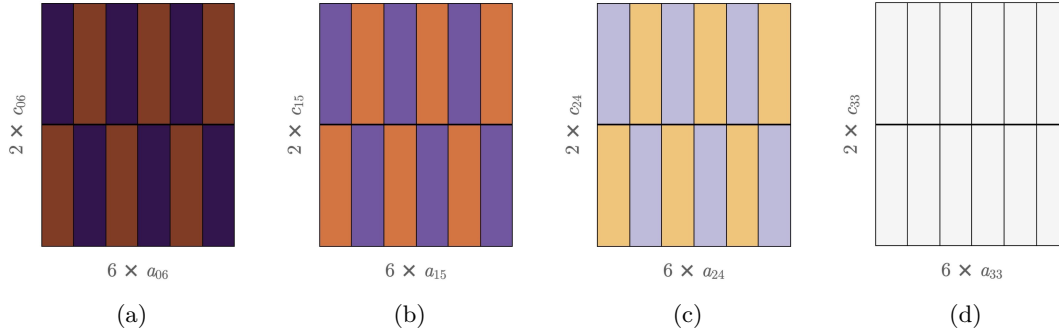
Figure 4.6 – Patterning of the various unit cells to create the (a) (0&6)-domain, (b) (1&5)-domain, (c) (2&4)-domain, and (d) (3&3)-domain.

       The basic β-TCP crystal structure determined by Yashima et al [28] was used to construct a series of supercell structures with varying Ca(4) arrangements using the seven β-TCP unit cells of Table 4.4. We considered the possible combinations ($_6C_n$) for filling $n = \{0, 1, 2, 3, 4, 5, 6\}$ of the six possible Ca(4) sites, summarized in Table 4.4. To limit the number of configurations to be studied, the unit cells were paired according to their occupancy counterparts, (0&6), (1&5), (2&4), and (3&3), to maintain a charge neutral system with a net 50% occupancy of the Ca(4) site. Supercell configurations were constructed by patterning the paired configurations in a 3D-checkerboard arrangement composed of eight unit cells, following the schematic of Figure 4.6. To limit the number of each domain mixture that will be considered, the domain mixture is composed of repeating base pairs. This results in 662 configurations that were considered; (0&6)-domain: $(_6C_0) \times (_6C_6) = 1$, (1&5)-domain: $(_6C_1) \times (_6C_5) = 36$, (2&4)-domain: $(_6C_2) \times (_6C_4) = 225$, and (3&3)-domain: $(_6C_3) \times (_6C_3) = 400$.

       The simulations in this study were carried out with the LAMMPS computational suite [21]. The potentials used for the β-TCP structures were derived by Demichellis et al.

[30]. The short-range interactions between all pairs were described with the Buckingham potential. The long-range interactions acted between all pairs of atoms, except those within the same phosphate tetrahedron, using Coulombic forces with a cut-off distance of 13 Å. Three dimensional periodic boundary conditions were applied to the simulation box. Systems were first relaxed by energy minimization using the conjugate gradient method [31], followed by the application of the Nosé-Hoover thermostat [32, 39] to bring the simulation box to 300 K. Using the isothermal-isobaric ensemble, simulations were performed with a combination of the Nosé-Hoover thermostat with a Martyna-Tuckerman-Tobias-Klein (MTTK) barostat [33] to maintain a temperature of 300 K and pressure of 1 bar. Simulation boxes containing $N = 2184$ atoms were equilibrated for 1 ns, followed by a production period of 1.5 ns using a 9 fs timestep.

The Kernel density estimation (KDE) technique [40] was applied to the 662 observable data set produced from the MD equilibration to visualize the bivariate relationship between the configuration energy and the lattice parameters. The Density Based Spatial Clustering of Applications with Noise (DBSCAN) clustering algorithm [41] was applied to identify densely clustered groups and remove outlier points according to the conditions set on the configuration energy. The DBSCAN clustering algorithm is sensitive to two parameters: the neighborhood radius, ϵ, and the minimal number of mutual neighbors, m. The parameters for evaluating the dataset were determined according to the performance from the perspective of Completeness using $\epsilon = 0.405$ and $m = 10$.

As each configuration is composed of a different combination of the several unit cell types, the occupation of the Ca(4) sites will subsequently be arranged differently. Therefore, the approach taken to quantify the arrangement of the Ca(4) sites is from the perspective of occupied Ca(4) sites out of the available Ca(4) sites. This is evaluated according to the following:

$$S(r) = \frac{\frac{1}{c} \sum_{i=1}^{c} x_i(r)}{N} \tag{4.1}$$

where c is the number of configurations that belong to a high density cluster, N is the number of available Ca(4) sites, x is the number of available Ca(4) sites that are occupied, and $S(r)$ is evaluated at distances r where there is a high probability of finding another Ca(4) site. Due to the ordered nature of the β-TCP crystal structure, these distances, r, are discrete and are determined to the cut-off distance of the minimum dimension of the simulation box. The $S(r)$ value captures the degree to which available Ca(4) sites are occupied, and depicts the local distribution of neighboring Ca(4) atoms relative to other Ca(4) atoms. The arrangement in which the neighboring Ca(4) sites are filled is a signature for differentiating distinct patterns. It therefore follows that configurations with similar patterns would have similar $S(r)$ values, and configurations with distinctly different patterns would be reflected in different $S(r)$ values.

4.3.3   Results

Between the different domain/unit cell configurations, the atomistic simulations lead to 662 structural outputs, each having its own relative configuration energy and lattice parameters. In order to interpret the outputs from this large parameter space, in Figure 4.7 we begin by making density plots of the results in lattice parameter a or c versus relative energy. Inspection of these plots immediately reveals that the data points are not uniformly distributed, but instead clustered into regions of higher density. More specifically, whether plotted for a or c, the maps can be partitioned into four distinct regions by their configuration energy. Going by visual inspection, we now define these regions according to the following conditions on the configuration energy: Region I: $x \leq 0.010$, Region II: $0.010 < x \leq 0.045$, Region III: $0.045 < x \leq 0.075$, and Region IV: $x > 0.075$.
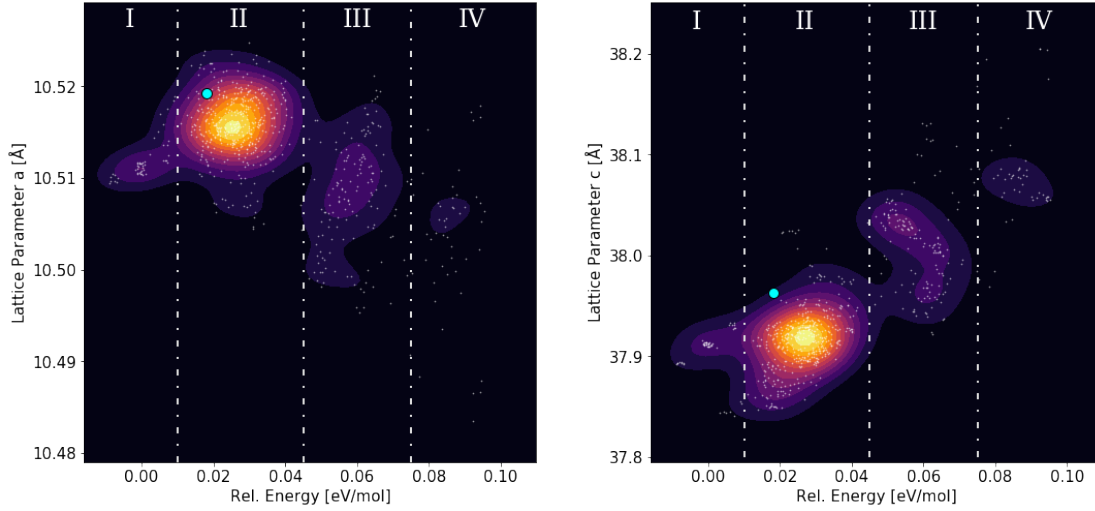
Figure 4.7 – Density maps created in the lattice parameter and relative configuration energy parameter space. Threshold values for defining the four regions are shown with dotted lines. The LEC is identified by the cyan scatter point.

Having defined these regions, we need to understand if they show discrete structural tendencies which may inform our outlook on the β-TCP crystal structure. This requires an understanding of how the configurations are distributed in the parameter space of interest. For instance, configurations with similar relative energies and similar lattice parameters must have a structural feature that connects these properties. Therefore, in order to understand what these density regions may imply, we need to segment the data such that we identify the configurations that are most similar and eliminate outliers within the given parameter space. In order to do this, the true labels are applied to each configuration according to the Region schematic they belong under. By applying the DBSCAN clustering algorithm, four clusters are refined to cover a total of 563 data points, with 99 noise points ignored, as shown in Figure 4.8. Having identified these clusters, their centroids are found in order to determine representative lattice parameters for each

region. As shown in Table 4.5, these lattice parameters clearly exemplify the following: $a_I \neq a_{II} \neq a_{III} \neq a_{IV}$, and $c_I = c_{II} \neq c_{III} \neq c_{IV}$. This study found that the LEC, which constitutes one variant of the (3&3)-domain configurations, while identified as belonging to the Region II, is found to be an outlier of the region's cluster (see Figure 4.8). It is also worth noting that numerous configurations belonging to the Region I and Region II were identified to have relative energies more stable than that of the LEC.
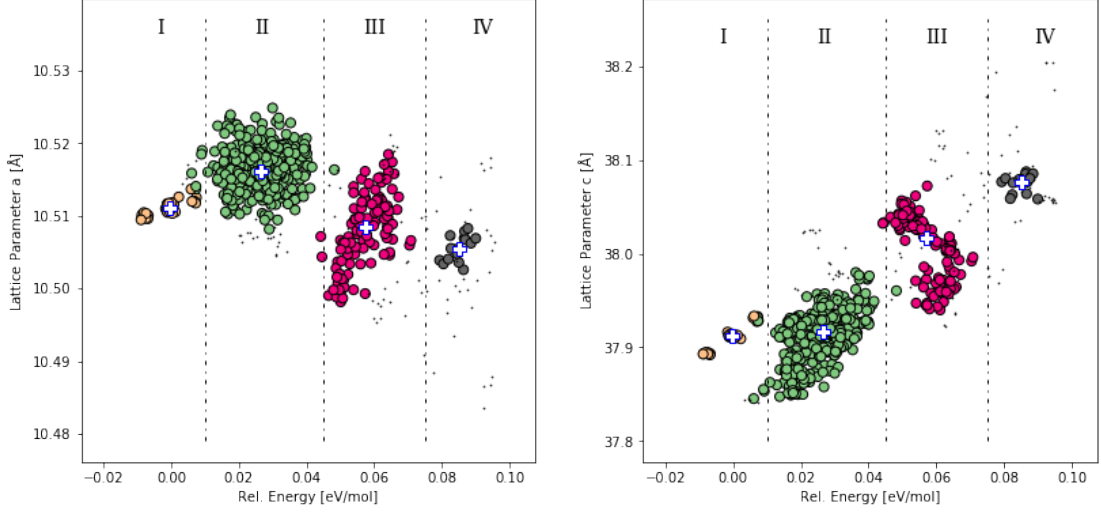
Figure 4.8 – DBSCAN-type clustering results in four clusters. Circles are colored according to their assigned clusters. Cluster centroids are shown with white crosses. Noise is represented with grey points.

Table 4.5 – Summary of the DBSCAN clustering results.

Region	Rel. Energy [eVmol]	Lattice-a [Å]	Lattice-c [Å]	Population
I	0.000	10.5111	37.912	40
II	0.027	10.5160	37.916	398
III	0.057	10.5085	38.015	110
IV	0.085	10.5055	38.077	15

The high density clustering shown in Figure 4.8 implies the clustered configurations have similar Ca(4) site arrangements. Configurations belonging to different clusters imply that the Ca(4) site arrangements are distinctly different. In order to differentiate the clustering of configurations, the local arrangement of Ca(4) neighbors is evaluated with the $S(r)$ metric in order to ascribe a quantity that is able to differentiate the clustering of configurations. The $S(r)$ values evaluated for the four regions and the LEC configuration using Equation 4.1 are summarized in Table 4.6. Distances $r = \{10.44, 18.07, 20.87\}$ represent symmetric equivalent sites related to the origin by primitive translations along

[100], [010], [110], [200], and [020], respectively. The $S(20.87)$ value of 1.00 is constant across the four regions because it results from the construction of the simulation box in the 3D-checkerboard arrangement of repeated base pairs. In order to interpret the results from the four regions, we first discuss the $S(r)$ values of the LEC, since they derive from a single unit cell configuration, rather than ordering across the entire simulation box. The $S(r)$ values of the LEC configuration are binary, either 1 or 0, labelled in Figure 4.9a. The available Ca(4) sites at distances $r = \{10.44, 13.84, 17.34, 18.07, 20.24, 20.87\}$ are fully occupied. As a result, one will always find an occupied Ca(4) site at these distances. On the other hand, the available Ca(4) sites at distances $r = \{8.68, 13.56, 17.12, 18.70\}$ are systematically vacant. To have Ca(4) distances that are systematically occupied or vacant is indicative of a highly ordered system. This corresponds to a repeating nature in the simulation box, as shown in Figure 4.9b. The occupied Ca(4) sites are arranged in the characteristic 13.8 Å separation along diagonal stripes, with the planes of the stripes being in turn separated by 9.037 Å.

Table 4.6 – Summary of $S(r)$ values.

r	Region I	Region II	Region III	Region IV	LEC
8.68	0.49 ±0.12	0.44 ±0.22	0.47 ±0.25	0.63 ±0.18	0.0
10.44	0.33 ±0.00	0.60 ±0.33	0.78 ±0.31	0.78 ±0.31	1.0
13.56	0.52 ±0.35	0.43 ±0.34	0.48 ±0.32	0.62 ±0.26	0.0
13.84	0.50 ±0.12	0.47 ±0.22	0.41 ±0.25	0.36 ±0.13	1.0
17.12	0.49 ±0.12	0.44 ±0.22	0.47 ±0.25	0.63 ±0.18	0.0
17.34	0.53 ±0.34	0.47 ±0.34	0.41 ±0.32	0.33 ±0.24	1.0
18.07	0.33 ±0.00	0.60 ±0.33	0.78 ±0.31	0.78 ±0.31	1.0
18.70	0.50 ±0.00	0.49 ±0.32	0.40 ±0.40	0.21 ±0.29	0.0
20.24	0.50 ±0.12	0.47 ±0.22	0.41 ±0.25	0.36 ±0.13	1.0
20.87	1.00 ±0.00	1.00 ±0.00	1.00 ±0.00	1.00 ±0.00	1.0

Having identified these characteristics of ordering in the LEC, we now turn our attention to the $S(r)$ analysis of the four clustered regions. Compared to a random 50% occupancy, $S(r)$ values at $r = \{10.44, 18.07\}$ are either systematically under- ($<50\%$, Region I) or over-represented ($>50\%$, Regions II - IV). Indeed, for Regions III and IV they have values of ~ 0.78, therefore approaching the value of 1 for these sites in the LEC. This indicates that configurations with a periodicity of [200] / [020] predominantly occur in Region I, whereas periodicities of [100] / [010] predominantly occur in Regions II, III, and IV. All other distances in Region I show occupancy values $S(r)$ of 50% ($\pm$ 1.2%). The $S(r)$ values of Regions II and III show that the occupancies of sites other than primitive translations are under-represented. The under-representation is more pronounced at short distances in Region II and at long distances in Region III. Region IV exhibits an accumulation of occupied sites at $S(8.67)$, $S(13.57)$, and $S(17.12)$, and

(a)   (b)
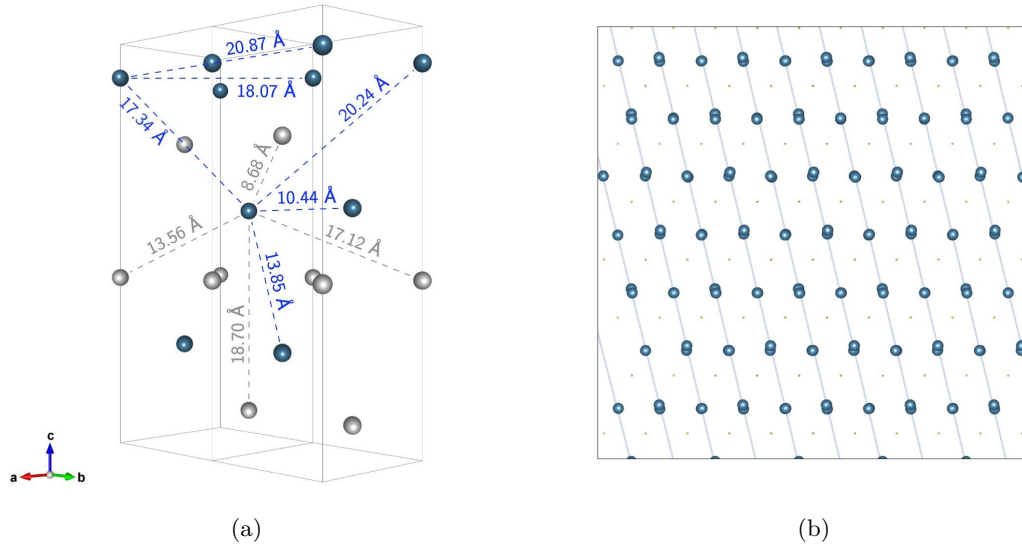
Figure 4.9 – (a) Perspective view of two LEC β-TCP unit cells, oriented to show all possible distances. For clarity, only the Ca(4) sites are shown: occupied and vacant Ca(4) sites are represented as blue and white spheres respectively. Distances to neighboring Ca(4) sites are labelled. (b) Snapshot of MD equilibrated LEC configuration, projected normal to (1 1 0) and replicated across $\sim$32 unit cells.

vacant sites at all other distances not related to the primitive translations. This suggests that, rather than being uniformly spaced, the Ca(4) sites of configurations in Regions II – IV are apportioned into groups of closely packed Ca(4) atoms. Region IV exhibits the strongest signs of grouping.

4.3.4   Discussion

This study was motivated by the hypothesis that β-TCP lattice parameters could depend on an ordering of Ca(4) site occupancy into domains, a concept that we tested by studying the energetics and lattice parameters of atomic simulation relaxation of checkerboard occupancy pairs. If correct, we would find that the mean a- and c-lattice parameter size varies according to the type of domain mixture, such that $\overline{a}_{(0\&6)} \neq \overline{a}_{(1\&5)} \neq \overline{a}_{(2\&4)} \neq \overline{a}_{(3\&3)}$, and $\overline{c}_{(0\&6)} \neq \overline{c}_{(1\&5)} \neq \overline{c}_{(2\&4)} \neq \overline{c}_{(3\&3)}$. This hypothesis did not prove valid; instead, we observe four different energetic clusters, each of which consists of multiple domain configurations. Nevertheless, the simulation analysis reveals new avenues for understanding the nature of the Ca(4) site occupancy of the β-TCP crystal structure, as now explained.

While the LEC has been identified as the most stable occupancy configuration [34–37] on the level of the single unit cell, Jay et al. stated that the β-TCP structure is more complicated, and could consist of numerous small domains formed during synthesis.

Indeed, numerous configurations with distinct cation arrangements, energetically more stable than the LEC, were identified in their larger hexagonal supercell study [34]. The simulations performed in this study similarly identify that the LEC is not the most stable configuration when considering a larger supercell, with numerous configurations composed of repeating base pairs, (0&6), (1&5), (2&4), and (3&3) being more stable. While we introduced the $S(r)$ metric to help evaluate these different possibilities, it would be useful to have a strategy for visualizing the configuration occupancies. In Figure 4.9b, we already introduced a way of visualizing Ca(4) occupancy of the LEC in the supercell system, where the structure gave a repeating pattern of diagonal stripes. We now apply the same approach to the configuration clusters identified by the DBSCAN clustering algorithm, and find that the grouping of these configurations can be understood by discerning motifs or patterns that arise from the Ca(4) site occupancy. Specifically, the domains constituting each region are found to be characterized by long-range patterning of the occupied Ca(4) sites.

We first consider Region I. When visualized on the level of the supercell, the Region I configurations are found to have a shared characteristic, in that the Ca(4) atoms are arranged in planes of varying herringbone patterns separated by 18.7 Å. The Ca(4) sites of selected configurations of Region I, shown in Figure 4.10, highlight the variations of the herringbone motif. These variations become apparent by considering the number of Ca(4) ions between a junction in the herringbone pattern. Using Figure 5a as an example, the basic building block of this herringbone pattern features two Ca(4) ions between each junction. Therefore, the repeating unit of Figure 4.10a is labelled as —$[2\text{–}2]_n$. A couple variations of the repeating unit of a herringbone pattern are —$[2\text{–}6]_n$ and —$[2\text{–}2\text{–}3\text{–}3]_n$, shown in Figure 4.10b and Figure 4.10c, respectively. It appears the herringbone pattern arranges the occupied Ca(4) sites such that the available sites are on average 50% occupied. Further, this 50% occupation of the available sites at a majority of the distances has a stabilizing effect that makes these configurations the most energetically favorable in the parameter space explored.

Similar to the Region I configurations, the herringbone planes are also discernible for the Region II configurations. However, what differentiates Region II configurations from Region I configurations, is the interruption of the herringbone planes by an exchange of a vacant Ca(4) site for a Ca(4) atom. This is adopted in the notation of the repeating unit by denoting an X where there is a vacant Ca(4) site. It is worth noting the variations of the interrupted herringbone motif of Region II with the base units of —$[3\text{–}2\text{–}2\text{–}(1\text{–}X\text{–}1)]_n$, —$[(3\text{–}X)\text{–}(X\text{–}3)]_n$, and —$[4\text{–}(2\text{-}X\text{–}1)]_n$, shown in Figure 4.11. By interrupting the herringbone pattern with a vacant Ca(4) site, the relative energies of the configuration centroid is increased by 0.027 eV. It is quite apparent that, by featuring these planes of vacant Ca(4) sites that break the continuity of the herringbone pattern, an energetic penalty is introduced.

(a)	(b)	(c)

Figure 4.10 – Selected Region I configurations replicated across ∼32 unit cells, and projected normal to (1 1 0). Only the Ca(4) sites are shown, with the occupied sites as the blue balls and the vacant sites as the golden points. The patterns of the occupied Ca(4) sites, highlighted with blue lines, emphasize the variable herringbone patterns: (a) —$[2\text{–}2]_n$, (b) —$[2\text{–}6]_n$, and (c) —$[2\text{-}2\text{-}3\text{-}3]_n$.

In comparison to the herringbone patterns of Region I and II, Ca(4) ordering in Regions III and IV is less obvious. The bands of vacant Ca(4) sites, which were a discernible feature in the Region II configurations, is more prominently seen in the Region III and IV configurations. This layering motif, that closely confines the Ca(4) atoms between horizontal bands of vacant sites (Figure 4.12 and 4.13), is reflected in the determined $S(r)$ values of these regions. Similar to Region II, an energetic penalty is introduced by featuring these layers of vacant Ca(4) sites. By losing the herringbone characteristic and adopting slabs of vacant and occupied Ca(4) sites, Region III and IV configurations have higher centroid energies of 0.057 and 0.085 eV, respectively, relative to Region I.

Tied to the characteristic Ca(4) occupancy motifs identified for the four regions are changes in the unit cell lattice a- and c-parameters and energetics of the cluster centroids. The determined lattice dimensions of the higher energy Region III and IV configurations have shorter a-lattice sizes and elongated c-lattice sizes compared to the lower energy Region I and II configurations. This observation from the simulations can draw a parallel to the experimental observation of two distinct domain lattice parameter pairs for the Ca:P ratio of 1.5, in which one of the domains had a smaller a-lattice parameter and a longer c-lattice parameter by 0.0021 Å and 0.0133 Å, respectively [38]. That is, by going beyond the level of the single unit cell to considering the possibility of longer range ordering of the Ca(4) occupancy, domains of the same Ca:P ratio can indeed be predicted to have discrete energetics and lattice parameters, in correlation with the surprising experimental results.

<div align="center">(a)   (b)   (c)</div>
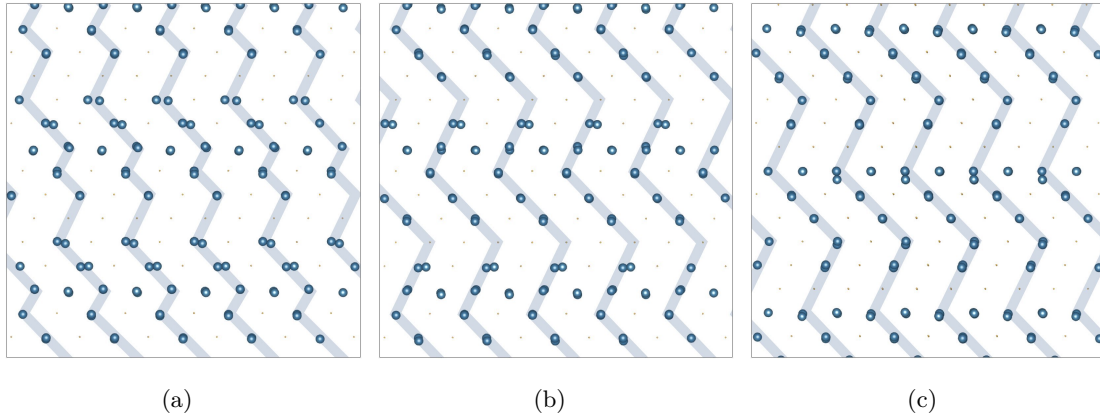
Figure 4.11 – Selected Region II configurations replicated across $\sim$32 unit cells, and projected normal to (1 1 0). Only the Ca(4) sites are shown, with the occupied sites as the blue balls and the vacant sites as the golden points. The patterns of the occupied Ca(4) sites, highlighted with blue lines, emphasize the variable herringbone patterns: (a) —[3–2–2–(1–X–1)]$_n$, (b) —[(3–X)–(X–3)]$_n$, and (c) —[4–(2-X–1)]$_n$.

<div align="center">(a)   (b)   (c)</div>
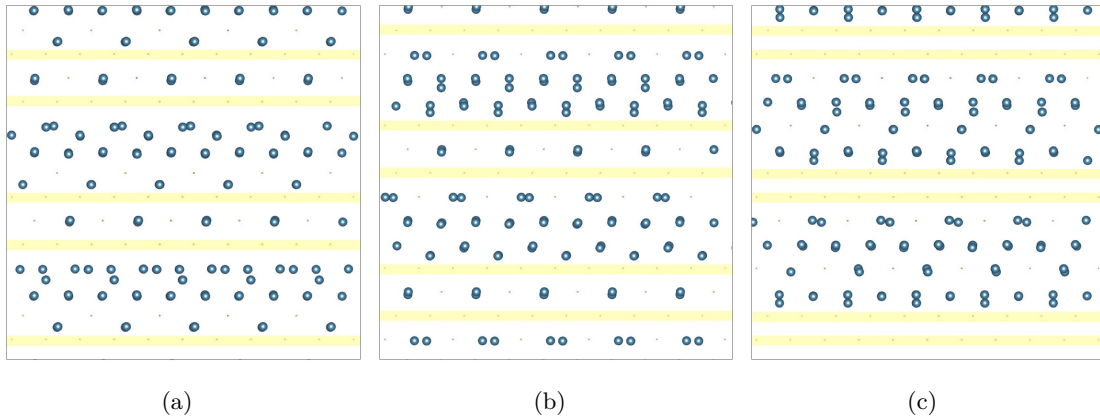
Figure 4.12 – Selected Region III configurations replicated across $\sim$32 unit cells, and projected normal to (1 1 0). Only the Ca(4) sites are shown, with the occupied sites as the blue balls and the vacant sites as the golden points. Bands of vacant Ca(4) sites are highlighted with yellow lines.

Going further with this discussion, our analysis also suggests that such discrete structural domains could be associated with characteristic long-range patterning of the Ca(4) site occupations. Such a possibility is advanced by Figures 4.10 to 4.13 covering common motifs from our simulations, with the herringbone nature of Regions I and II and the slab layering of occupied and vacant sites in Regions III and IV. Nevertheless, care must be taken in considering these identified motifs too "literally". This is because the checkerboard unit cell domains that we set up for charge neutrality inherently have a certain structure or repetition that could in turn influence the ordering outcome. The key point to consider is instead that patterning of the occupied Ca(4) sites on the longer range
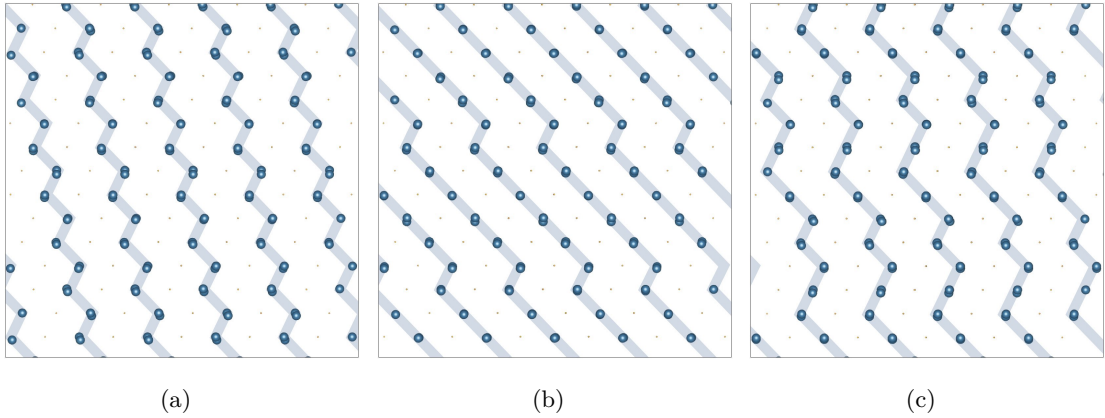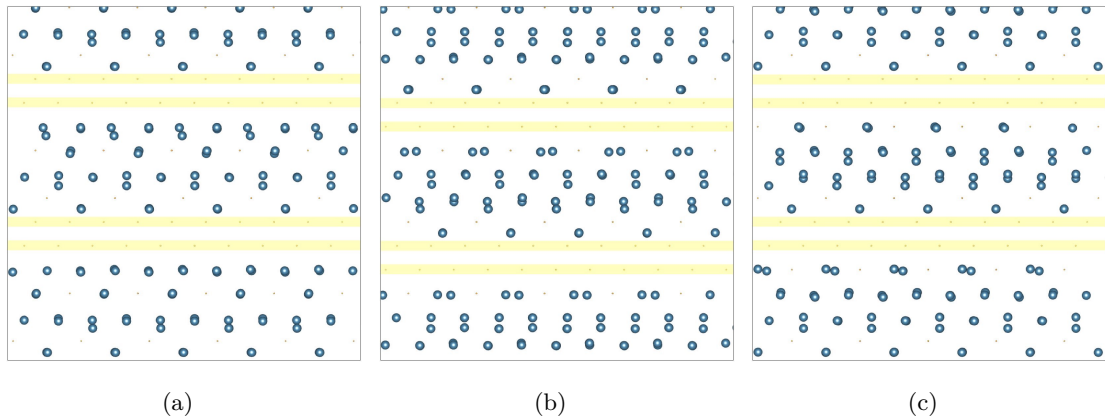
Figure 4.13 – Selected Region IV configurations replicated across ∼32 unit cells, and projected normal to (1 1 0). Only the Ca(4) sites are shown, with the occupied sites as the blue balls and the vacant sites as the golden points. Bands of vacant Ca(4) sites are highlighted with yellow lines.

distances of a supercell can both lead to lower structural energetics than when considering configurations only on the level of the unit cell, and that these could be tied to discretely different lattice parameters that correlate to experimental findings. Such tendencies would also be consistent with the experimental structural studies, where synchrotron and XRD data are neither commensurate with fully random Ca(4) site occupancy nor fully ordered (such as the LEC unit cell structure). Conceivably, while the β-TCP lattice is forming, it could fall into different local energetic minima, each having certain types of Ca(4) occupancy patterning and unit cell parameters. Experimentally, there are significant challenges in translating the simulation results into structural determination expectations from, say XRD analysis. That is, the simulation output cannot be straightforwardly used "to drive" a Rietveld analysis. One potential solution to this challenge would be to leverage the $S(r)$ values, by comparing them to Ca atomic pair distribution functions (PDF) measured using synchrotron X-ray [42]. This is a possibility that is being considered for future work.

In order to bypass the potential influence of the periodic nature of the checkerboard domain atomistic simulations, a Monte Carlo atom-swapping simulation approach of occupied and vacant Ca(4) sites over larger supercells could be interesting [43, 44]. From the results presented here, it could be hypothesized that local regions of these simulations will collapse into different patterns of Ca(4) site occupancy upon supercell equilibration. Such an analysis is tested in the next section.

4.3.5 Conclusion

This work explored the parameter space of 662 configurations that were composed of "checkerboard" domain arrangements that appropriately combined seven types of unit

cells. The parameter space resulting from molecular dynamics simulations revealed numerous aspects that lend better insight into the nature of the Ca(4) site of the β-TCP crystal structure. The simulation results revealed high density clustering of configurations that could be differentiated into regions. In order to understand the formation of the clusters, two concepts were introduced to study potential long-range ordering of the Ca(4) sites: motif identification and the $S(r)$ metric. It was realized that the clusters are composed of configurations that have similar Ca(4) site arrangements. Although the arrangements may have slight variations from configuration to configuration, they will belong to similar regions if their Ca(4) sites follow a similar motif. This particular parameter space identified two motifs: the varying planes of herringbone configurations and the layering of the occupied and vacant sites.

The identified patterns of each region were differentiated by the $S(r)$ method that evaluates the number of available Ca(4) sites that are occupied at discrete distances where there is a high probability of finding another Ca(4) site. The $S(r)$ values reveal the configurations of Region I arrange the Ca(4) sites such that, on average, 50% of the available sites are occupied (except for at distances $r = \{10.44, 18.07, 20.87\}$). This particular arrangement, which is represented as the herringbone patterns, is more energetically stable than the popularly used LEC. In fact, numerous 'checkerboard' arrangements composed of the (0&6)-, (1&5)-, (2&4)-, and (3&3)-domains were found to be more stable than the LEC. This indicates that the ideal characteristic of the Ca(4) site cannot be captured across a single unit cell occupancy, but could possibly be a combination of all seven types of unit cells. While the results of these molecular dynamics simulations do not directly explain the observed discontinuity in the a- and c-lattice parameters reported by Le Gars Santoni et al., the tools introduced can be applied in future simulation studies that may better explain the Ca(4) site occupancy of the β-TCP crystal structure.

4.4 Resolving the partially occupied sites of the β-TCP crystal structure by Monte Carlo simulations

4.4.1 Introduction

The previous sections have highlighted that the energetic stability of the β-TCP structure is dependent on the arrangement of the partially occupied Ca(4) site. Section 4.1 highlighted the 20 possible configurations of a single β-TCP unit cell (u.c.) that could be grouped into three energetic classes: the low energy configuration (LEC), intermediate energy configuration (IEC), and high energy configuration (HEC). Section 4.2 created various supercell systems that combined the energetic configurations (LEC, IEC, HEC) and found some configurations were more stable than the supercell composed solely of LECs, suggesting a longer range ordering or clustering of the Ca(4) site could be important. Section 4.3 explored a new perspective of the β-TCP unit cell inspired by experimental findings. Instead of maintaining a 50%-partial occupancy of the Ca(4) site within the unit cell, the 50%-partial occupancy could be globally maintained with a larger supercell system that combines Ca(4) deficient and Ca(4) rich unit cells. As a result, a consistent motif was observed in the patterning of the Ca(4) sites (planes of herringbone patterns, bands of vacancies).

This section will build off the idea that the Ca(4) site could be arranged in patterns that span across multiple unit cells, by exploring larger supercell systems. A Monte Carlo (MC) approach is taken, with the aim of finding the optimum arrangement(s) of the Ca(4) site over long distances. The MC method is ideal for investigating larger systems as it removes the human bias when probing a multitude of configurations. However, there is always the possibility of infrequent crossings of high energy barriers between local energy minima in MC simulations. This can lead to trapping in local minima over long periods during the sampling process. One method to overcome this problem includes parallel tempering or the replica exchange method (REM) [45–47], which is implemented in the simulations of this section.

4.4.2 Computational Method

To explore the Ca(4) site at longer ranges we created a supercell system containing 13,248 ions (48 u.c.). This was the largest supercell system that could be successfully created in METADISE [20]. In order to probe even longer length scales, this base 48 u.c. supercell system was replicated $n = \{2, 3, 4\}$ times. Therefore, MC simulations were undertaken on four β-TCP supercell systems comprising 13,248 ions (48 u.c.), 26,496 ions (96 u.c.), 39,744 ions (144 u.c.), and 59,064 ions (216 u.c.). All supercell systems were initialized from the LEC arrangement of the Ca(4) site using the crystal structure published by Yashima et al [28]. These initial crystal structures introduce a placeholder atom that
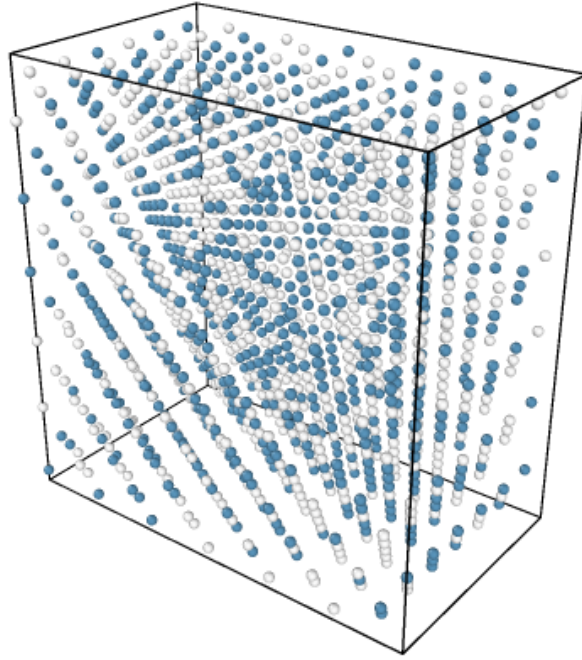
Figure 4.14 – Snapshot of the 216 u.c. system for the 300 K replica. For clarity, only the occupied Ca(4) sites (blue spheres) and placeholder atoms representing the vacant Ca(4) sites (white spheres) are shown.

does not interact with the system (charge $q = 0$) to represent the Ca(4) site point defect vacancy in the simulation.

All calculations were performed with the DL_MONTE computational suite [22, 23]. The total long-range electrostatic energy was evaluated using the Ewald summation as periodic boundary conditions were employed. The potentials employed have been successfully used in the previous sections (Sections 4.1, 4.2, and 4.3), being the force field introduced by Demichelis et al. [30] in their study of calcium phosphate systems, and implemented with a cut-off of 13.0 Å. The Monte Carlo cycle applied allows for the pairwise exchange of the Ca^{2+} ion occupying a Ca(4) site (Ca(4)$_{occ}$) and a placeholder atom representing a "vacant" Ca(4) site (Ca(4)$_{vac}$), both of which are chosen at random. The parallel replica exchange method was implemented to make sure the simulation did not become trapped in a local minimum. This was done with eight replicas at temperatures between 300 K to 1350 K, separated by 150 K. The target temperature of 1350 K was chosen to approximate the experimental sintering temperature of 1100℃ (1373.15 K). A swap between adjacent replicas was attempted every 100 steps. Each calculation consisted of an initial equilibration followed by subsequent production cycles. A snapshot of the Ca(4) sites from the MC trajectory of the 216 u.c. system is shown in Figure 4.14.

Although the largest simulation box of 216 u.c. contains a total of 59,064 ions, the structural degrees of freedom are significantly lowered considering the only MC move is the pairwise exchange of the Ca(4)$_{occ}$ and the Ca(4)$_{vac}$, which consists of 1,284 ions.
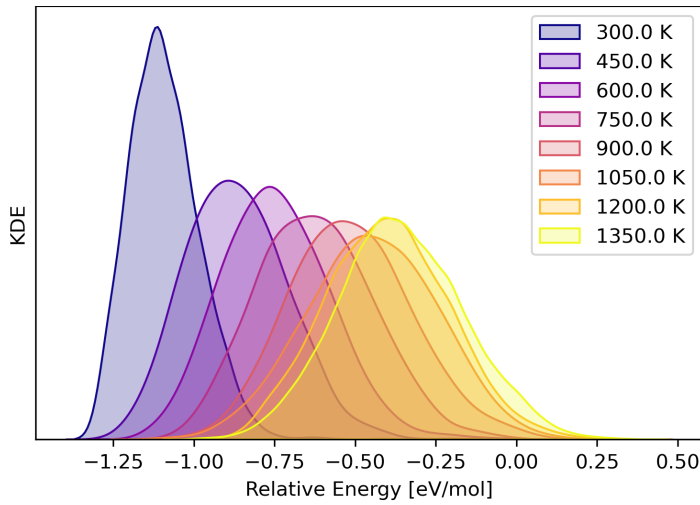
Figure 4.15 – Energy distribution of the eight replicas from the MC simulation of the 216 u.c. system.

As a result, eight replicas were adequate to cover the temperature range between 300 K and 1350 K with a non-vanishing acceptance ratio for the replica exchange. This point is illustrated with the sufficient overlap of the energy distributions of adjacent replicas in Figure 4.15.

4.4.3   Results & Discussion

Simulating these extremely large supercell systems presents a core challenge of segmenting the simulation outputs such that the resulting Ca(4) site arrangements can be interpreted. The first strategy in interpreting the Ca(4) sites was to consider the seven unit cells, introduced in Section 4.3, that range in the number of Ca(4)$_{\mathrm{occ}} = \{0, 1, 2, 3, 4, 5, 6\}$, again summarized in Table 4.4. The presence of the seven unit cells was determined by dividing the four supercell systems into composing base unit cells. Within each unit cell, the number of Ca(4)$_{\mathrm{occ}}$ ions was determined. This approach is illustrated in Figure 4.16a, which represents the 216 u.c. system as a grid. Each cell of the grid represents a u.c. and is colored according to the number of occupied Ca(4) sites.

Table 4.4 – Unit cells with varying occupied Ca(4) sites

Filled Ca(4) sites (n)	0	1	2	3	4	5	6
Ca:P	1.429	1.452	1.476	1.500	1.524	1.548	1.571
$_6C_n$	1	6	15	20	15	6	1

(a)   (b)
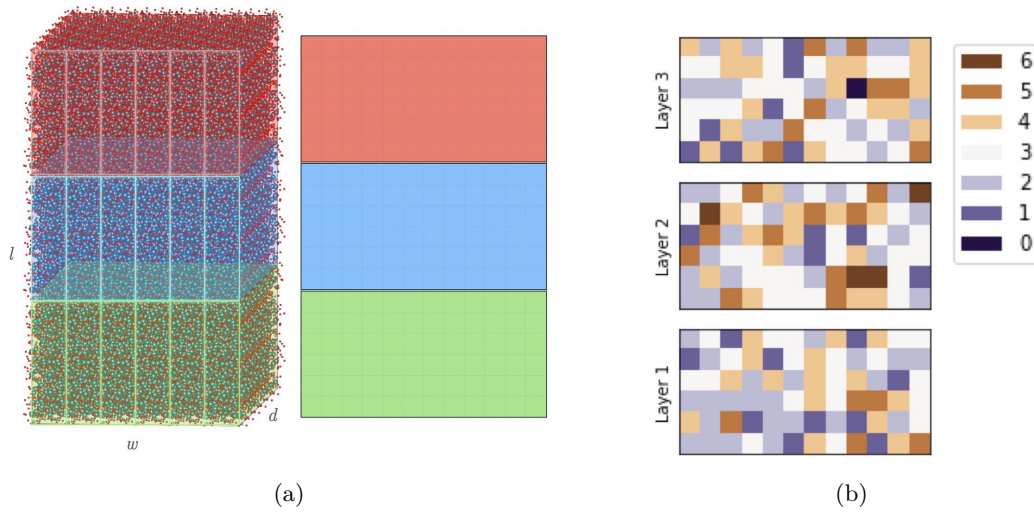
Figure 4.16 – (a) Grid representation of the 216 u.c. system. (b) Color coded grid according to the determined number of occupied Ca(4) sites per unit cell.

At this point, it is worth recalling that in Section 4.3, an average Ca:P = 1.50 was maintained by pairing each type of the seven unit cells with its complement: (0&6), (1&5), (2&4), (3&3). Subsequently, the systems investigated patterned the paired unit cells in a 3D-checkerboard arrangement. We now try to draw a parallel by observing if this checkerboard arrangement is present in the supercell systems. This was mainly achieved through visual observation of the resulting grids, an example of which is presented in Figure 4.16b. Although the presence of the seven unit cells is observed, there is no obvious grouping or patterning (in 3D-checkerboard arrangement as presented in Section 4.3) of the four domains. However, it is clear that the MC produced configurations are not solely composed of the Ca(4)$_{\text{occ}}$ = 3 unit cell. This suggests that the traditional definition of the β-TCP unit cell with 50%-partial occupancy of the Ca(4) sites is not entirely accurate.

The four supercell systems are broken down into the fractional composition by each of the seven unit cell types. The represented average of 1000 structures collected during the data production is shown in Figure 4.17. It is clear there is a symmetric distribution of the seven unit cells, with a preference to feature the Ca(4)$_{\text{occ}}$ = 3 unit cell, which represents approximately 31% of the unit cells in each of the four supercell systems. Considering that 69% of the unit cells therefore do not feature Ca(4)$_{\text{occ}}$ = 3, there is clearly also a tendency for many unit cells to be Ca-rich and Ca-deficient. The Ca(4)$_{\text{occ}}$ = $\{2, 4\}$ unit cells make up about 23% of the four supercell systems. The Ca(4)$_{\text{occ}}$ = $\{0, 1, 5, 6\}$ are also featured, but appear less frequently. The four supercell systems are only composed of $\sim$10% Ca(4)$_{\text{occ}}$ = $\{1, 5\}$ and $\sim$1% Ca(4)$_{\text{occ}}$ = $\{0, 6\}$. In fact, the composition of the supercell systems seems to follow the combinatorial distribution of possible unit cell types summarized in Table 4.4. There are a total of 64

possible combinations when considering the seven unit cells. If this distribution is then followed, the $Ca(4)_{occ} = 3$ would be the most represented unit cell in a bulk system, as it makes up 31.25% (= 20/64) of the possible configurations. When extended to the other unit cells, the $Ca(4)_{occ} = \{2, 4\}, \{1, 5\}, \{0, 6\}$ unit cells make up 23.4375%, 9.3750%, and 1.5625% of the possible combinations, respectively. These values are all very close to the unit cell composition distributions identified with the MC supercell simulations.
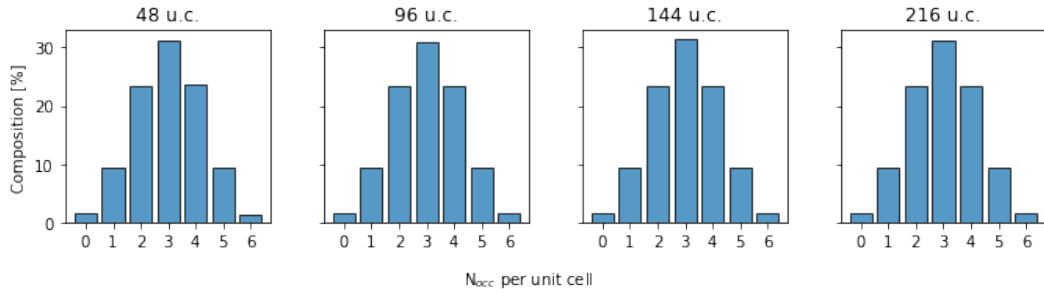
Figure 4.17 – Histograms of the four simulation boxes showing the composition breakdown with the seven unit cells.

Patterns of the $Ca(4)$ site occupation were a common theme of Section 4.3. The configurations probed could be grouped into energetic regions according to the configuration patterns of the $Ca(4)$ site occupation. Here, we recall the contrast between the Region I configurations (Section 4.3, Figure 4.10), which featured planes of various herringbone patterns, and the Region IV configurations (Section 4.3, Figure 4.13), which featured horizontal bands of vacancies. As a metric to explain why one pattern was more energetically stable than another, the approach taken quantified the arrangement from the perspective of occupied $Ca(4)$ sites out of the available $Ca(4)$ sites. This was evaluated with the Equation 4.1 of Section 4.3:

$$S(r) = \frac{\frac{1}{c}\sum_{i=1}^{c} x_i(r)}{N} \tag{4.1}$$

where c is the number of configurations that belong to a high density cluster, N is the number of available $Ca(4)$ sites ($Ca(4)_{avail}$), x is the number of available $Ca(4)$ sites that are occupied ($Ca(4)_{occ}$), and $S(r)$ is evaluated at distances r where there is a high probability of finding another $Ca(4)$ site. The distances r were determined from the peaks of the radial distribution function of $Ca(4)_{avail}$—$Ca(4)_{avail}$.

Now we apply the same metric for analyzing the output of the MC simulations. The $S(r)$ values evaluated for the four supercell systems of the $T = 300$ K replica using Equation 4.1 are shown in Figure 4.18. In each case, the simulation boxes show that $S(r) \approx 0.50 \pm 0.02$ for all distances r, except for a slight deviation near the limits of the simulation box. A consistent value of $S(r) = 0.5$ indicates that the configurations produced by the MC simulations have the $Ca(4)$ sites ordered such that the available $Ca(4)$ sites are on average half-occupied, even though the occupation varies per constituent unit

cell (Figure 4.17). This trend is maintained from the 48 u.c. to the 216 u.c. simulation box. Such a result indicates that, while each Ca(4) site is still randomly 50% occupied, the randomness is applied on the scale of the supercell, not the unit cell. That is, half of the sites in the supercell are occupied, but there is no need for the individual unit cells to maintain the "3 out of 6" rule. In regards to the Ca(4) site, for the calcium ions there is no unit cell description, just a generalized domain. This can potentially explain the incommensurate nature of the XRD pattern analysis, since a Rietveld analysis only considers the unit cell scale and symmetry, not longer-range effects.

It is worth mentioning that there are some limitations to the $S(r)$ analysis. While this approach is useful in describing the Ca(4) site arrangements in the long range, it could possibly be blind to patterning occurring on the local scale. A different approach is needed to address this concern but, given the challenges of developing a suitable approach, this beyond the scope of this thesis and instead a question for future studies. Nonetheless, it is clear that the $S(r)$ values of the four MC supercell systems are very different to the $S(r)$ signature of the LEC configuration. The values of the LEC are binary with $S(r) = \{0, 1\}$. This indicates that the LEC has a highly ordered arrangement of the Ca(4) site occupancy that repeats over a long range, which can be observed in the planes of diagonal striping of occupied Ca(4) sites. Relative to this, it is clear that the Ca(4) sites of the four MC supercell systems are not highly ordered.

Continuing on the theme of short-range local arrangements, the $S(r)$ values of the MC produced systems are most similar to the $S(r)$ values of Region I. Due to the substantially smaller dimensions of the simulation boxes created in Section 4.3, the $S(r)$ values are capped at the minimum dimension of the simulation box at $r = 20.87$. The $S(r)$ values at $r = \{10.44, 18.07\}$ were significantly under-represented, and all other distances have $S(r)$ values of 0.50 ± 0.17 for Region I. It was observed that the Ca(4) sites were arranged in planes of various herringbone patterns to obtain this Region I signature. Visual inspection of simulation outputs finds that the Ca(4) sites of the four MC simulation systems do not appear to be arranged in a repeating pattern. If there was a pattern, it is not strikingly obvious in the four simulation boxes. This presents two options: (1) there is a pattern but the repeating unit extends beyond the dimensions of the simulation box or (2) there is no pattern and the Ca(4) site is pseudo-random in order to maintain half-occupancy of the available sites. It is worth keeping in mind that the largest supercell system has dimensions $\{l, w, d\} = \{108.50 \text{ Å}, 62.61 \text{ Å}, 112.21 \text{ Å}\}$. The largest dimension probed in this study (0.011 μm) is significantly smaller than the typical reported β-TCP grain size [48] (small: 1.3 μm, large: $\sim$3.3 μm). Further experiments are needed in to resolve the two options. As already proposed in Section 4.3, one analytical avenue towards this could be acquisition of, and comparison to, experimental atomic pair distribution functions (PDF) for Ca using synchrotron radiation
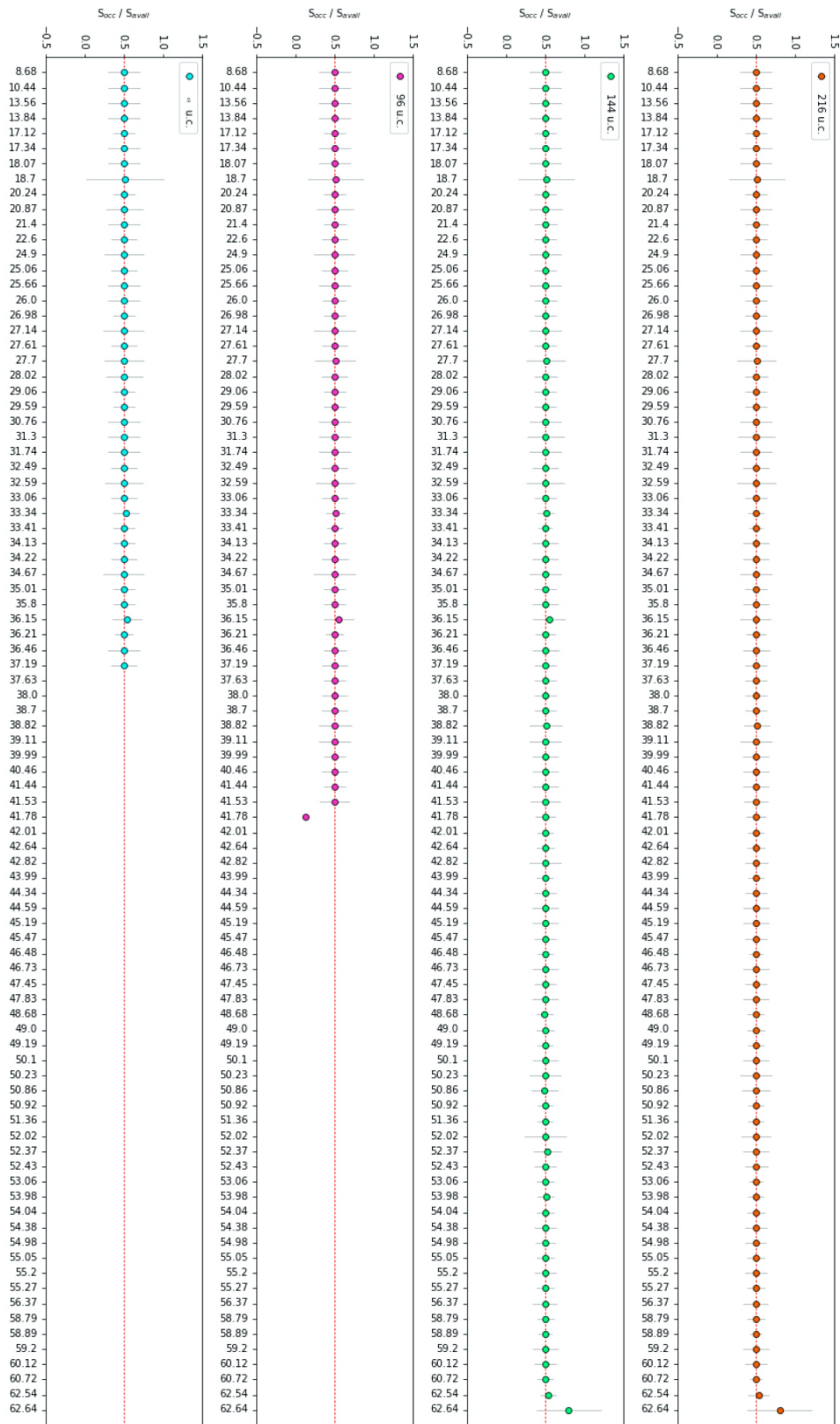
Figure 4.18 – $S(r)$ values for the 48 u.c., 96 u.c., 144 u.c., and 216 u.c. system.

4.4.4 Conclusions

The work presented in this section used the REM MC approach to investigate the optimal occupation arrangements of the Ca(4) site in the β-TCP crystal structure. The core challenge presented with analyzing the MC-produced configurations was being able to appropriately segment the structures such that the Ca(4) site occupancy could be interpreted. The approach taken relied mainly on the tools presented in Section 4.3. The take-away points from the analysis are summarized as follows:

- The MC simulations show the presence of seven unit cell types with a range of Ca(4) site occupancy. These seven unit cell types are distributed in a manner that mirrors the number of possible unit cell combinations, which must be linked to the configurational entropy.

- Although the Ca(4)$_{\mathrm{occ}}$ = 3 unit cell is predominantly featured in the four supercell systems, Ca-rich and Ca-deficient cells are also present. This suggests that the nature of the Ca(4) site cannot be correctly described within a single unit cell.

- The four supercell systems were found to have $S(r)$ values of 0.5 at all distances r, with a slight deviation at the limits of the simulation boxes. The evaluated $S(r)$ values of the four supercell systems were found to be most similar to the $S(r)$ values of Region I in Section 4.3.

- However, there was no obvious patterning of the Ca(4) sites (for instance, the signature planes of varying herringbone patterns for the Region I configurations of Section 4.3). This perhaps confirms that the repeating patterns presented in Section 4.3 are an artifact resulting from the supercell construction in the 3D-checkerboard arrangement.

Although the results of these MC results are enlightening towards understanding the Ca(4) site occupancy of the β-TCP crystal structure, further analysis is needed to determine if there is either a repeating pattern of the Ca(4) site occupancy that extends beyond the dimensions of the simulation box, or that the Ca(4) site occupancy is pseudo-random (i.e. random on the scale of the supercell). As well as development of a suitable metric or algorithm to identify local Ca(4) site occupancy patterning within supercells, another possible avenue for future studies is acquisition of, and correlation to, experimental PDF data acquired using synchrotron radiation.

5 | Sr-doped β-TCP: from atomistic simulations to electron microscopy

Osteoporosis is the most common bone disease in humans. It affects more than an estimated 200 million people worldwide, and its prevalence will only increase as the aging population lives longer life spans [49]. Osteoporosis is characterized by an increase in bone fragility and the deterioration of bone microarchitecture [50]. Its occurrence is associated with an imbalance in the dynamic and coordinated bone remodeling process: the rate of bone loss via osteoclastic resorption exceeds the rate of bone formation by osteoblast synthesis [51]. In recent decades, the drug strontium ranelate has been used for treating osteoporosis. The novelty of this drug, compared to other antiosteoporotic drugs, is its dual mode of action on affecting the bone remodeling process: it simultaneously promotes bone formation by osteoblasts and inhibits bone resorption by osteoclasts, thereby inducing positive bone balance [50, 52–55].

The unique effects of strontium ranelate has stimulated growing interest in strontium as an ion of biological significance. Various studies have investigated the incorporation of strontium into bone replacement materials, such as β-TCP and hydroxyapatite (HA), as an approach to tailoring the biological properties of these materials. The substitution of strontium (Sr^{2+}) has been shown to shift the bone remodeling balance towards bone formation by increasing osteoblast proliferation [56–58] and suppressing osteoclast differentiation [59, 60]. Strontium has also been shown to improve bioactivity and osteoinductivity. A study by Roy and Bose showed the SrO-incorporated β-TCP not only enhanced *in vitro* cell attachment and growth, but also improved the *in vivo* biocompatibility [61]. These studies highlight the effectiveness of strontium in adjusting the bone-remodeling process.

Considering the beneficial effects of strontium, it is important to identify the precise location of strontium in the β-TCP microstructure in order to draw conclusions on the mechanism of action on the bone remodeling process. In this chapter, we investigate the localization and distribution of Sr ions in Sr-doped β-TCP across grain boundaries using molecular dynamics and Monte Carlo simulations, in combination with experimental

characterization by analytical electron microscopy. The framework for these studies is detailed as follows:

- **Section 1** – This section studies the incorporation of Sr^{2+} into the β-TCP crystal lattice using molecular dynamics. Various properties are evaluated with an appropriately chosen force field. The agreement of these calculated properties with other simulations and experimental values confirms these potentials can be used for future sections.

- **Section 2** – A framework for investigating β-TCP as interface structures will be presented in this section, by introducing the methodology for creating surface and grain boundary structures. The approach to addressing the complexity of the Ca(4) site (previously described in Chapter 4) will be discussed. The section concludes by detailing the implications of randomly selecting the occupied Ca(4) site on the distribution of Sr^{2+} ions.

- **Section 3** – Monte Carlo simulations are employed, using the potentials of Section 5.1, to determine the distribution of Sr^{2+} across various surfaces and grain boundaries.

- **Section 4** – Analytical electron microscopy analysis of Sr-doped β-TCP powders and ceramics. The results of Section 5.3 from the atomistic simulations will be compared to those from experimental characterization techniques, in an effort to explain the in vitro findings of Sr-doped β-TCP .

5.1   Single & multi-substitution study of Sr-doped β-TCP

Although most interatomic potentials for introducing dopants into calcium phosphate systems have been developed for hydroxyapatite, Pedone et al. demonstrated potentials parameterized for hydroxyapatite were transferable to other calcium phosphate systems [62]. With this in mind, the parameters chosen to describe the strontium (Sr^{2+}) interaction in the β-TCP crystal lattice are a combination of two force fields. The first potential set is the standard calcium phosphate force field derived by Demichellis et al. [30] that has been previously used to simulate the β-TCP crystal structure in Chapter 4. The second potential set, derived by Rabone and DeLeeuw [63], defines the $Sr–O_{Phos}$ interaction for natural apatite crystals. The Sr–P interaction was determined by applying a scaling argument that assumes the ratios of the potential parameters for a cation with two different anions are the same for different cations, as shown by the following equation:

$$A_{(Sr–P)} = A_{(Sr–O_{Phos})} \times \frac{A_{(Ca–P)}}{A_{(Ca–O_{Phos})}} \tag{5.1}$$

where $A_{(Ca–O_{Phos})}$ and $A_{(Ca–P)}$ are the potentials derived by Demichelis et al. [30] and $A_{(Sr–O_{Phos})}$ was derived by Rabone et al. [63]. The determined Buckingham potentials used to describe the Sr–P interaction were as follows, with A [eV] and ρ [Å] equal to 1405.4387 and 0.387208, respectively.

As this combined potential set will be the keystone for further atomistic simulations it is important to assess its performance across a set of benchmarks. The following section applies the β-TCP force field with the derived parameters for strontium in molecular dynamics simulations to investigate the substitution of Sr^{2+} in place of Ca^{2+}. The molecular dynamics simulations performed will evaluate the site preference of strontium substitution, up to 80 at.% into the β-TCP crystal lattice. The site preferences of strontium substitution were evaluated and explained by the local coordination environment. The energetics of the sites were used to determine the "filling" order up to 80 at.% in the β-TCP crystal structure. From the varying degrees of strontium substitution, various properties (lattice parameters and reaction enthalpies) are reported and compared to experimental data.

5.1.1   Computational method

The simulations in this study were carried out with the LAMMPS computational suite [21]. The short-range interactions between all pairs of ions were described with the Buckingham potential. The long-range interactions acting between all pairs of atoms (except those within the same phosphate tetrahedron) use Coulombic forces with a cut-off distance of 13 Å. Three-dimensional periodic boundary conditions were applied to the simulation box. Systems were relaxed by energy minimization using the conjugate gradient method [31], then thermostatted to 300 K using a Nosé-Hoover thermostat [32, 39]. Using the

isothermal-isobaric ensemble, simulations were performed with a combination of the Nosé-Hoover thermostat with a Martyna-Tuckerman-Tobias-Klein (MTTK) barostat [33] to maintain a temperature of 300 K and pressure of 1 bar. Simulation boxes containing $N = 1092$ atoms were equilibrated for 1 ns, followed by a production period of 2 ns using a 9 fs timestep.

5.1.2   The β-TCP crystal structure

Previous studies [34, 36, 37] have found that the lowest energy configuration (LEC) for a single β-TCP unit cell separates the Ca(4) atoms by 13.8 Å. Although Chapter 4 identified the LEC as an inaccurate description of the Ca(4) site in the β-TCP crystal structure, this configuration is still considered the standard crystal structure for most theoretical studies of β-TCP. For this reason, all calculations in this study assume this low energy configuration of the Ca(4) site to describe the β-TCP crystal structure, in order to compare our results to other computational studies. The LEC arrangement of the Ca(4) atoms lowers the symmetry of the Ca sites from five to nine [35], as labelled in Figure 5.1.

5.1.3   Site dependent stability of Sr^{2+}

Since the LEC configuration of the β-TCP crystal structure contains nine inequivalent Ca sites, the stability of strontium substitution depends on the Ca site being substituted. To determine the energetic favorability of each Ca site, a single Sr^{2+} atom was substituted in place of a Ca^{2+} atom in the β-TCP crystal structure at each of the nine Ca-sites: Ca(1)-1 ($n = 9$), Ca(1)-2 ($n = 9$), Ca(2)-1 ($n = 9$), Ca(2)-2 ($n = 9$), Ca(3)-1 ($n = 9$), Ca(3)-2 ($n = 9$), Ca(4) ($n = 3$), Ca(5)-1 ($n = 3$), and Ca(5)-2 ($n = 3$). The MD-equilibrated energies of each site are plotted relative to the most stable substitution site in Figure 5.2. It can be seen that the most favorable substitution site for strontium is the Ca(4) site, followed by a small energetic penalty to substitute at the Ca(3)-2 site. There are similarly larger energies to substitute at the Ca(1)-1,2, Ca(2)-1,2, and Ca(3)-1 sites. The Ca(5)-1,2 sites are highly unstable substitution sites for strontium. These results are similar to the single substitution Density Functional Theory (DFT) study performed by Matsunaga et al. [35].

5.1.4   Sr^{2+} influence on local environment

The preference of the larger Sr^{2+} atom ($r = 1.18$ Å) to substitute in place of the Ca^{2+} ($r = 1.00$ Å) atom is reflected in the local environment of the substitution site. The Ca(4) site is weakly coordinated [64] to three oxygen atoms in a planar coordination, with bond lengths of 2.585 Å. The preference for Sr^{2+} to substitute at the Ca(4) site can be seen by the spacious coordination polyhedron of the site, that can easily accommodate
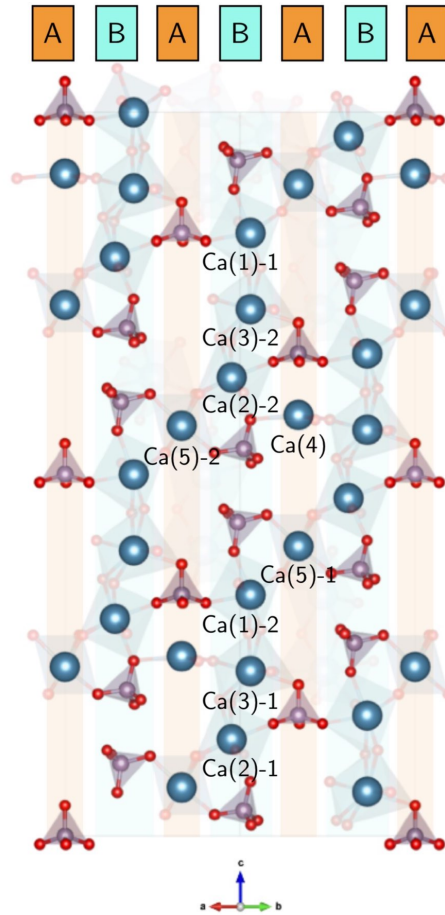
Figure 5.1 – The crystal structure of β-TCP showing the two types of repeating columns down the c-axis. The nine unique Ca sites from the low energy configuration are labelled.

the larger ion, as shown in Figure 5.3a. Conversely, the Ca(5) site is tightly six-fold coordinated with bond lengths of 2.267 Å and 2.261 Å (Figures 5.3b and 5.3c), and thus is unfavorable for substitution as this caged environment does not easily accommodate the large Sr^{2+} ion. The small energetic difference between the Ca(5)-1 and Ca(5)-2 site substitution by Sr ($\sim$0.2 eV) can be explained by a slight rearrangement of a phosphate tetrahedron, indicated in Figure 5.3b. The breaking of the caged environment has a stabilizing effect that lowers the energy of the Ca(5)-2 substituted site, as compared to the maintained cage of the Ca(5)-1 site (Figure 5.3c).

The Ca(1), Ca(2), and Ca(3) sites have more complicated coordination geometries, as shown in Figure 5.4. According to Ref. [28], the Ca(1) site is 7-fold coordinated with bond lengths that range from 2.340–2.621 Å; the Ca(2) and Ca(3) sites are 8-fold coordinated with bond lengths that range from 2.349–2.730 Å and 2.425–2.796 Å, respectively. The wide bond length variations of the relatively distorted coordination
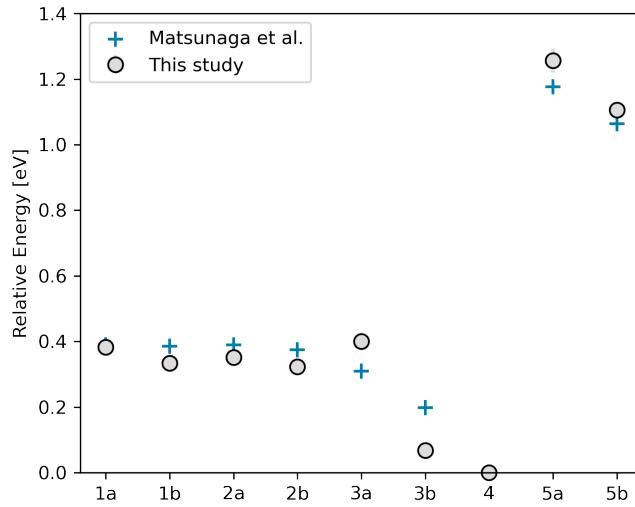
Figure 5.2 – MD equilibrated energies of single Sr^{2+} substitution at each unique Ca site. Energies are plotted relative to the Ca(4) site (the most stable substitution site).

polyhedra allow for strontium to substitute at these sites more readily than at the Ca(5) site. The differentiating feature between the Ca(1,2,3)-1 and Ca(1,2,3)-2 local environments is the P(1)-tetrahedron, circled in Figure 5.4. The P(1)-tetrahedron is oriented "up" with respect to the c-axis in the Ca(1,2,3)-1 sites, but appears rotated in the Ca(1,2,3)-2 sites. Similar to the Ca(5)-2 site, the rearrangement of the local geometry has a stabilizing effect that lowers the energy of the Ca(1,2,3)-2 sites. This stabilization is most pronounced for the Ca(3)-2 site. The P(1)-tetrahedron loses coordination with the Ca(3)-2 site, which significantly lowers the energy of the site relative to the Ca(3)-1 site.

5.1.5   Variation of cell parameters with degrees of Sr^{2+} substitution

To simulate the effects of varying degrees of Sr^{2+} substitution on the lattice and its unit cell parameters, the sites were "filled" in order of the determined energetic stabilities. The distribution of "filled" Ca(1), Ca(2), and Ca(3) sites at varying degrees of Sr^{2+} substitution is shown in Figure 5.5. The Ca(4) site is completely filled at low degrees of substitution ($\sim$6 at%), and strontium does not substitute at the Ca(5), even up to 80 at.%. The powder fitting refinements performed by Boanini et al. [64] report the highest occupancy factors of the Ca(4) and Ca(3) sites at low degrees of substitution, followed by the Ca(1) and Ca(2) sites as the overall substitution increases. This is therefore in agreement with the order in which Sr was substituted in our MD simulations.

The influence of strontium substitution on the unit cell constants is plotted in Figure 5.6, with simulation data points fitted with an ordinary least squares (OLS) regression. According to the fits, the a- and c-lattice parameters expand linearly with

(a)   (b)   (c)
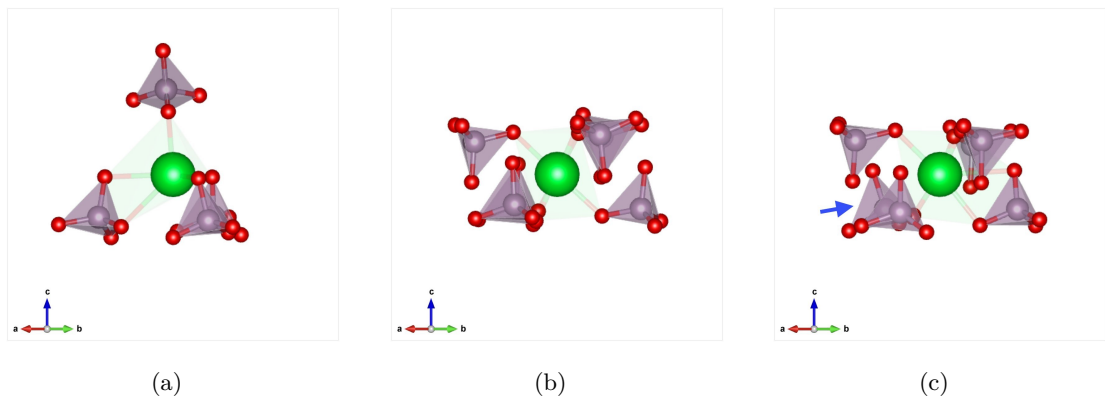
Figure 5.3 – MD equilibration snapshot around the local environment of Sr^{2+} substitution at the (a) Ca(4), (b) Ca(5)-1, and (c) Ca(5)-2 sites. The rearranged P(2)O$_4$ tetrahedron in (c) is indicated by the blue arrow.

(a)   (b)   (c)

(d)   (e)   (f)
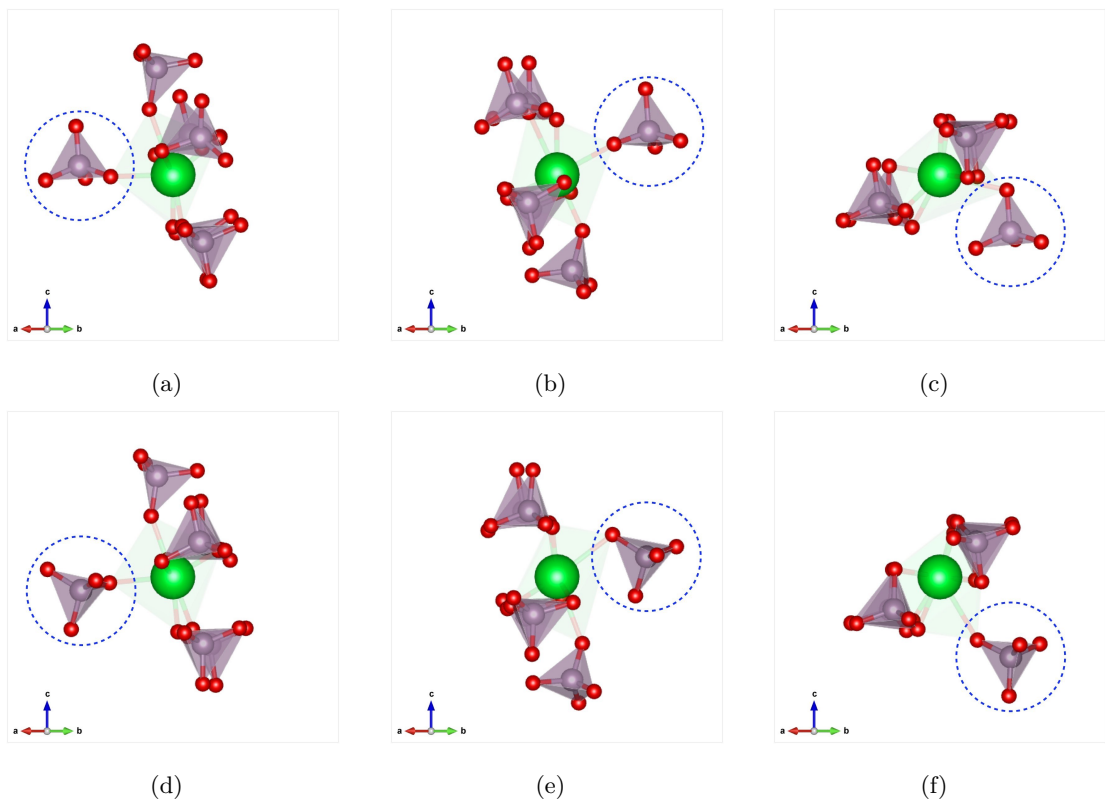
Figure 5.4 – MD equilibration snapshot around the local environment of Sr^{2+} substitution at the (a),(d) Ca(1)-1,2, (b),(e) Ca(2)-1,2, and (c),(f) Ca(3)-1,2 sites. The P(1)O$_4$ tetrahedra are indicated by the dashed blue circle.
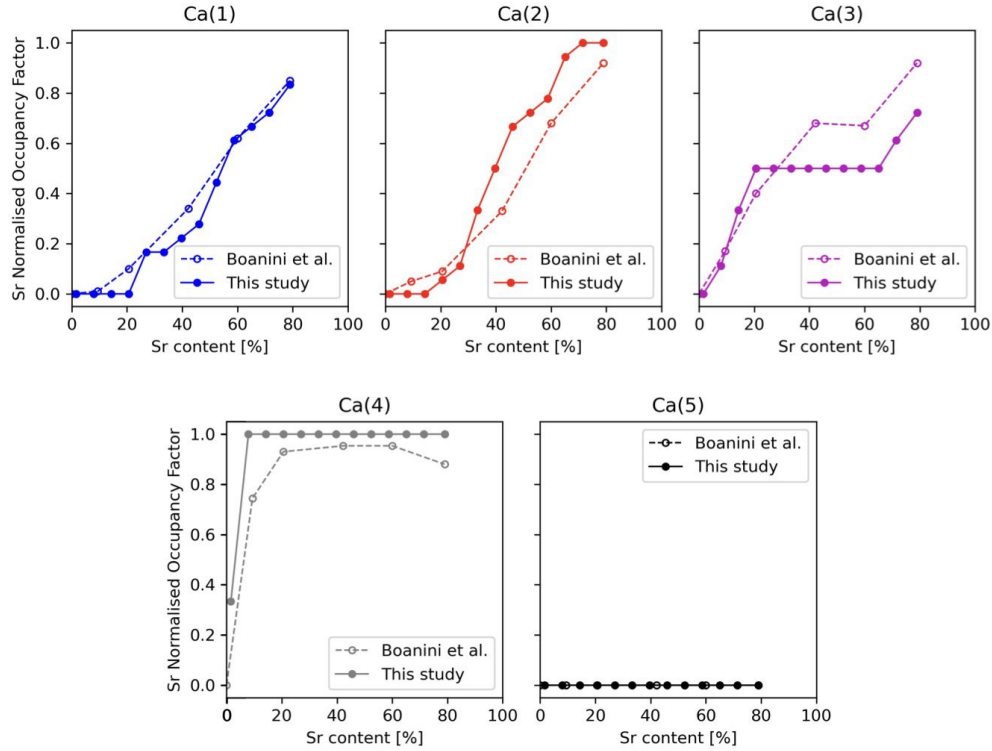
Figure 5.5 – Occupancy values of the Ca(1), Ca(2), Ca(3), Ca(4), and Ca(5) positions as a function of Sr content.

increasing strontium incorporation, following the equations given in Table 5.1. The calculated linear equations are similar to the trends reported by two experimental studies [64, 65]. This expansion of the unit cell parameters can be explained by the elongation of bond lengths at the Ca(1), Ca(2), and Ca(3) sites needed to accommodate the larger strontium ion, with the bonds elongating by 1.44–7.60% (Table 5.2). The ability of the calcium sites of β-TCP to host up to 80 at.% of strontium with linear enlargement of the lattice constants demonstrates that strontium incorporation does not provoke a remarkable rearrangement of the unit cell.

Table 5.1 – Determined linear equations of the lattice parameters as a function of strontium content.

	a-lattice	c-lattice
Bigi et al. [65]	$10.4340 + 0.373x$	$37.2110 + 2.50x$
Boanini et al. [64]	$10.4291 + 0.357x, R^2 = 0.985$	$37.2323 + 2.44x, R^2 = 0.980$
This study	$10.5084 + 0.545x, R^2 = 0.989$	$37.6949 + 3.46x, R^2 = 0.991$

Table 5.2 – Comparison between experimental and simulated Ca–O bond lengths, and Sr–O bond lengths.

		Exp. [28]	Ca–O(This study*)		Sr–O (This study)	
Ca(1)	O(6)	2.3277	2.3207	-0.3	2.4306	4.1
	O(5)	2.3907	2.3596	-1.3	2.4731	4.4
	O(8)	2.4196	2.4462	1.1	2.5859	4.9
	O(4, 4')	2.4518 2.4718	2.4462	0.4	2.6226	5.2
	O(9)	2.4648	2.4919	1.1	2.6409	5.0
	O(3)	2.5127	2.6082	3.8	2.7880	6.4
Ca(2)	O(9)	2.3578	2.4167	2.5	2.5762	5.9
	O(3)	2.3757	2.3709	-0.2	2.5237	5.3
	O(1)	2.4067	2.3369	-2.9	2.5503	4.9
	O(7,7')	2.4228 2.4247	2.4446	0.9	2.5981	5.4
	O(2)	2.4197	2.3616	-2.4	2.6114	5.3
	O(5)	2.7027	2.7405	1.4	2.7776	2.8
	O(6)	2.7448	2.7283	-0.6	2.7883	2.4
Ca(3)	O(3)	2.3547	2.3994	1.9	2.5498	5.2
	O(5)	2.3936	2.4463	2.2	2.5636	4.4
	O(6)	2.5477	2.5069	-1.6	2.6548	4.2
	O(8,8')	2.5687 2.6227	2.5790	0.4	2.7286	4.3
	O(10)	2.5734	2.4396	-5.2	2.6747	7.6
	O(2)	2.5997	2.4307	-6.5	2.6337	3.1
	O(1)	2.6896	-	-	2.8422	1.6
Ca(4)	O(1, 1', 1")	2.5316	2.6607	5.1	2.5637	-1.0
Ca(5)	O(4, 4', 4")	2.2119	2.2561	2.0	2.4011	6.0
	O(7, 7', 7")	2.3129	2.2528	-2.6	2.3863	5.6

Note: Values are from the LEC column of Table 4.2 in Section 4.1.
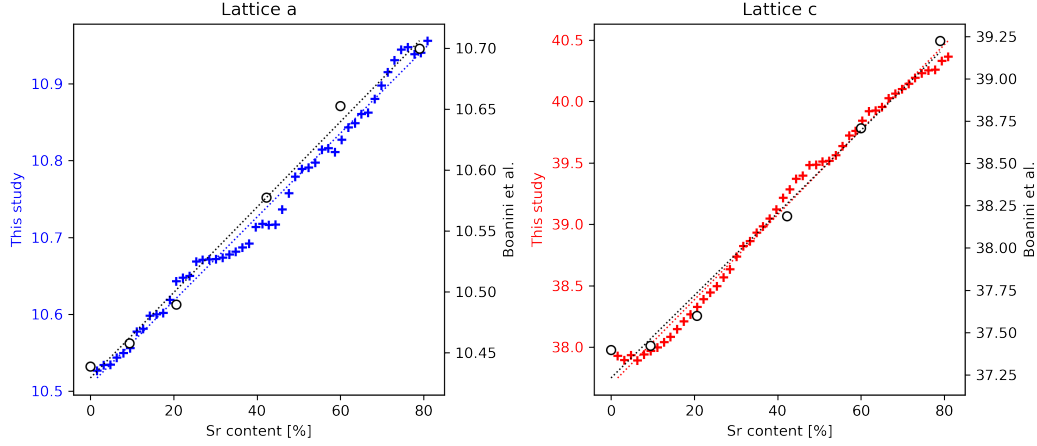
Figure 5.6 – The MD equilibrated a- and c-lattice parameters plotted as a function of strontium content. The dotted lines show the respective OLS fits to the simulation data points.

5.1.6   Reaction enthalpies of Sr^{2+} substitution

Having investigated the structural features of Sr-doped β-TCP, the next quantity of interest is the reaction enthalpy. This is calculated by considering the synthesis method of Bigi et al. [65], who prepared β-TCP with varying degrees of Sr^{2+} substitution by heat treatment of appropriate mixtures of β-TCP and α-Sr$_3$(PO$_4$)$_2$ at 1000℃ for 15 h. The stoichiometric reaction to produce Sr-doped β-TCP is shown with the following equation:

$$(1-x) \cdot \mathrm{Ca_3(PO_4)_2} + x \cdot \mathrm{Sr_3(PO_4)_2} \longrightarrow \mathrm{Ca_{(1-x)}Sr_x(PO_4)_2} \tag{5.2}$$
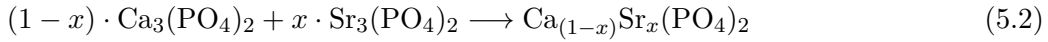
Therefore, the stability of strontium in β-TCP is evaluated from the reaction enthalpy, given by the following equation:

$$\Delta H_{\mathrm{rxn}} = H_{\mathrm{Ca_{(1-x)}Sr_x(PO_4)_2}} - \left((1-x) \cdot H_{\mathrm{Ca_3(PO_4)_2}} + x \cdot H_{\mathrm{Sr_x(PO_4)_2}} \right) \tag{5.3}$$

where $H_{\mathrm{Ca_3(PO_4)_2}}$ is the enthalpy of pure β-TCP evaluated using the structure reported by Yashima et al [28]. The enthalpy of Sr$_3$(PO$_4$)$_2$, $H_{\mathrm{Sr_x(PO_4)_2}}$, was evaluated using the structure reported by Zachariesen et al. [66]. $H_{\mathrm{Ca_{(1-x)}Sr_x(PO_4)_2}}$ is the calculated enthalpy with a fraction x of Ca sites substituted by Sr. Figure 5.7 shows the calculated reaction enthalpies as a function of Sr content by Equation 5.3.

     The calculated reaction enthalpies were fitted with an OLS. As shown in Figure 5.7, they are discretized into three parts that each follows its own linear trend, whose expressions are given in Equation 5.4. The values first descend according to Equation
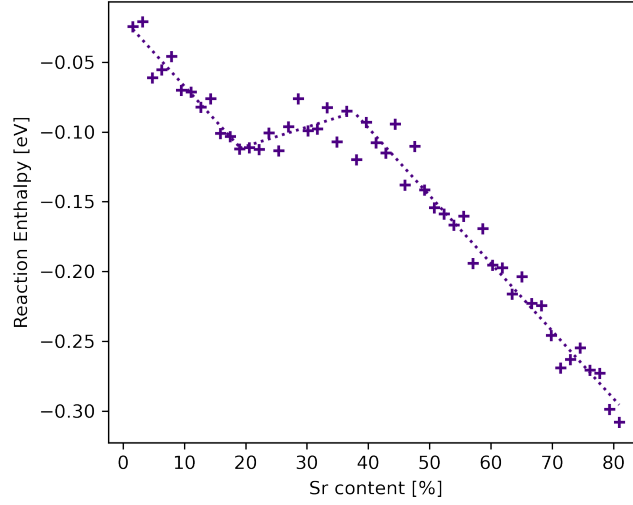
Figure 5.7 – Calculated reaction enthalpies as a function of strontium content. The dotted lines show the OLS fits to the stimulation data points.

5.4a up to a strontium content of 20.6 at.%, then at 38.1 at.% is continued with a similar slope up to the maximum substitution of 80.0 at.%, as described by Equation 5.4c. The trend is broken between 20.6–38.1 at.%, where the values slightly increase, as described by Equation 5.4b. Our current analysis has no interpretation for this region. All reported values are negative even up to significant concentrations of strontium, indicating that strontium is stable when incorporated in β-TCP with respect to phase separation into β-TCP and strontium phosphate. Further calculations are planned that will leverage experimental thermodynamic databases to obtain an experimental comparison to these simulated reaction enthalpies.

$$y = \begin{cases} -0.4840x - 0.0118, \ (R^2 = 0.901) & \text{if } x < 0.206 \ , & (5.4a) \\ 0.1374x - 0.1378, \ (R^2 = 0.382) & \text{if } 0.206 \leq x \leq 0.381 \ , & (5.4b) \\ -0.4844x + 0.0967, \ (R^2 = 0.962) & \text{if } x > 0.381 \ . & (5.4c) \end{cases}$$

5.1.7   Conclusions

In this section, atomistic simulations were performed to investigate strontium substitution in the β-TCP lattice. Strontium was shown to substitute most favorably at the Ca(4) site, with a small energetic barrier to substitute at the Ca(3)-2 site. Substitution at the Ca(5) site proved to be highly unfavorable. The results showed excellent agreement to previous first-principles calculations and experimental results.

The site preference is strongly correlated to the local environment of the site. The spacious environment of the Ca(4) easily accommodates the larger Sr^{2+} ion, while the unfavorable substitution at the Ca(5) site can be related to its caged environment. Interestingly, the slight rearrangements of the P(1) tetrahedron coordinated to the Ca(1,2,3)-2 and a P(2) tetrahedron coordinated to the Ca(5)-2 site have a stabilizing effect, making them more energetically favorable than their non-rearranged counterparts. This rearrangement has not been previously mentioned.

With increasing incorporation of strontium in the β-TCP crystal lattice, the *a*- and *c*-lattice parameters expand following a linear trend similar to that seen in experimental results. The expansion of the unit cell lattice parameters is due to the elongation of bond lengths needed to incorporate the larger ion. Reaction enthalpies for varying degrees of strontium substitution were calculated.

The results presented in this section demonstrate the validity of the force field used, as based on the Demichelis et al. force field for β-TCP with our addition of the strontium parameters in a Buckingham format derived from the work of Rabone and de Leeuw. In the next sections, this force field is used to simulate the interaction of Sr dopants with surfaces and grain boundaries, as of potential significance for the use of Sr-doped β-TCP as a resorbable bone substitute.

5.2   Workflow for simulating Sr-doped interfaces

5.2.1   Introduction

This section aims to describe the strategy used to create the surface and grain boundaries of Sr-doped, β-TCP using Monte Carlo simulations. The approach taken presents three nodes as follows: (1) slab generation, (2) creation of interface, (3) selection of the occupied Ca(4) sites and incorporation of dopants.

5.2.2   Approach

The non-doped interface structures were constructed using METADISE [20]. As the three-body bond angle intramolecular definition reported by Demichellis et al. is currently incompatible with METADISE, another force field must be used. The choice was made to use the potential set reported by Jay et al. [34] for two reasons: (1) the three-body angle is compatible with METADISE, and (2) the included core-shell model of the O-atom is more appropriate for creating dipole-free slab structures.

In order to create the slabs, the crystal structure must be defined. A first attempt was made using the β-TCP unit cell reported by Yashima et al. [28] with the LEC arrangement of the Ca(4) sites (as discussed in Section 4.1). However, the resulting slab structure was unreasonably large for performing atomistic simulations. Therefore, it was decided to use a 'reduced' β-TCP crystal structure, that cuts the unit cell in half down the c-axis. This 'reduced' unit cell contains 138 atoms, and has the following dimensions: $a = b = 10.445$ Å, $c = 18.5$ Å, $\alpha = \beta = 90°$, $\gamma = 120°$. At this point, in order to preserve the six Ca(4) sites of the crystal structure, all the Ca(4) sites in the 'reduced' unit cell are populated with a $q = +1.0$ charge.

The interface structures were created in METADISE by cleaving the 'reduced' crystallographic unit cell along two chosen planes: $(1\,\bar{2}\,0)$ and $(1\,0\,0)$. These planes are considered because they were experimentally-identified as crystal surface planes by Tao et al. [67]. Cleaving along a given crystallographic plane generates multiple terminations. Only the lowest energy termination was considered for creating the surface and grain boundary structures, which are shown in Figure 5.8. 3D-periodic boundary conditions were used such that two surfaces or two grain boundaries (A and B) are respectively contained in each simulation box.

5.2.3   Sr-dopant incorporation

Before dopants can be introduced into the crystal structure, the occupancy of the Ca(4) site of the β-TCP crystal structure needs to be addressed. A reduced β-TCP unit cell was used in order to create the interface structures, which preserved the six Ca(4) sites by

(1 -2 0)

(1 0 0)

(1 -2 0)

(1 0 0)

x: 18.65 Å
y: 17.81 Å
z: 82.50 Å

x: 20.57 Å
y: 18.65 Å
z: 71.50 Å

x: 18.65 Å
y: 17.81 Å
z: 165.45 Å

x: 20.57 Å
y: 18.65 Å
z: 164.33 Å

(a)

(b)
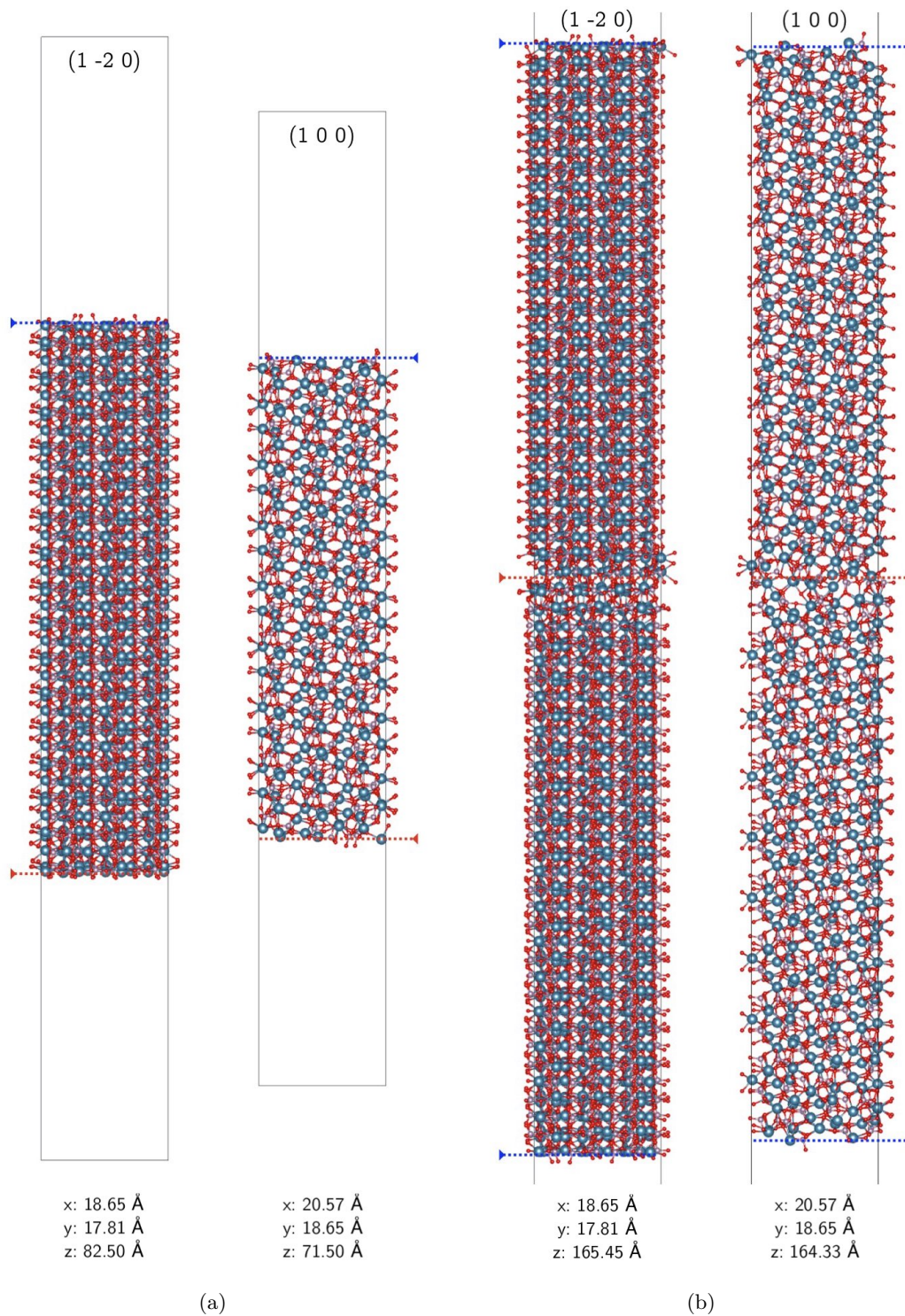
Figure 5.8 – Un-doped β-TCP structures: (a) surfaces and (b) grain boundaries. Interface A and Interface B are identified by the blue and red arrow, respectively.

occupying all the Ca(4) sites with a charge, $q = +1.0$. As seen in Chapter 4, the charge neutrality of the β-TCP simulation box is preserved by occupying 50% of the Ca(4) sites. The occupied Ca(4) sites must be selected with care. An initial attempt at selecting the Ca(4) sites in the surface structures considered all the Ca(4) sites for random occupancy selection to give a total with 50% Ca(4)-site occupancy. However, considering all the Ca(4) sites in this way can lead to a non-homogeneous charge distribution of $q = +2.0$ down the long axis of the interface structure, resulting in an introduced dipole moment. In order to prevent this occurring, instead of a global consideration of the Ca(4) sites, the Ca(4) sites are grouped in layers down the interface structure. Within each of these layers 50% of the Ca(4) sites are randomly selected to be occupied, therefore creating a zero total dipole perpendicular to the surface.

At this point, dopants can now be introduced into the interface structures. The incorporation of strontium is performed with an in-house Python script, see Appendix B.2. This code considers all the calcium sites in the interface structure as available for dopant substitution. All the calcium sites, Ca(1-5), are then randomly selected for incorporating the desired amount of Sr^{2+} by substitution in place of Ca^{2+}.

5.2.4 Evaluating the implications of randomly selecting the Ca(4) site occupancy

The Ca(4) site acts as a free variable that could possibly influence the distribution of strontium within the interface structures. For example, the (1 0 0) surface structure contains 48 Ca(4) sites, which are grouped in 24 layers along the z-axis perpendicular to the surface (Figure 5.9a). With two Ca(4) sites in each layer, there are $(2^{24} =) \, 16,777,216$ possible Ca(4) site arrangements corresponding to the defined condition for selecting the occupied Ca(4) site. The number of possible occupied Ca(4) site arrangements is staggeringly larger with the grain boundary structures (Figure 5.9b), which now have 54 layers resulting in $(2^{54} =) \, 1.80 \times 10^{16}$ possible arrangements. Sampling this entire phase space is an impractical feat; instead, practically, we can only sample a handful of occupancy arrangements. Therefore, in order to validate that such a small sampling can give adequately representative results, we must evaluate the effect of randomly selecting the Ca(4) site occupancies on various properties, such as the energetics of the structure and the distribution of strontium within the structure. To do this, a series of (1 0 0) surface and grain boundary structures with different variations of randomly selected Ca(4) site occupancies are investigated, and the incorporated dopant content is varied.

Monte Carlo simulations were performed using the DL_MONTE [22, 23] computational suite to simulate the distributions of strontium doped into β-TCP interface structures having different arrangements of randomly-selected Ca(4) site occupancies. The combined force field, validated in Section 5.1, was the defined force field for these simulations. In these simulations, the phosphate group is considered to be a rigid body.

(a)

(b)
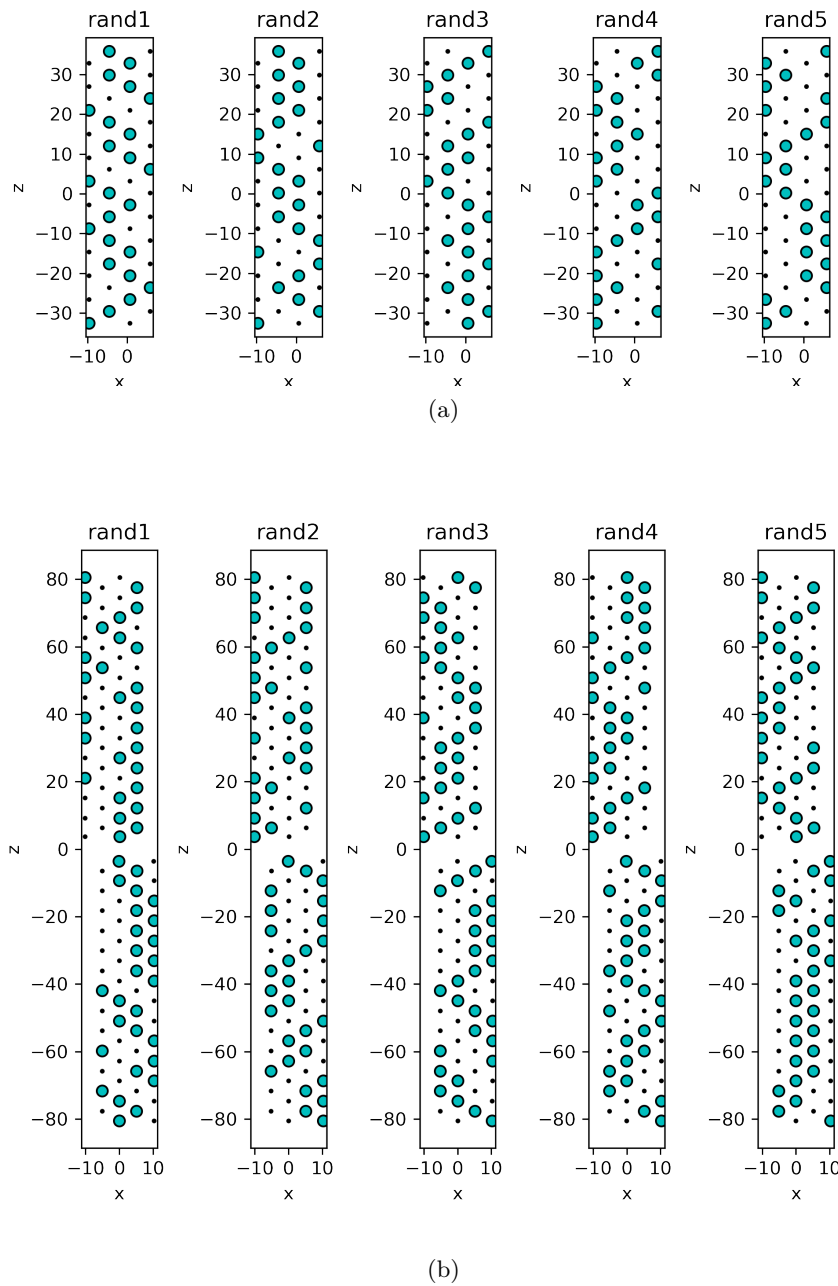
Figure 5.9 – Schematic representation of the Ca(4) sites in (a) (1 0 0) surface structures, and (b) (1 0 0) grain boundary structure, projected down the y-axis of the simulation box. $Ca(4)_{occ}$ (blue scatter), $Ca(4)_{vac}$ (black pixel)

The simulations were run at 1400 K in order to closely approximate the sintering temperature of the ceramics at 1100℃ (1373.15 K) [19]. The Monte Carlo moves implemented within a cycle are: (1) the atomic displacement of Ca^{2+} and Sr^{2+} ions, (2) the molecular displacement of the phosphate group, (3) the molecular rotation of the phosphate group, (4) the pairwise swap in coordinates of the Ca^{2+} and Sr^{2+} ions, and (5) the anisotropic scaling moves of the simulation box. The surface and grain boundary simulations were run for 2.2×10^7 and 5×10^7 MC steps, respectively, both with 78 data production cycles. The protocol and potential fields for running these simulations can be found in Appendix A.3.

As we are interested in determining the distribution of strontium at the interfaces, the interface depths must be defined. The strontium depths perpendicular to the interface are collected from each structure in the data production cycle. From this distribution, the Kernel Density Estimate (KDE) curve is determined in order to evaluate the interface depth. Bulk-like behavior is observed between $-0.2 < z < 0.2$ of the fractional z-direction of the surface simulation box. The grain boundary simulation boxes contain two grain boundaries; one is located at the middle of the box, and the other is located at the bounds of the simulation box. Therefore, bulk-like behavior is observed between $0.15 < |z| < 0.35$ of the fractional z-direction of the simulation box. The mean strontium density is evaluated within this region in order to define the bulk-like behavior, highlighted by the orange band, in Figure 5.10. Where the KDE curve deviates from evaluated bulk-like behavior is where the interface depths are defined. This is evaluated as the extremum intersections of the KDE curve with the bulk density ($\mu + \sigma$).

5.2.5   Energetic implications

The energetic statistics for the (1 0 0) surface structures with varying strontium content are summarized in Tables 5.3 and 5.4. The interquartile ranges reported show that from the (1 0 0) surface structures ($n = 21$), the energies of the structures are likely to range between 0.20–0.24 eV/u.c. For the grain boundary systems, fewer structures need to be sampled to achieve the same range as the surface simulations. The interquartile ranges reported show that, from the (1 0 0) grain boundary structures ($n = 5$), the energies of the structures are likely to range between 0.04–0.28 eV/u.c. The median of the sampled configurations is used for fitting the total energy of the system as a function of strontium content. The total energy of the systems increases linearly with increasing dopant concentration (Figure 5.11), by the following equations for the surface (Equation 5.5) and grain boundary (Equation 5.6) simulations:

$$y = 1.3142x - 1233.3663, R^2 = 0.998 \tag{5.5}$$
$$y = 1.3747x - 1312.7335, R^2 = 1.000 \tag{5.6}$$
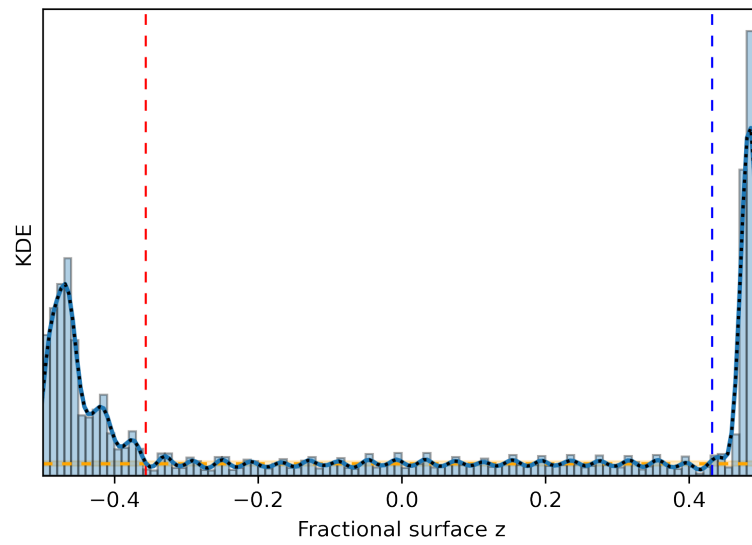
(a)
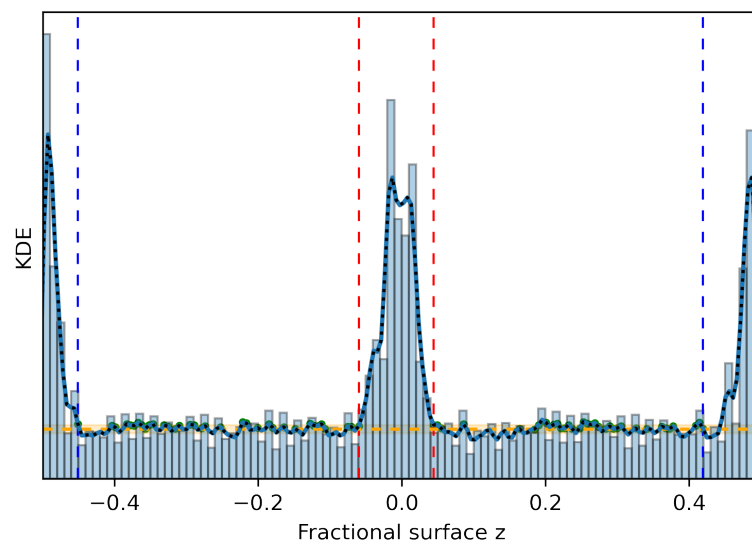
(b)

Figure 5.10 – (a) Surface and (b) grain boundary depth determination from the KDE curves (dotted, black line) for the (1 0 0) orientation. Bulk-level is indicated with the orange line. The interface regions, noted by the dashed, colored lines, indicate where the KDE curve deviates from bulk-like behavior.

The good fit of the lines, as indicated by the R^2 values, is actually a pretty powerful revelation, because this means that, from an energetic perspective, any Ca(4) site occupancy arrangement can fit well to the trend.

Table 5.3 – Surface ($n = 21$) energies [eV/u.c.] for different Sr contents showing, the median, upper (Q3) and lower (Q1) quartiles, and the interquartile range (IQR = Q3 - Q1).

Sr content [%]	Median	Q1	Q3	IQR
0.1984	-1233.004	-1233.148	-1232.920	0.23
0.9921	-1232.060	-1232.158	-1231.913	0.24
1.7857	-1231.098	-1231.172	-1230.974	0.20
2.9762	-1229.579	-1229.708	-1229.493	0.21
4.9603	-1226.749	-1226.929	-1226.625	0.30

Table 5.4 – Grain boundary ($n = 5$) energies [eV/u.c.], for different Sr contents showing, the median, upper (Q3) and lower (Q1) quartiles, and the interquartile range (IQR = Q3 - Q1).

Sr content [%]	Median	Q1	Q3	IQR
0.1764	-1312.437	-1312.584	-1312.398	0.19
0.9700	-1311.417	-1311.529	-1311.327	0.20
1.7637	-1310.355	-1310.391	-1310.353	0.04
2.9101	-1308.753	-1309.024	-1308.739	0.28
4.9383	-1305.915	-1306.017	-1305.778	0.24

5.2.6 Strontium distribution to interfaces

As we have observed the influence of the Ca(4) site occupancy arrangements has little effect on the energetics of the interface structures, we now see if the Ca(4) site occupancy arrangements influence the distribution of dopants within the structures. The simulated ratios of strontium concentration in the interface-to-bulk for varying strontium contents are summarized in Table 5.5 and presented as a box plot in Figure 5.12. First considering the surface structures, the arrangement of the Ca(4) site occupancy is seen to significantly influence the distribution of strontium between the surface and bulk at low dopant concentrations. This is most prominently seen at 0.20% Sr, which displays the largest spread with an IQR = 58. While the IQR at 0.99% and 1.79% Sr is not as wide compared to that for the 0.20% Sr, the range in distribution remains non-negligible. Therefore, at low dopant concentrations, multiple configurations with random Ca(4) site arrangements would need to be sampled in order to accurately describe the distribution of dopants at the surfaces. The higher concentrations (2.98%, 4.96%) show significantly smaller
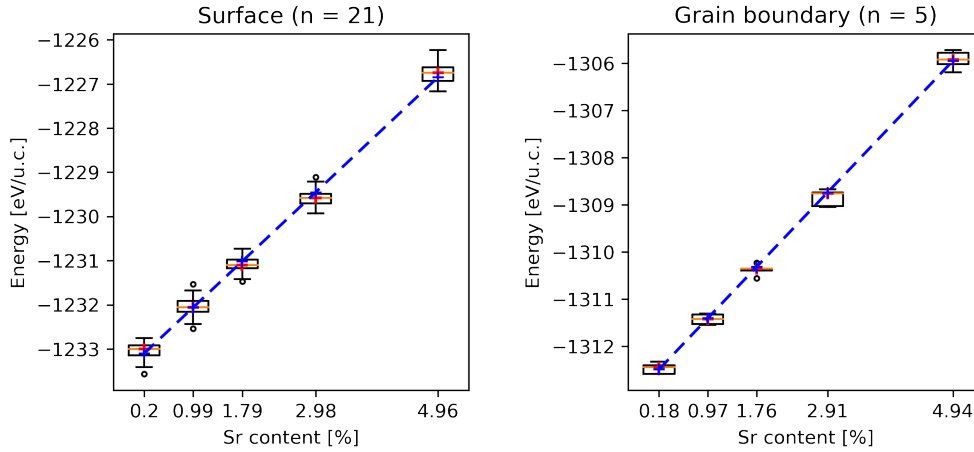
Figure 5.11 – Box plots of surface ($n = 21$) and grain boundary ($n = 5$) energies plotted as a function of strontium content. Distributions are drawn with Spear style whiskers.

IQR spreads. At these concentrations, multiple configurations would essentially give similar distributions. Therefore, it can be judged that the influence of the Ca(4) site occupancy arrangement is negligible at strontium concentrations above $\sim 2\%$ and the resulting distribution from a single configuration would be a representative result.

Interestingly, in contrast, Figure 5.12 and Table 5.6 indicate that the arrangement of the Ca(4) site occupancy has little influence on the distribution of strontium to the grain boundaries, even at low dopant concentrations. All determined IQR values for the varying dopant concentrations in the grain boundary structures lie between 0.22–0.70. This is a vitally important result that implies a single configuration would give a representative result of dopant behavior to the grain boundary, without having to sample even a small fraction of the 1.80×10^{16} possible configurations.

5.2.7   Conclusions

This section presented the strategy for creating the β-TCP interface structures. Due to the large nature of the β-TCP unit cell, a 'reduced' β-TCP unit cell was used to create the interface structures, in order to create reasonably sized simulation boxes for Monte Carlo simulations. The use of the 'reduced' unit cell for creating the interface structures requires a 50% selection of Ca(4) sites to be occupied. The determined condition for selecting the occupied Ca(4) sites first groups the Ca(4) sites in layers perpendicular to the interface. Within each of these layers, 50% of the Ca(4) sites are selected to be occupied, in order to ensure a zero net dipole moment within the interface structures.

With this methodology for creating the interface structures, the implications of assigning the Ca(4) site occupancies were assessed using the (1 0 0) interface structures as a pilot study. The energetics and dopant distributions of a series of surfaces ($n = 21$)
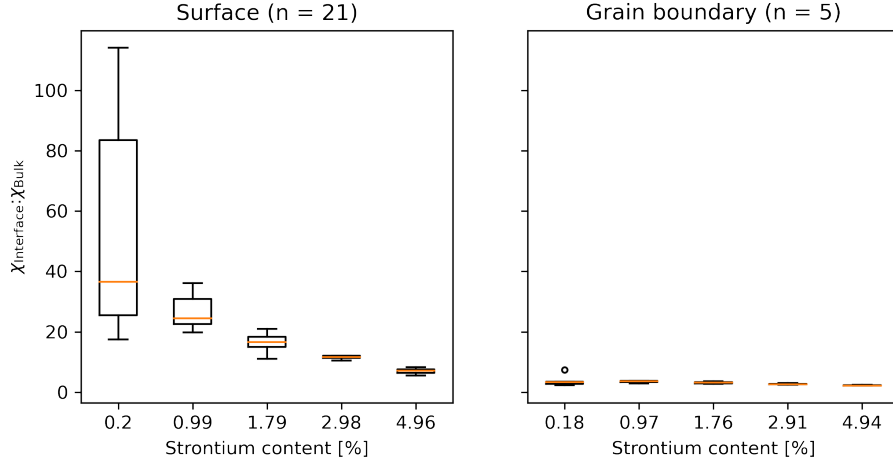
Figure 5.12 – Box plots of the strontium surface-to-bulk ($n = 21$) and grain boundary-to-bulk ($n = 5$) concentrations plotted as a function of strontium content. Distributions are drawn with Spear style whiskers.

Table 5.5 – Strontium segregation ratio [$\chi_{\text{surface}} : \chi_{\text{bulk}}$] for different Sr content, with statistical parameters: median, Q1, Q3, and IQR values of the (1 0 0) β-TCP interfaces

Sr content [%]	Median	Q1	Q3	IQR
0.1984	36.549	25.499	83.467	58.0
0.9921	24.528	22.518	30.868	8.3
1.7857	16.508	14.999	18.329	3.3
2.9762	11.593	11.276	12.044	0.8
4.9603	7.037	6.342	7.494	1.2

Table 5.6 – Strontium segregation ratio [$\chi_{\text{GB}} : \chi_{\text{bulk}}$] for different Sr content, with statistical parameters: median, Q1, Q3, and IQR values of the (1 0 0) β-TCP interfaces

Sr content [%]	Median	Q1	Q3	IQR
0.1764	3.354	2.783	3.480	0.70
0.9700	3.537	3.290	3.686	0.40
1.7637	3.174	2.881	3.369	0.49
2.9101	2.567	2.536	2.775	0.24
4.9383	2.190	2.109	2.333	0.22

and grain boundaries ($n = 5$) with varying strontium concentrations were evaluated from Monte Carlo simulations. The results reveal the following:

- The energies of the structures linearly increases with increasing dopant concentration. This linear trend was evaluated from the median values reported at each strontium concentration. This implies that the variation in energetics due to different Ca(4) site occupancy arrangements is negligible.

- Although the energetics suggest that the structures are equivalent, the influence of the Ca(4) occupancy site on the resulting distribution of strontium dopants gives us significantly different results. In particular, one would need to interpret the results of low dopant concentrations in β-TCP surface structures with caution because the resulting values could lie anywhere within a large IQR, which here was found to be IQR $= 58$.

- This is not the case for grain boundary structures. Even at low dopant concentrations the simulations from five different arrangements of Ca(4) site occupancy, giving strontium distributions consistent to an IQR < 0.7, suggest that a single, randomly-defined configuration would essentially give a representative result.

These results will be used in the sampling protocol of the following Section 5.3, where the Sr segregation to surfaces and grain boundaries is looked at in more detail.

5.3   Atomistic simulations of Sr-doped β-TCP interfaces

5.3.1   Introduction

This section builds off the framework presented in Section 5.2 to investigate the behavior of strontium to β-TCP interfaces, through the use of appropriate Monte Carlo simulations. Of the identified β-TCP surface planes reported by Tao et al. [67], here we will focus on the (1 $\bar{2}$ 0) and (1 0 0) variants and present a comparative analysis of the β-TCP interfaces in supercells that have been doped with various amounts of strontium. This work is effectively a pilot study, with the aim that the pipeline used for these two surfaces/grain boundaries can be straightforwardly applied to study other surface/grain boundary variants in the future. After presenting the simulation methodology and results on Sr distribution at interfaces, this section then discusses interface energies and enthalpies of segregation per dopant before some brief concluding remarks.

5.3.2   Methodology

Interface structures. The surface and grain boundary structures were created using the 'reduced' β-TCP unit cell previously described in Section 5.2. The interfaces were modeled with a slab method using the METADISE code [20], in which a finite number of crystal layers are used to generate the interface structures. Surface structures are created by introducing a vacuum gap perpendicular to the surface. A vacuum gap of 35 Å was used to minimize the interaction between surface images. The (1 $\bar{2}$ 0) and (1 0 0) surface structures both contain 8 unit cells (u.c.). Near-coincidence grain boundary structures were created by mirroring an image of the surface across the surface plane. A 2D-scan of the interface was then performed to determine the ideal displacement vector for arranging the two bodies, followed by an energy minimization protocol. The resulting (1 $\bar{2}$ 0) and (1 0 0) grain boundaries structures contain 16 u.c. and 18 u.c., respectively. The 50% partial occupancy of the Ca(4) site for all structures is addressed by grouping the Ca(4) sites in layers down the axis perpendicular to the interface plane. Within each layer, 50% of the Ca(4) sites are randomly selected to be occupied. The desired dopant concentration is then incorporated by substituting Sr^{2+} in place of Ca^{2+} at randomly selected Ca(1,2,3,4,5) sites. In this study, several Sr-dopant concentrations were considered for each interface structure, $C_i[\%] = \{1.00,\ 1.71,\ 2.92,\ 5.00,\ 10.00,\ 20.00,\ 40.00\}$.

Calculation details. Monte Carlo simulations were performed using DL_MONTE [22, 23]. The combined force field, presented in Section 5.1, was applied for these simulations. In these simulations, the phosphate group is considered to be a rigid body. As in previous section, the simulations were run at 1400 K. The Monte Carlo moves implemented within a cycle are: (1) the atomic displacement of Ca^{2+} and Sr^{2+} ions, (2) the molecular displacement of the phosphate group, (3) the molecular rotation of the phosphate group, (4) the pairwise swap in coordinates of the Ca^{2+} and Sr^{2+} ions, and

(5) the anisotropic scaling moves of the simulation box. The surface simulations were run for an equilibration period of 5.0×10^6 MC steps, followed by a data production run of 2.2×10^7 MC steps. The grain boundary simulations were run for an equilibration period of 2.5×10^7 MC steps, followed by a data production run of 5.0×10^8 MC steps. Both simulation protocols collect 1000 structures. Similar protocol and potential fields for running these simulations can be found in Appendix A.3.

5.3.3   Strontium distribution to the interfaces

We begin by considering the results for dopant behavior relative to free surfaces. The distribution of the Sr^{2+} ions along the z-axis perpendicular to the surface planes, and averaged over the $n = 1000$ structures of the MC trajectory, are shown in Figure 5.13. The two surface regions are placed at the ends of the z-axes, with a bulk-like region in the middle. These distributions clearly show an accumulation of Sr^{2+} ions to the surface regions, with surface depths (as determined using the method described in Section 5.2) that range between 4.60–9.33 Å and 3.76–11.94 Å for the $(1\ \bar{2}\ 0)$ and $(1\ 0\ 0)$ surfaces, respectively. This accumulation becomes less pronounced with increasing dopant concentrations, as the Sr^{2+} level in the bulk region increases. Also clearly shown in the distributions, is that the bulk region always hosts Sr^{2+} ions, even at low dopant concentrations. This is not unexpected, considering that strontium can substitute up to 80 at.% in the β-TCP crystal lattice [64, 65], as discussed in Section 5.1.

The observations made on the histogram distributions can be quantified by comparing the concentration of Sr^{2+} ions in the surface region (χ_{surf}) to the concentration of ions in the bulk region (χ_{bulk}), as shown in Figure 5.14a. Further details on the approach used for the determination of χ_{surf}:χ_{bulk} ratio can be found in Appendix B.1. The $(1\ 0\ 0)$ surface generally has a higher concentration of ions in its surface regions than the $(1\ \bar{2}\ 0)$ surface. Also, both trend lines show an exponential decay in surface-to-bulk concentration ratios with increasing Sr-content, converging to similar values at the higher dopant concentrations (10–40%). Equally, as Sr-content increases, it appears that the trend lines tend asymptotically towards a ratio of χ_{surf}:$\chi_{bulk} = 1$, which represents a homogeneous distribution of ions throughout the structure.

We now turn to the simulation of strontium dopant behavior in structures containing grain boundaries. Figure 5.15 plots the distribution of strontium atoms along z-axes perpendicular to the grain boundary planes for varying strontium contents. Similar to the surface structures, these distributions also clearly show that Sr^{2+} ions are always hosted in the bulk region as well as around the grain boundaries. An accumulation of Sr^{2+} ions is clearly seen in the $(1\ 0\ 0)$ grain boundary regions, within distances that range between 5.19–21.74 Å. Although not so readily apparent, Sr^{2+} ions accumulate in the $(1\ \bar{2}\ 0)$ grain boundary regions within distances that range between 4.43–19.63 Å.

(a)   (b)
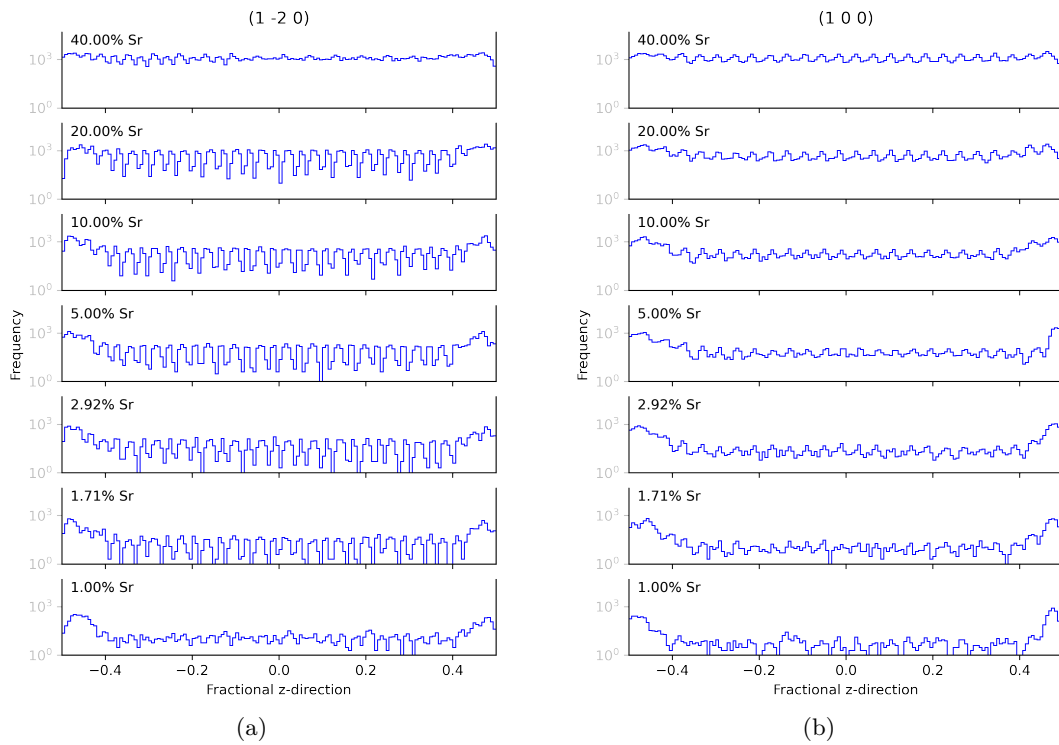
Figure 5.13 – Histogram distributions of the Sr^{2+} fractional positions along the z-axis perpendicular to the $(1\ \overline{2}\ 0)$ and $(1\ 0\ 0)$ surfaces, for varying Sr-content. In each plot, the two surfaces are at fractional $z = \{+0.5, -0.5\}$. The y-axis is plotted on a log-scale.

(a)   (b)
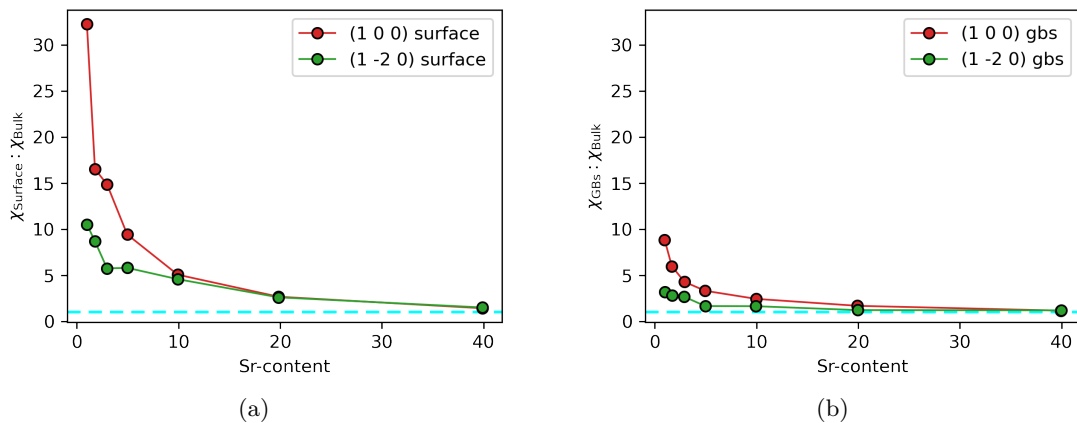
Figure 5.14 – The determined χ_{interf}:χ_{bulk} values plotted as a function of Sr-content [at.%] for the (a) surfaces and (b) grain boundaries.
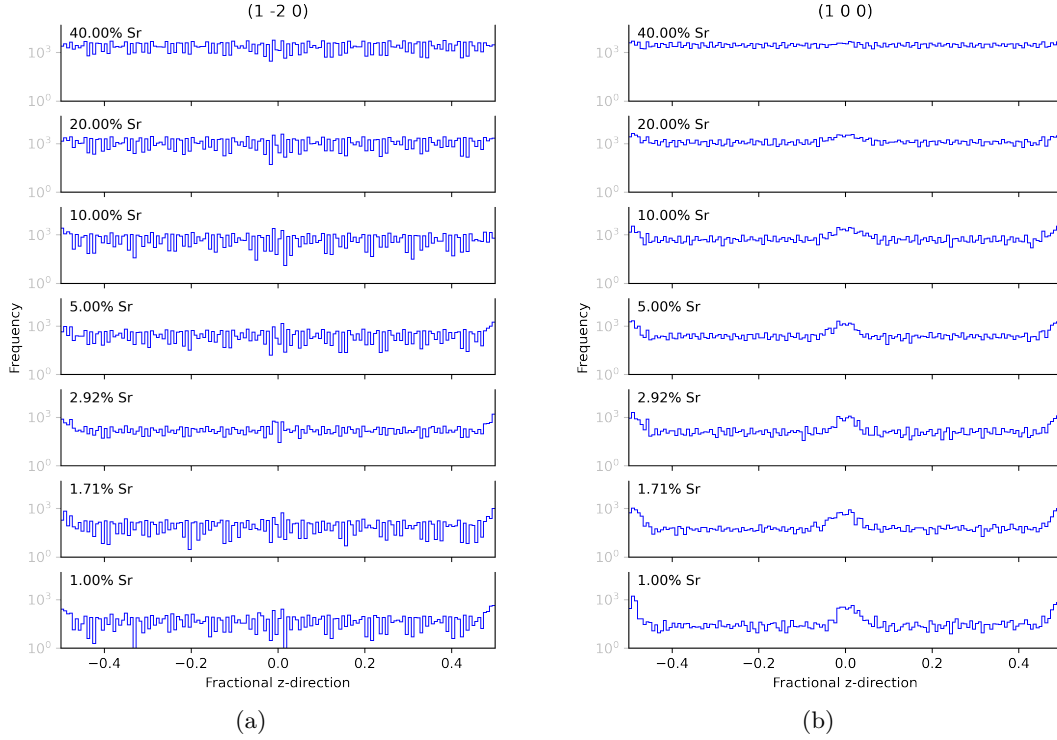
Figure 5.15 – Histogram distributions of the Sr^{2+} fractional positions along z-axis perpendicular to the $(1\,\overline{2}\,0)$ and $(1\,0\,0)$ grain boundaries, for varying Sr-content. In each plot, the two grain boundares are at fractional $z = \{0, \pm 0.5\}$. The y-axis is plotted on a log-scale.

In order to better visualize the partitioning of Sr^{2+} ions between the grain boundary regions and the bulk, in Figure 5.14b the concentration of ions in the grain boundary region (χ_{GB}) is compared to the concentration of ions in the bulk region (χ_{bulk}), where the profiles can also be compared to those from the surface structures in Figure 5.14a. Similar to the surface trends, the $(1\,0\,0)$ grain boundary generally has a higher concentration of Sr^{2+} ions in the grain boundary regions than the $(1\,\overline{2}\,0)$ grain boundary. Both trend lines show an exponential decay in χ_{GB}:χ_{bulk} values as a function of increasing dopant, with ratios that tend towards the ratio of χ_{GB}:$\chi_{bulk} = 1$ at the higher concentrations.

5.3.4   Interface Energies

Having gained these preliminary insights into the relative segregation of dopant Sr^{2+} ions to free surfaces and grain boundaries, the next calculated quantity of interest is the interfacial energy. The interfacial energy (γ) for the structures can be calculated according to the following equation:

$$\gamma = \frac{E_{\text{interf}} - mE_{\text{bulk}}}{2A} \tag{5.7}$$

76

where E_{interf} is the energy of an interface systems containing m unit cells with a cross-sectional area (A), and E_{bulk} is the energy of the corresponding bulk unit cell. Applying this, the surface energies of the pure $(1\,\overline{2}\,0)$ and $(1\,0\,0)$ systems are calculated to be 1.03 and 1.05 J·m^{-2}, respectively. The simulations therefore predict the $(1\,\overline{2}\,0)$ and $(1\,0\,0)$ surface to have similar energetic stabilities. The calculated $(1\,\overline{2}\,0)$ and $(1\,0\,0)$ surface energies for the varying dopant concentrations are summarized in Table 5.7. As for the pure systems, they were all found to be positive. The change in interfacial energies $(\Delta\gamma)$ of the $(1\,\overline{2}\,0)$ and $(1\,0\,0)$ surfaces relative to their pure counterparts are shown for the different strontium concentrations. The incorporation of dopants are seen to have similar effects on the $(1\,\overline{2}\,0)$ and $(1\,0\,0)$ surfaces with increasing strontium content, with the exception of $\gamma(1.71, 20.0)$. Given that the $\Delta\gamma$ values are negative across all the range, the addition of strontium has a stabilizing effect on the surfaces. Since the $\Delta\gamma$ values generally become more negative for both the $(1\,\overline{2}\,0)$ and $(1\,0\,0)$ surfaces as Sr-content increases, it appears that this stabilization increases with dopant content.

Table 5.7 – Interfacial energies (γ) for Sr-doped β-TCP surfaces. The change in interfacial energy during doping $(\Delta\gamma)$ are given for the doped case at 1400 K.

Strontium content	$(1\,\overline{2}\,0)$		$(1\,0\,0)$	
	γ [J·m^2]	$\Delta\gamma$ [J·m^2]	γ [J·m^2]	$\Delta\gamma$ [J·m^2]
1.00	0.93	-0.11	0.91	-0.15
1.71	0.87	-0.16	0.94	-0.11
2.92	0.90	-0.13	0.92	-0.13
5.00	0.85	-0.18	0.86	-0.20
10.00	0.85	-0.19	0.88	-0.18
20.00	0.83	-0.21	0.95	-0.10
40.00	0.81	-0.23	0.85	-0.20

Table 5.8 – Interfacial energies (γ) for Sr-doped β-TCP grain boundaries. The change in interfacial energy during doping $(\Delta\gamma)$ are given for the doped case at 1400 K.

Strontium content	$(1\,\overline{2}\,0)$		$(1\,0\,0)$	
	γ [J·m^2]	$\Delta\gamma$ [J·m^2]	γ [J·m^2]	$\Delta\gamma$ [J·m^2]
1.00	0.29	0.01	0.87	-0.05
1.71	0.31	0.03	0.83	-0.10
2.92	0.36	0.08	0.81	-0.11
5.00	0.27	-0.01	0.77	-0.15
10.00	0.30	0.02	0.78	-0.15
20.00	0.40	0.12	0.84	-0.08
40.00	0.22	-0.05	0.69	-0.23

Turning our attention to the two grain boundary variants, the grain boundary energies for the pure (1 $\bar{2}$ 0) and (1 0 0) systems were calculated to be 0.28 and 0.92 J·m^{-2}, respectively. Therefore, the (1 $\bar{2}$ 0) grain boundary is predicted to be more stable than the (1 0 0) grain boundary. Table 5.8 then shows grain boundary energies once varying dopant concentrations are factored in. All calculated values were found to the positive. As for the free surface case above, values for the change in interfacial energies ($\Delta\gamma$) of the (1 $\bar{2}$ 0) and (1 0 0) grain boundaries with respect to their pure counterparts are shown. From this, it can be seen that the incorporation of dopants has different effects on both grain boundaries. The addition of strontium has a small stabilizing effect on the (1 0 0) grain boundary, with the $\Delta\gamma$ values of the (1 0 0) grain boundary found to be negative for all dopant concentrations. In contrast, the $\Delta\gamma(5.00, 40.00)$ values were the only ones found to be negative for the (1 $\bar{2}$ 0) grain boundary, albeit very slightly (-0.01 J·m^{-2} and -0.05 J·m^{-2} respectively), while all other values were found to be positive. This result should correlate with the much-reduced segregation of strontium observed for the (1 $\bar{2}$ 0) grain boundaries as compared to the (1 0 0) grain boundaries, as seen in Figures 5.14b and 5.15.

5.3.5   Strontium segregation

In order to consider these differing behaviors further, a thermodynamic quantity of interest is the enthalpy of segregation per dopant ion in an interface structure containing n dopants, calculated by the following equation:

$$\Delta H_{\text{seg}}(n) = \frac{1}{n} \left[H(n) - H(0) - n\Delta H_{\text{b}} \right] \tag{5.8}$$

where $H(n)$ is the enthalpy of the interface structure doped with n atoms, $H(0)$ is the enthalpy of the pure interface, and $n\Delta H_{\text{b}}$ is the change in enthalpy when inserting a dopant ion in the bulk material. Further details on the calculation of the ΔH_{b} term can be found in Appendix C. Finding enthalpies of segregation of $\Delta H_{\text{seg}} < 0$ would indicate that segregation of dopant ions towards the interface is energetically favorable.

The ΔH_{seg} trends of the (1 $\bar{2}$ 0) and (1 0 0) free surfaces are plotted in Figure 5.16a. The ΔH_{seg} values of both surfaces are found to lie between -1.12 and -0.05 eV and -0.87 and -0.04 eV for the (1 $\bar{2}$ 0) and (1 0 0) surface, respectively. Further, both ΔH_{seg} curves become more positive with increasing dopant concentration. A steep incline in the ΔH_{seg} energy is seen up to 9.9% Sr, tending towards plateaus around -0.05 eV between 19.8–39.8% Sr. This suggests that a less pronounced segregation to the (1 $\bar{2}$ 0) and (1 0 0) surfaces would be expected for samples with $\geq 10\%$ Sr content, in keeping with the behavior identified with the MC simulations in Figure 5.14a.

Having considered the surface case, the ΔH_{seg} trends of the (1 $\bar{2}$ 0) and (1 0 0) grain boundaries are plotted in Figure 5.16b. Unlike the surfaces, a distinct difference is
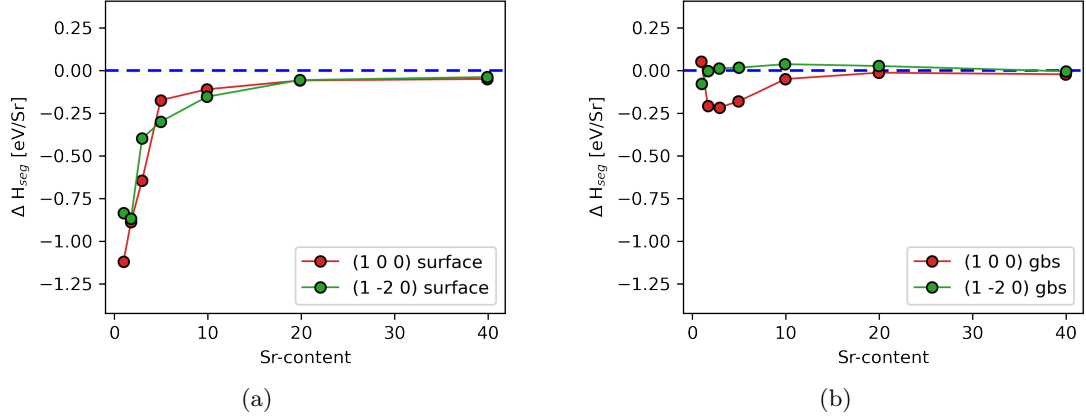
Figure 5.16 – ΔH_{seg} trends for the $(1\,\bar{2}\,0)$ and $(1\,0\,0)$ interfaces: (a) surfaces and (b) grain boundaries.

observed in the ΔH_{seg} trends between the two investigated grain boundaries. A minimum is clearly observed in the ΔH_{seg} curve of the $(1\,0\,0)$ grain boundary at $\Delta H_{\text{seg}}(2.91) =$ -0.21 eV. Apart from the $\Delta H_{\text{seg}}(1.00)$ value that is positive, the $(1\,0\,0)$ ΔH_{seg} curve remains negative, trending to less negative values beyond the minimum at $\Delta H_{\text{seg}}(2.91)$, up towards a plateau of -0.01 eV between 19.8–39.8% Sr. This indicates that the most pronounced segregation of Sr to the $(1\,0\,0)$ grain boundary would be seen at 2.92% strontium content, becoming less favorable and also less pronounced as the strontium content is increased. This is fairly consistent with the MC simulation results shown in Figures 5.14b and 5.15, except that the lower Sr-contents show even stronger relative segregation — a discrepancy that needs further work to understand. In contrast, except for the $\Delta H_{\text{seg}}(1.00)$, the ΔH_{seg} trend of the $(1\,\bar{2}\,0)$ grain boundary features $\Delta H_{\text{seg}} > 0$ across the dopant range, indicating an unfavorable energetic drive for strontium ions to segregate towards the $(1\,\bar{2}\,0)$ grain boundary. Somewhat consistent with this, the Monte Carlo simulations show a much weaker segregation for this grain boundary case.

5.3.6   Conclusions

In this section, the behavior of strontium dopants relative to $(1\,\bar{2}\,0)$ and $(1\,0\,0)$ β-TCP interfaces was investigated using MC simulations. Here, we report the first calculated interfacial energies and enthalpies of segregation for β-TCP surfaces and near-coincidence grain boundaries. The surface energies, γ_{surf}, of the pure $(1\,\bar{2}\,0)$ and $(1\,0\,0)$ systems were calculated to be 1.03 and 1.05 J·m^{-2}, respectively. The introduction of strontium was found to have a stabilizing effect, as the γ_{surf} values become systematically negative as strontium was introduced into the surface structures, for both the $(1\,\bar{2}\,0)$ and $(1\,0\,0)$ surfaces. Correlated to this, the MC simulation results indicate a strong tendency for Sr^{2+}

ions to segregate to the (1 $\overline{2}$ 0) and (1 0 0) surfaces at low Sr content, which becomes weaker as the Sr content increases.

The grain boundary energies, γ_{GB}, for the pure (1 $\overline{2}$ 0) and (1 0 0) systems were calculated to be 0.28 and 0.92 J·m^{-2}, respectively. The introduction of strontium was found to have a stabilizing effect for the (1 0 0) grain boundary, which however was not observed for the (1 $\overline{2}$ 0) grain boundary. The results of the MC simulations also show different segregation tendencies between the (1 $\overline{2}$ 0) and (1 0 0) grain boundaries: a pronounced segregation of Sr is expected to the (1 0 0) grain boundary at low Sr content, while minimal segregation of Sr is expected to the (1 $\overline{2}$ 0) grain boundary. Overall, these preliminary results therefore suggest that Sr-segregation can be expected at certain "special" β-TCP grain boundaries, but perhaps not others. Given the divergent behavior of the two studied grain boundaries, future simulation studies of other grain boundary types are therefore needed to make more generalized conclusions. Considering the challenges involved in experimental measurements of dopant behavior at grain boundaries, as discussed in the next chapter Section 5.4, leveraging the simulation framework in this way will serve as a useful tool for studying the segregation behavior of Sr in β-TCP ceramics.

5.4   Analytical characterization of Sr-doped β-TCP samples

5.4.1   Introduction

Having studied the behavior of strontium dopants at grain boundaries by Monte Carlo (MC) simulations in Section 5.3, in this section we report on preliminary studies of Sr-dopant distributions around grain boundaries using analytical scanning transmission electron microscopy (STEM). In addition to comparing the simulated behavior to these results, we also compare to some analytical data from 3D atom probe tomography measurements. The STEM analyses primarily concern a sintered 5.00% Sr-doped β-TCP ceramic sample prepared by Dr. Bastien Le Gars Santoni during his thesis [19], since this is most directly comparable to the simulated grain boundary structures. However, a β-TCP ceramic (prepared by Le Gars Santoni) using a commercial β-TCP powder from Plasma Biotal is also considered, owing to the results of a correlated analysis of such material using atom probe tomography. The commercial sample is an interesting case because it was not intentionally doped with strontium. Instead, strontium was identified as an impurity of 305 ± 27 ppm, along with Mg and Na at levels of 2110 ± 201 ppm and 276 ± 104 ppm, respectively.

5.4.2   Methods

For the STEM analyses, it was necessary to first prepare suitable electron-transparent lamellae from the sintered ceramic samples. It was required that these lamellae were taken from the interior of the sintered ceramic samples, and that they also contain grain boundaries. In order to ensure this, the following focused ion beam (FIB) method was applied. First, cross-sections of ceramic samples were polished according to the procedure given in Chapter 3, and thermally-etched in order to reveal grain boundaries. Next, they were coated with 5 nm OsO_4 in order to alleviate charging during the FIB milling process. In the FIB machine (Zeiss NVision 40), the scanning electron microscope (SEM) column was used to image the polished and etched surfaces, choosing a region for TEM lamella preparation containing a number of grain boundaries, with at least a couple oriented approximately perpendicular to the lamella length. The lamellae were then extracted, milled and polished with the FIB according to the procedure given in Chapter 3.

The TEM specimens were investigated using a FEI Tecnai Talos Microscope, operated at 200 kV high tension, and equipped with two "ChemiSTEM" silicon drift energy dispersive X-ray spectroscopy (EDXS) detectors. The FIB-prepared lamellae were inserted into a single-tilt low background specimen holder such that the open region of the half-moon shaped support grids were facing the X-ray detectors, thereby maximizing X-ray yield/minimizing X-ray absorption and fluorescence artifacts.

Figure 5.17 shows overview images of the two prepared lamellae, taken in bright-field transmission electron microscopy (TEM) mode using a broad illumination and with a small objective aperture inserted. From the diffraction contrast, different grains can be observed with grain boundaries between them. During FIB milling, a specimen thickness of about 100 nm was targeted, in order to give suitable electron transparency while increasing the X-ray yield compared to much thinner specimens. However, the nature of the β-TCP (for instance, poor conductivity, residual porosity, sensitivity to the ion beam) made FIB milling challenging, such that the final sample thicknesses were not completely uniform. From the TEM image in Figure 5.17a, it can be seen that the Plasma Biotal ceramic was particularly problematic, with FIB beam sensitivity and over-milling leading to amorphization and some large voids (from residual porosity expansion) in the middle of the lamella. Even the top of the sample was too thin for a good X-ray yield. Therefore, the STEM-EDXS analyses were made at the bottom, where the TEM image indicates a greater sample thickness was preserved, and suitable grain boundaries could still be found. In comparison, the 5.00% Sr-doped sample shown in Figure 5.17b is both on average much thicker, and much more uniform in thickness, such that the optimum regions for analysis were in the zone approximately given by the upper three-quarters of the lamella. We also note how the thermal etching of grain boundaries can be observed in projection at the top of the lamellae, at the surfaces underneath the amorphous carbon protection layers.

STEM-EDXS was used for the analytical data acquisition, using an electron probe of $\sim$0.8 nA beam current, and recording spatially-resolved maps using Thermoscientific Velox software. For analyzing the elemental composition at the grain boundaries, we concentrate on grain boundaries that appear close to edge-on and hence parallel to the electron beam, tilting the sample if needed. STEM-EDXS maps were recorded over acquisition times of $\sim$20 minutes, using short pixel dwell times (e.g. 5 µs per pixel) and multi-frame acquisition in order to reduce electron beam damage. In the case of the Plasma Biotal sample, mapping in the over-thinned region of the lamella described above resulted in sample degradation seen immediately after acquisition started. Therefore, as explained earlier, the maps were acquired in the "thick" part of the lamella in order to minimize the damage and maximize the X-ray yield. From the maps, EDXS line profiles are extracted from the most end-on grain boundaries along chords perpendicular to the grain boundary orientations. The line profiles are integrated over many pixels in directions perpendicular to the chords, in order to increase the X-ray signal to noise ratios. All data analyses were performed using the Velox software.

5.4.3   STEM-EDX analysis of the 5.00% Sr-doped β-tcp ceramic

We begin the analysis with the 5.00% Sr-doped β-TCP lamella. In Figure 5.18, annular dark-field STEM images and EDXS maps are shown for two regions of interest, both containing approximately end-on grain boundaries. The Sr EDXS maps, made by

(a)
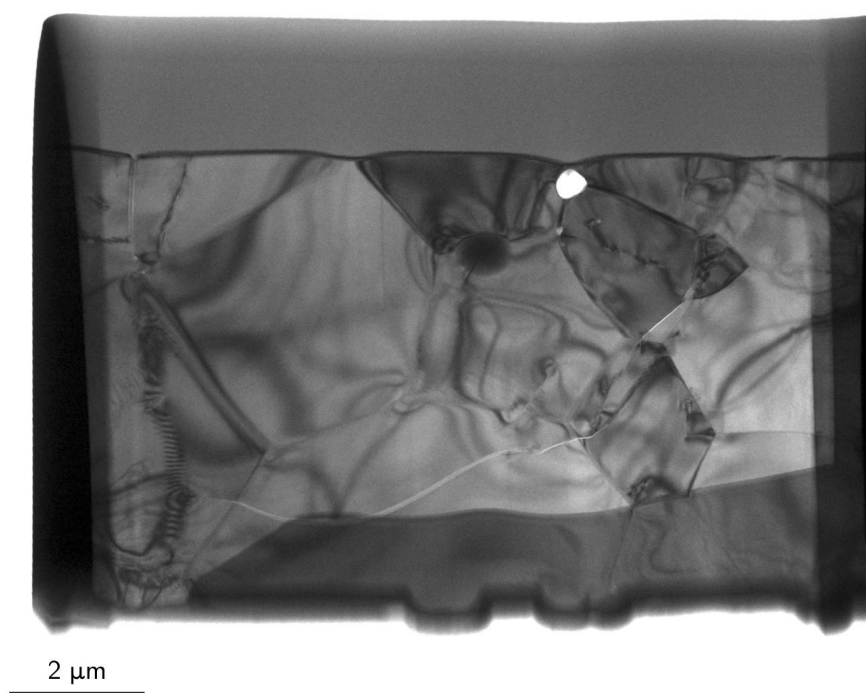
(b)

Figure 5.17 – Bright field TEM image overviews of the (a) Plasma Biotal and (b) 5.00% Sr-doped lamella.
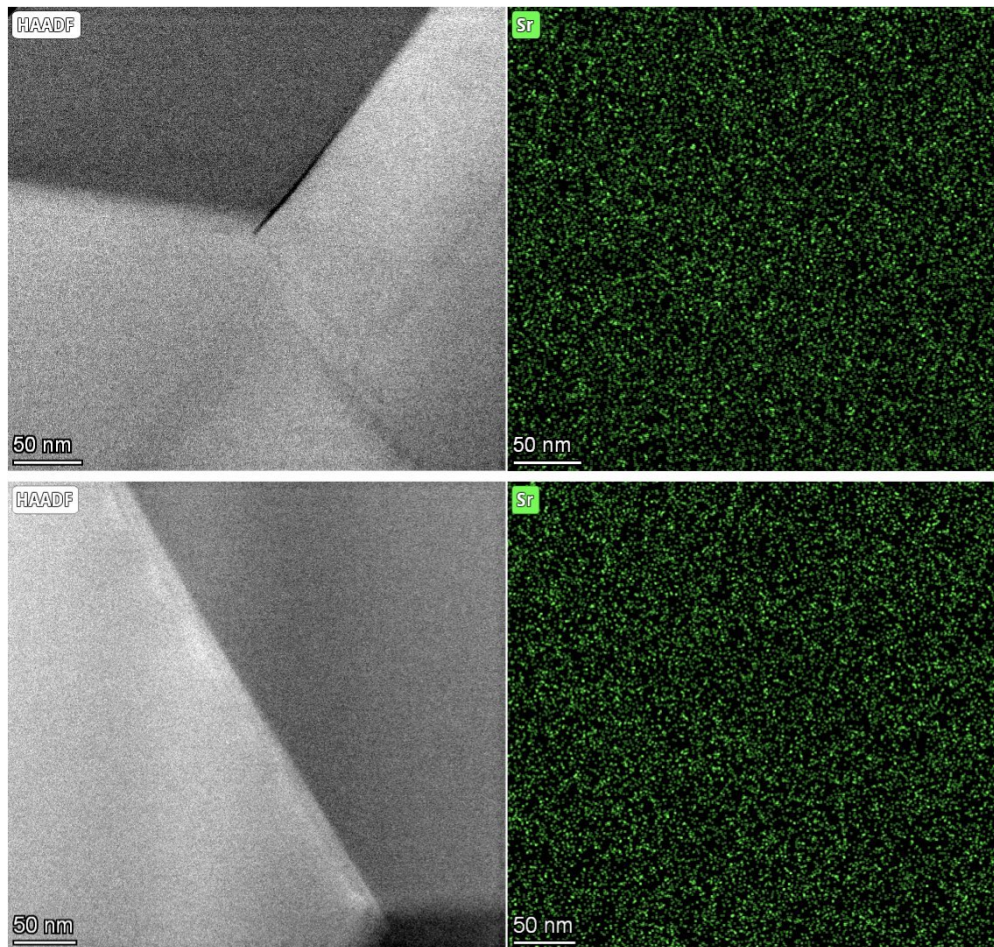
Figure 5.18 – Annular dark-field STEM images and Sr-Kα (14.17 keV) EDXS maps of two regions of the 5.00% Sr-doped sample, each containing end-on grain boundaries. Note that the collection angle on the "HAADF" detector was reduced in order to increase diffraction contrast for grain boundary visibility compared to a classic "Z-contrast" imaging condition.

integrating the signal in the Sr-Kα peak (14.17 keV), do not show any obvious segregation of the dopant. Rather, it appears that there is a homogeneous distribution of Sr across the grain boundaries. In order to verify this, Figure 5.19 shows EDXS line profiles across two grain boundaries, integrated across the widths indicated on the STEM images. As for the maps, no visible segregation can be discerned at the grain boundaries beyond the background (Poisson) noise.

As currently presented, the results of the MC simulations in Section 5.3 and the STEM-EDXS results presented in Figures 5.18 and 5.19 here appear to be at variance. In particular, the MC simulation of the (1 0 0) near coincidence grain boundary identified a strong Sr-dopant segregation for the 5.00% Sr-doped grain boundary structure. In comparison, we have not observed any indications of strontium segregation to grain
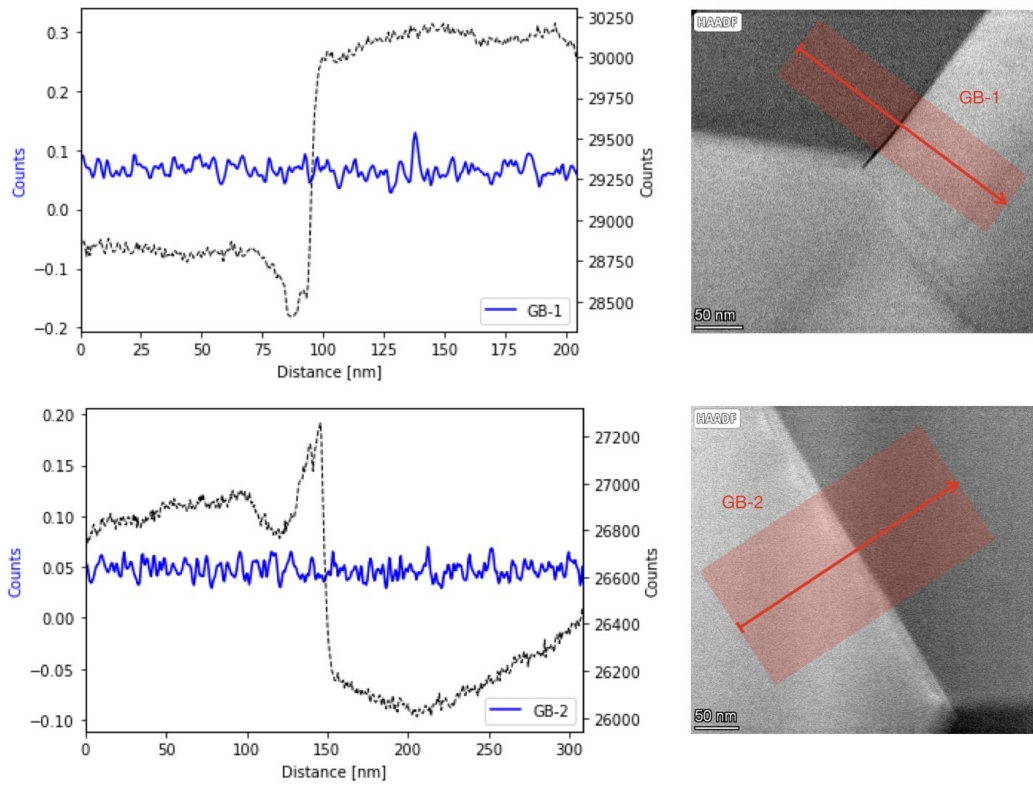
Figure 5.19 – EDXS line scan analysis across two grain boundaries, showing no discernible segregation of Sr to the grain boundaries. The line profile trajectory and integration widths are shown in the STEM image recorded using the HAADF detector.

boundaries in STEM-EDXS analyses of the 5.00% Sr-doped sample, including other maps not shown here. Moreover, additional STEM-EDXS analyses of 5.00% Sr-doped β-TCP powder samples (pre-sintering stage) failed to detect any strontium segregation at grain boundaries.

One plausible explanation for this discrepancy between experiment and simulation is that strontium grain boundary segregation existed in the analyzed sample(s) but, with their sensitivity to the incident electron beam (and charging issues) limiting map acquisition time and incident beam current, the segregation could not be observed with the X-ray signal-to-noise ratios of the acquired map/integrated line profile data. In order to test this hypothesis, we have collaborated with Dr. Adrien Teurtrie of the Electron Spectrometry and Microscopy Laboratory (LSME) in the Institute of Physics (IPHYS) at EPFL. Towards an improved quantification of EDXS data, Dr. Teurtrie has developed an algorithm for simulating EDX spectra and maps for samples of known compositions using physically-based models (currently unpublished work). Starting with the MC-simulated Sr-distribution for the (1 0 0) grain boundary of a 5.00% Sr-doped structure presented in Section 5.3, he has applied this algorithm to simulate an EDXS map and integrated line profile that would be expected for the simulated distribution. The simulation is shown in

Simulated Sr-Kα (14.16 keV) EDXS map

Line intensity of Sr-Kα (14.16 keV)
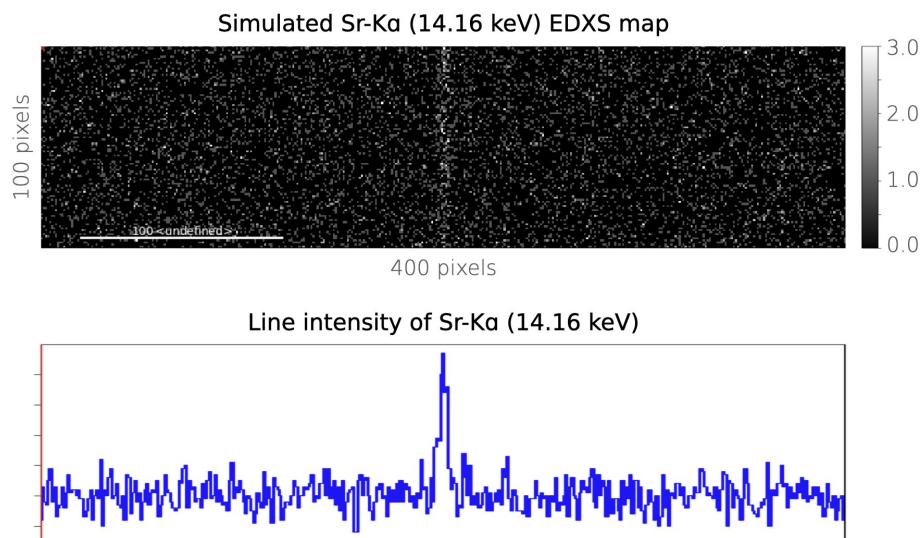
Figure 5.20 – Simulated Sr-Kα EDXS map (100 x 400 pixel^2) and integrated line profile of the 5.00% Sr-doped. The x-axis of the line profile is a spatial dimension that represents both the electron probe size and spatial sampling frequency. The simulated grain boundary has a Gaussian shape with a full width half maximum of 5 pixels, which should be similar to the grain boundary pixel width in the experimental data.

Figure 5.20. For suitable comparison to the experimentally-acquired data, the simulation applies an X-ray signal intensity equivalent to the experimental data, along with suitable detector characteristics, Poisson noise, etc. Specifically, it applies a total number of counts per pixel spectrum of 15, as similar to the experimental data. The elements Sr, Ca and P (and Cu from the grid) were simulated, using theoretical cross-sections.

In the simulated EDXS data of Figure 5.20, it is clear that we would expect to detect the Sr-segregation to the grain boundary if such a grain boundary was measured experimentally, even with the limited signal-to-noise ratio of the acquired data. At the simulated grain boundary there is clear a Sr-enrichment of the β-TCP phase, with four times more Sr than the bulk. (The Ca-content — not shown — decreases accordingly at the grain boundary.) In consequence, other explanations must be sought for the variance between the simulated and experimental results. Possibilities include:

- In Section 5.3, two near-coincidence grain boundaries were simulated, of which only the (1 0 0) variant showed significant segregation of strontium to the grain boundary. The (1 $\bar{2}$ 0) grain boundary showed much lower segregation. If such a boundary was sampled by STEM-EDXS, it would be more challenging to discern this low level of segregation. (Further EDXS data simulations, based on the (1 $\bar{2}$ 0) grain boundary simulation would be useful to pursue this concept.)

- In the case that there are certain "special" grain boundaries that show strong segregation, and others that only shown minimal segregation, all of the current simulations and experimental data are essentially preliminary, because in both cases we have insufficient data points to make conclusions. More simulations are needed to estimate some likelihood of "special" grain boundaries. Analytical characterization of many more grain boundaries might be required to find and measure such a "special" grain boundary.

- The simulated grain boundary structures have a distance between the two grain boundaries of 7.5 nm. Compared to this, the actual grain sizes observed in TEM are much larger, in the order of hundreds of nm to a few µm. We know that the β-TCP lattice easily accommodates Sr dopants (see Section 5.1). Consistent with this, quantification of integrated EDXS spectra from the bulk of the grains in the 5.00% Sr-doped sample finds a Sr-content of $\sim$4.2%. Within the accuracy of the quantification, this cannot be judged different to the nominal 5.00% Sr-content. In such a case where the lattice accepts the dopant so readily, it is conceivable that grain boundary segregation effects will substantially reduce as grain size is increased, correlated to the reduction in the volume ratio of grain boundary/bulk. Therefore, any potential segregation for grains of a few µm in size might be reduced to a level that is too small to measure within the precision of the STEM-EDXS technique.

- STEM-EDXS orientation effects should also be considered. The simulated profile shown in Figure 5.20 is for an ideal sampling geometry, with the incident electron beam perfectly parallel to a perfectly flat grain boundary. Such a geometry will maximize the possible segregation signature. In reality, as can be seen in the TEM images of Figure 5.17, the grain boundaries are never perfectly flat. In addition, the boundaries sampled by STEM-EDXS are not necessarily fully parallel to the incident electron beam. Any deviations from these two ideal conditions would reduce the strength of measurable segregation, since in the projection of the lamella the boundary will be sampled over a greater pixel width. While this alone is unlikely to account for the discrepancy between the simulated profile and the experimental data, owing to the strength of observable segregation in the former, it would be interesting to look further into this issue by simulated EDXS maps and profiles for tilted grain boundaries.

5.4.4   STEM-EDXS analysis of the Plasma Biotal ceramic

In contrast with the STEM-EDXS results from the 5.00% Sr-doped sample presented above, a recent study using 3D atom probe tomography (APT) is suggestive of the experimental observation of dopant segregation in a sintered β-TCP ceramic. The analysis was made on a sample sintered from the commercial Plasma Biotal precursor, and was done in collaboration with Torsten Schwartz and Dr. Baptiste Gault at the MPIE Max Planck

Institute. In their preliminary (currently unpublished) analysis, the atomic distribution of a FIB-milled pillar of Plasma Biotal ceramic was measured in 3D using APT. The left-hand side of Figure 5.21 shows a rendering of the 3D compositional data-set, in a needle volume measuring about 120 nm in length and 50–90 nm in diameter. Slanted relative to the needle's axis, a plane of dopant species segregation is observed. On the right-hand side of Figure 5.21, integrated line-profiles of different dopant species are extracted on a chord perpendicular to this plane, using a 0.3 nm bin size. Assuming that this plane corresponds to a grain boundary, the figure shows a clear segregation of Sr and Na, with no clear influence of the grain boundary on the Mg distribution. This result could well be the first positive identification of dopant segregation in a β-TCP ceramic.
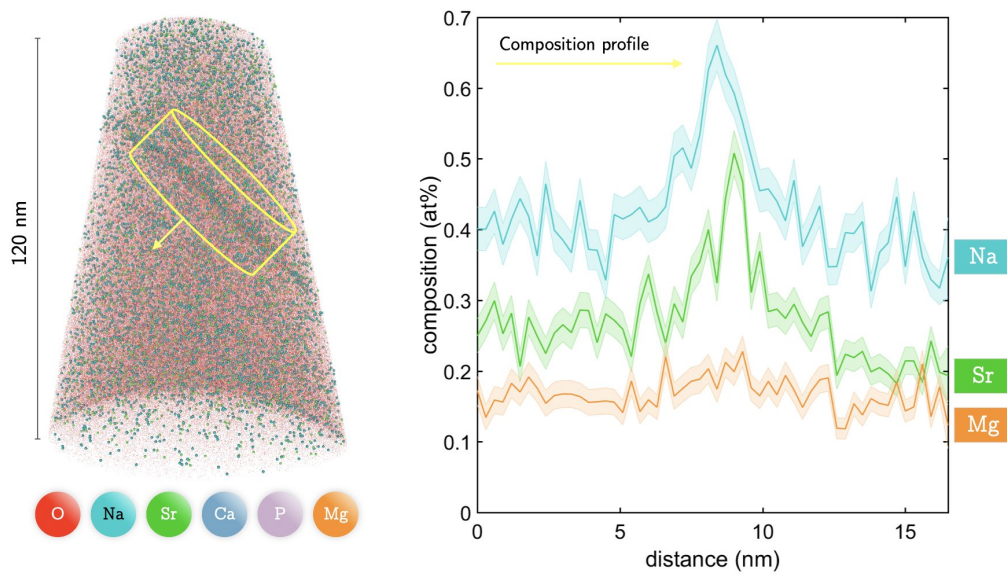
Figure 5.21 – 3D elemental compositional rendering (left) and extracted integrated line profiles (right) from APT analysis of a needle-shaped sample prepared by FIB from a sintered Plasma Biotal-based β-TCP ceramic. Figures by Torsten Schwartz and Dr. Baptiste Gault at the MPIE Max Planck Institute (unpublished).

Stimulated by this result, we set out to make a comparative analysis of an equivalent sample of sintered Plasma Biotal β-TCP ceramic using STEM-EDXS, with the sample prepared by FIB as described in the Methods, and with Figure 5.17a showing the overview TEM image of the lamella. Figure 5.22 presents an example EDX spectrum from the lamella, integrated from a large number of spatially-mapped pixels. A summary of the identified peaks and where they come from are summarized in Appendix C. As described in the Methods section, the map was made in the thickest region of the TEM lamella in order to maximize X-ray yield and minimize electron beam induced damage. Because of the very low levels of the Sr and Na dopant impurities (each $\sim$300 ppm), neither species gives discernible X-ray peaks {Sr-Kα (14.17 keV), Sr-Kβ (15.84 kev), Sr-Lα (1.81 keV)} and {Na-Kα (1.04 keV)} in the integrated spectrum. Considering that the

integrated spectrum gives the highest possible X-ray spectral signal of the map data-set, it is therefore impossible to study their spatial distribution in the STEM-EDXS map data. As a result, we cannot obtain confirmatory data for the APT observation of segregation of these two dopant impurities. In contrast, the Mg impurity is present at an order of magnitude higher level of $\sim$2000 ppm, and has a distinct and visible Kα peak {Mg-Kα (1.25 keV)} in the integrated spectrum. Figure 5.23 shows a line profile for the Mg-Kα peak signal, made across the indicated grain boundary. No segregation is discernible. However, this dopant did not show any segregation in the APT analysis either (see Figure 5.21), such that the two results are consistent.
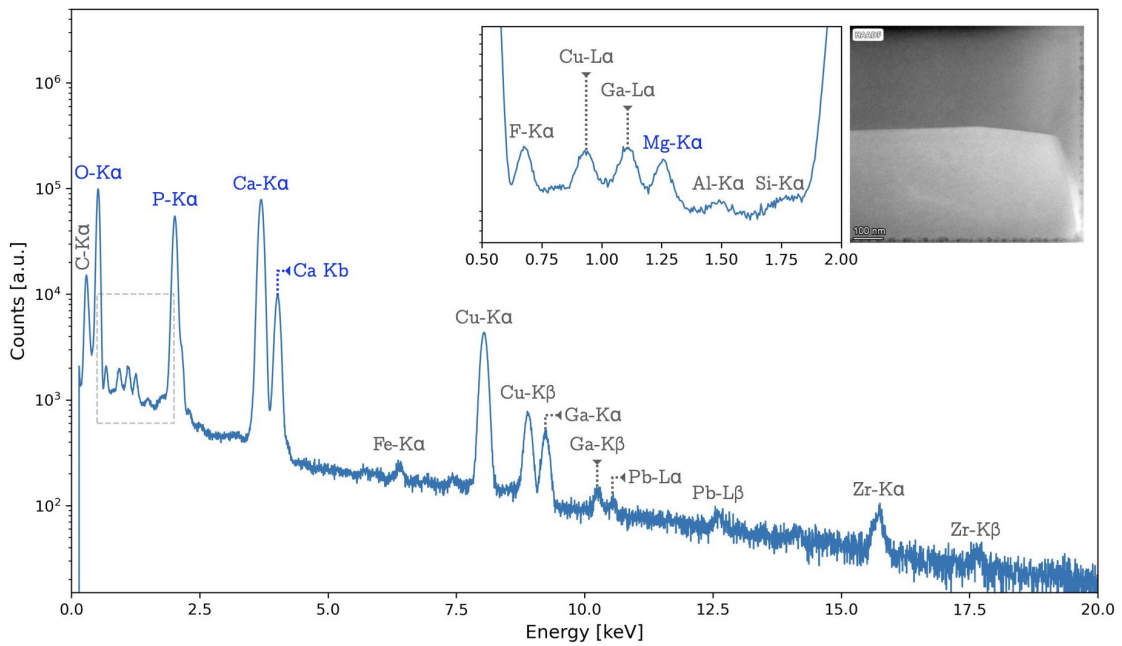
Figure 5.22 – Example integrated EDX spectrum of Plasma Biotal TEM lamella, integrated from the region shown on the accompanying HAADF-STEM image.
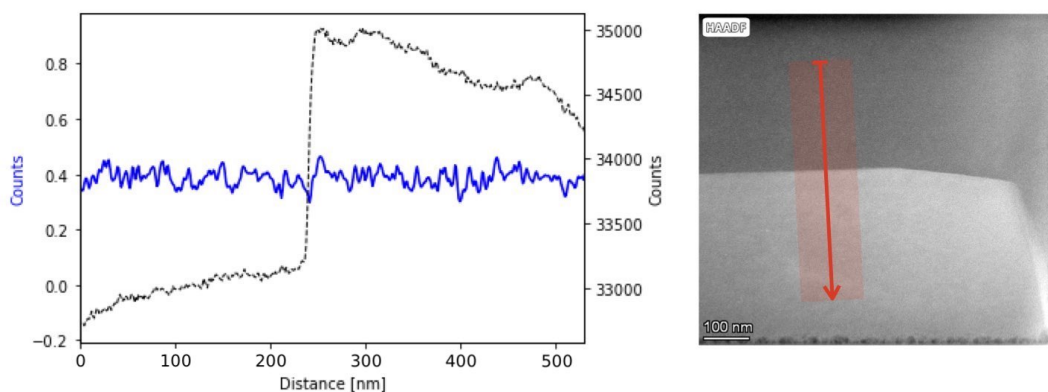
Figure 5.23 – Line profile of Mg-Kα line, integrated across a grain boundary as shown in the accompanying HAADF-STEM image.

In summary, the STEM-EDXS analysis cannot provide any confirmation for the APT observation of Sr and Na dopant segregation in the Plasma Biotal sample. Pursuant to this, we also emphasize the preliminary and unconfirmed nature of the APT result. Two particular points should be kept in mind:

- The APT analysis was not accompanied by a correlated structural characterization of the needle, for instance by TEM before the APT run. This characterization would be needed in order to confirm that the plane of elemental segregation definitively corresponds to a grain boundary. Currently, the grain boundary nature is hypothesized from the observation of the plane of dopant segregation.

- The positive identification of segregation by APT shown in Figure 5.21 is a one-off result. The same team at MPIE has made at least four similar analyses on samples of the high purity 5.00% Sr-doped without any observation of Sr-dopant segregation. However, without any structural analysis, it is unknown whether the analyzed needles of material contained grain boundaries or not. Therefore, even this result cannot give any full verification of dopant behavior at grain boundaries.

5.4.5 Concluding remarks

In this section, preliminary efforts were made to experimentally characterize dopant behavior across grain boundaries in sintered β-TCP samples, and correlate to the results from atomistic simulations. Both the simulations and the experimental characterizations present strong limitations in terms of sampling statistics (i.e. number of grain boundary variants simulated, numbers of grain boundaries experimentally-measured). This prevents making definitive conclusions at this stage.

That said, we can expect that a grain boundary showing segregation of the level shown by the (1 0 0) grain boundary structure having 5.00%-Sr-doping would be observed using our STEM-EDXS protocol, even though our X-ray peak signal-to-noise ratios are inherently limited by the beam dose supported by the sample and charging issues (see Chapter 3 for details). Various reasons have been proposed for the actual experimental results of no observable dopant segregation in the 5.00% Sr-doped sample.

The APT result suggesting Sr and Na segregation at a grain boundary from the Plasma Biotal sample that features these dopants as very low-level impurities ($\sim$300 ppm) is, however, impossible to verify with our STEM-EDXS methods, given the unmeasurable signal from the two species. While this APT result remains a one-off, hypothetically it could correlate well with the MC-simulation results of Section 5.3. In that section, it was found that lower levels of Sr-dopant gave stronger relative grain boundary segregation (χ_{GB}:χ_{bulk} values) than higher dopant levels. According to this, the very low levels of Sr dopant in the Plasma Biotal sample, as compared to the otherwise-studied 5.00% Sr-doped

sample, may actually favor positive observation of dopant segregation at grain boundaries. This suggests that future characterization studies of Sr-dopants are preferably made with samples having lower dopant levels than the 5.00% Sr-doped sample. Practically, such samples will need to be analyzed by APT, not STEM-EDXS, because of the much greater sensitivity of the former technique for measuring low dopant concentrations. However, given that the grains in these samples are large and hence rare compared to the size of an APT needle, we advise that such APT studies are made with correlative TEM measurements in order to have confirmatory structural information on the presence of a grain boundary in the APT needle before the APT measurement is made.

6 Documentation and characterization of β-TCP powders and ceramics by electron microscopy

In the context of the SNSF project (Sinterphos No. 200021_169027), the β-TCP powders and ceramics studied throughout the thesis were prepared by Bastien Le Gars Santoni as part of the project and his PhD thesis at the RMS Foundation (Bettlach, CH). Throughout the project, one of the main electron microscopy aims was to document and characterize the β-TCP powders and ceramics during the various stages of production — precipitated powders, calcined powders, sintered ceramics (before and after polishing), after various treatments for XRD analysis, and after *in vitro* resorbability tests. In order to illustrate this extensive documentation project — as carried out by the thesis author — this chapter will begin by presenting examples of the powder and ceramic characterization carried out by electron microscopy and highlight where these have been an integral part of the success of the encompassing SNSF project. Then, the case of copper-doped β-TCP samples will be described in more detail, as it is of particular interest. Data access for the complete electron microscopy documentation linked to the project will be provided in an online repository.

6.1   Documentation of β-TCP powders and ceramics

All β-TCP powder synthesis and dense ceramics fabrication were performed by Dr. Bastien Le Gars Santoni at the Robert Mathys Stifung (RMS) Foundation under the direction of Dr. Marc Bohner. Details of the synthesis method can be found in the thesis of Dr. Bastien Le Gars Santoni [19]. Linked to this synthesis effort, the documentation of powders and ceramics was a major experimental effort during this thesis, involving the scanning electron microscopy (SEM) imaging and cataloging of approximately 64 samples at different stages of five fabrication routes. The catalogue also includes upwards of 160 samples from cell culture tests, also carried out by Dr. Bastien Le Gars Santoni in collaboration with Prof. Wilhelm Hofstetter (University of Bern), in order to document the changes in topographical features created under varying conditions.

As a first example of this work, the synthesized powders were imaged by SEM at various stages of the fabrication procedure as a quality assurance step, see Figure 6.1 for overviews of the β-TCP powders. The initial stage of documenting begins with the calcium deficient hydroxyapatite (CDHA) powders after synthesis and drying, shown in Figure 6.1a. The second stage images the β-TCP powders formed after the thermal treatment (850℃, 1h), shown in Figure 6.1b. Between this stage and the previous stage, it is clear that the thermal treatment decreases the particle specific surface area. After the thermal treatment, the powders are ground in a ball-mill for 2h in ultra pure water in order to destroy agglomerates formed during the thermal treatment, producing the material shown in Figure 6.1c. The last stage of the powder documentation is the powder after it has been thermally-treated for analysis with XRD, shown in Figure 6.1d. This stage is useful to document as it is the only powder that can be imaged in the transmission electron microscope (TEM).

The surfaces of β-TCP cylinders at various stages of the cell culture tests were also observed in SEM imaging to monitor the changes in topographical features caused by cell-mediated resorption of the polished surfaces. In order to bring out imaging contrast for these features, the samples are visualized with the Everhart-Thronley detector at an accelerating voltage of 1.00 kV and probe current of 80 pA with a working distance between 4.0 - 5.0 mm. The main states of interest include: the polished surface (as a control surface); after 24 h in cell-culture medium; after 24 h of osteoclast resorption; and after 24 h of exposure to cell-culture medium with macrophages, see Figure 6.2.

In this example, immersion of the β-TCP cylinder in the cell medium leads to dissolution around the grain boundaries and the polishing lines, as shown in Figure 6.2b. Osteoclasts are the main cells responsible for bone resorption and remodeling. As seen in Figure 6.2c, the osteoclast resorption brings out distinct features. The resorbed grains reveal needles and pillars on their surfaces, suggestive of specific resorption mechanisms. In contrast, exposure to the cell culture medium with macrophages (Figure

(a)

(b)

(c)

(d)
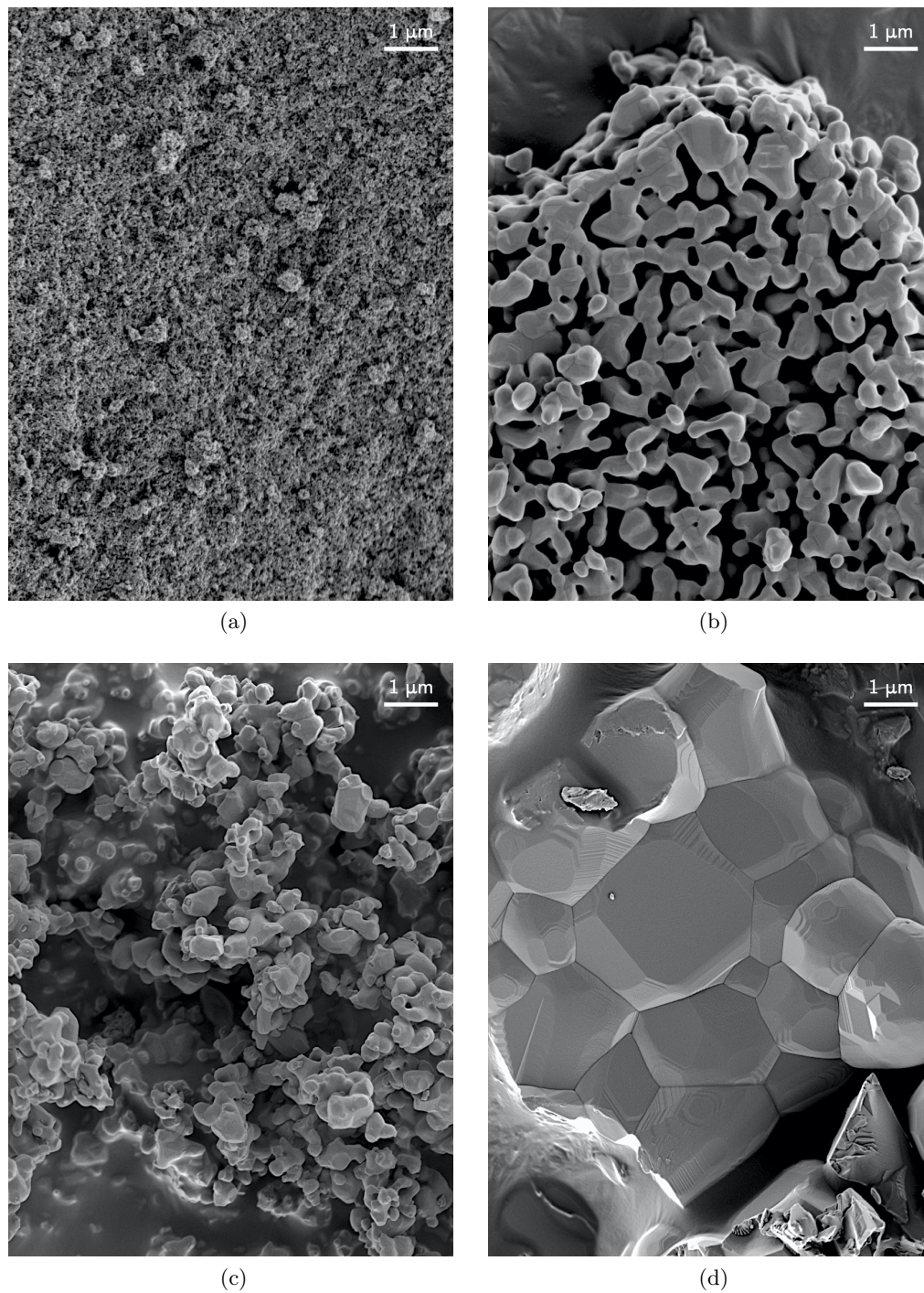
Figure 6.1 – SE-SEM images of 5.00% Sr-doped β-TCP powders (a) after synthesis and drying, (b) after thermal treatment, (c) after ball mill grinding for 2 h, and (d) after thermal treatment for XRD analysis. Powders are coated with 5 nm of conductive OsO_4 prior to SEM imaging. All images are acquired with the following parameters: 1.00 kV high tension, 80 pA probe current, at working distances between 2.3 - 3.0 mm, using the In-Lens SE detector.
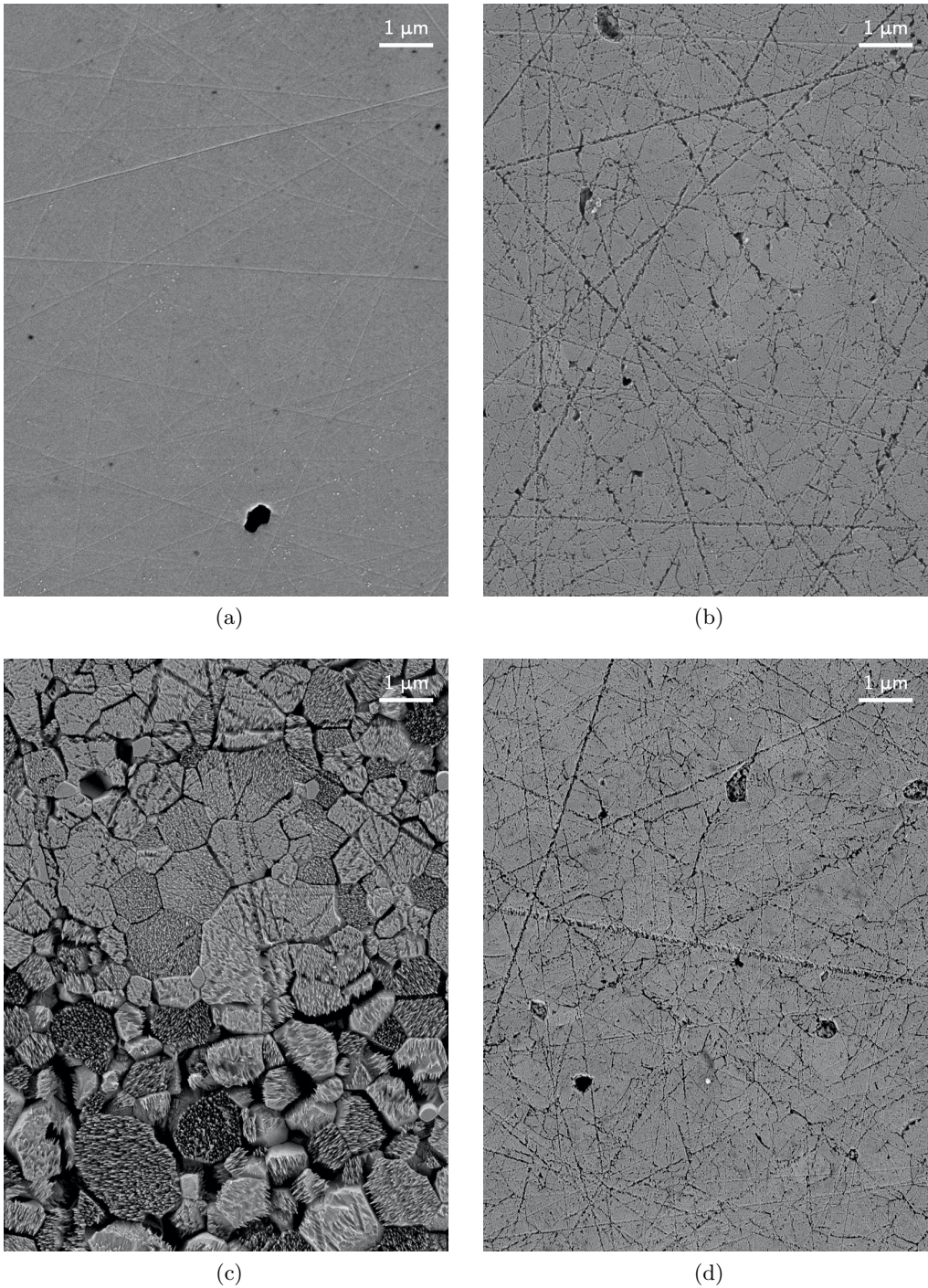
Figure 6.2 – SE-SEM images of pure β-TCP ceramic surfaces after: (a) polishing, (b) after 24 h in cell culture medium, (c) after 24 h in cell culture medium with osteoclasts, and (d) after 24 h in cell culture medium with macrophages.

6.2d) produces a surface that closely resembles the that of the pure cell culture medium, possibly suggesting that macrophages do not interact with the surface of the ceramics.

Figures 6.3 and 6.4 present examples of how the SEM documentation work and resulting image catalogue has contributed to journal publications. The images can be found in the article "Chemically pure β-tricalcium phosphate powders: Evidence of two crystal structures" [38] that features the comparison of β-TCP obtained from calcium deficient hydroxyapatite (CDHA) powders synthesized at various pH levels. This article presents two comparisons of the fabrication steps. The first, shown in Figure 6.3, shows CDHA powders precipitated at different synthesis pH. The change in synthesis pH is seen to significantly affects the morphology of the particles: the evolution observed shows elongated platelets at acidic pH (Figure 6.3a) which become equiaxed particles at basic pH (Figures 6.3c and 6.3d) [38].

The second, shown in Figure 6.4, shows β-TCP powders following the thermal treatment of the CDHA powders precipitated at different pH. Similar to the CDHA powders, the morphologies of the β-TCP powders are affected by the synthesis pH. This evolution goes from rectangular platelets at acidic pH (Figure 6.4a) to equiaxed-facetted particles at more basic pH (Figures 6.4b–d) [38]. It is also noted that, the proportion of smaller fused particles increased with the increase in synthesis pH 8.0–9.0 (noted by the red arrows).

The catalogue has also been used in the article "β-tricalcium phosphate for bone substitution: Synthesis and properties" [68] to compare the morphologies of β-TCP synthesized under various conditions, see Figure 6.5. Here, the catalogue images are used in the panels Figure 6.5g and h, in order to aid comparison to other β-TCP powders that are synthesized under different conditions: by precipitation in organic media (Figures 6.5a–c), by calcination of amorphous calcium phosphate (ACP) produced by flame-spray synthesis (Figure 6.5d and 6.5e), or, in the catalogue data, by thermal conversion of calcium deficient hydroxyapatite (CDHA) (Figure 6.5g and 6.5h). Other interesting morphologies include a commercial β-TCP powder (Aldrich, Art No 20218) (Figure 6.5f) and β-TCP fibers (Figure 6.5i).

The final example of application of the catalogue can be found in the article "Effects of minor amounts of β-calcium pyrophosphate and hydroxyapatite on the physico-chemical properties and osteoclastic respiration of β-tricalcium phosphate cylinders" [69]. In this example, Figure 6.6 presents sections of β-TCP cylinders with variable Ca:P ratios, and compares the polished surfaces to the same type of surfaces after 24 h in cell culture medium with and without HCl, with macrophages, and with osteoclasts. In comparison to the initial polished surfaces, the surfaces after 24 h immersion in cell culture medium shows dissolution along the grain boundaries and the polishing lines (similar to Figure 6.2). The effect is more pronounced in the cell culture medium with HCl as compared to the one without. In contrast, exposure to osteoclasts gives very strong changes in
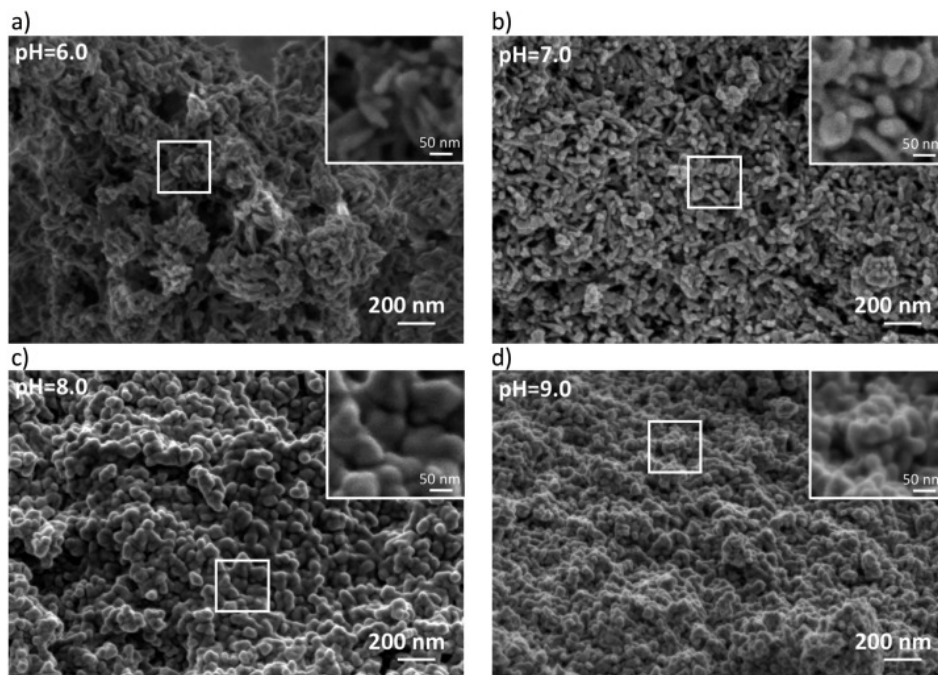
Figure 6.3 – SEM images as presented in Reference [38] of CDHA powders obtained after different synthesis pH and subsequent drying at 70℃; (a) pH 6.0, (b) pH 7.0, (c) pH 8.0, and (d) pH 9.0.
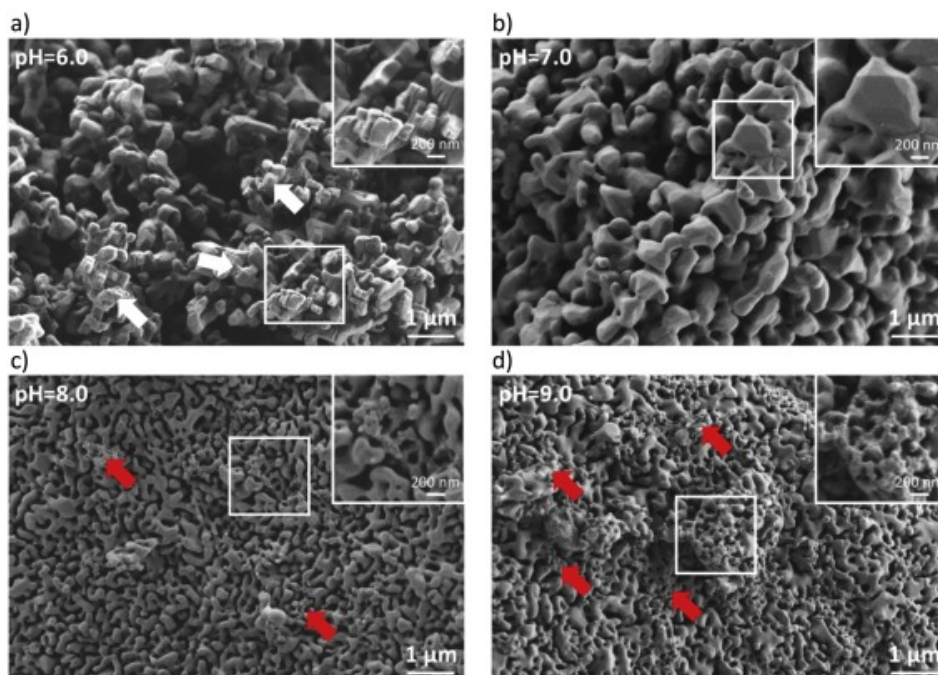
Figure 6.4 – SEM images as presented in Reference [38] of β-TCP powders obtained after thermal treatment (850℃, 1 h) of CDHA powders synthesized at (a) pH 6.0, (b) pH 7.0, (c) pH 8.0, and (d) pH 9.0.
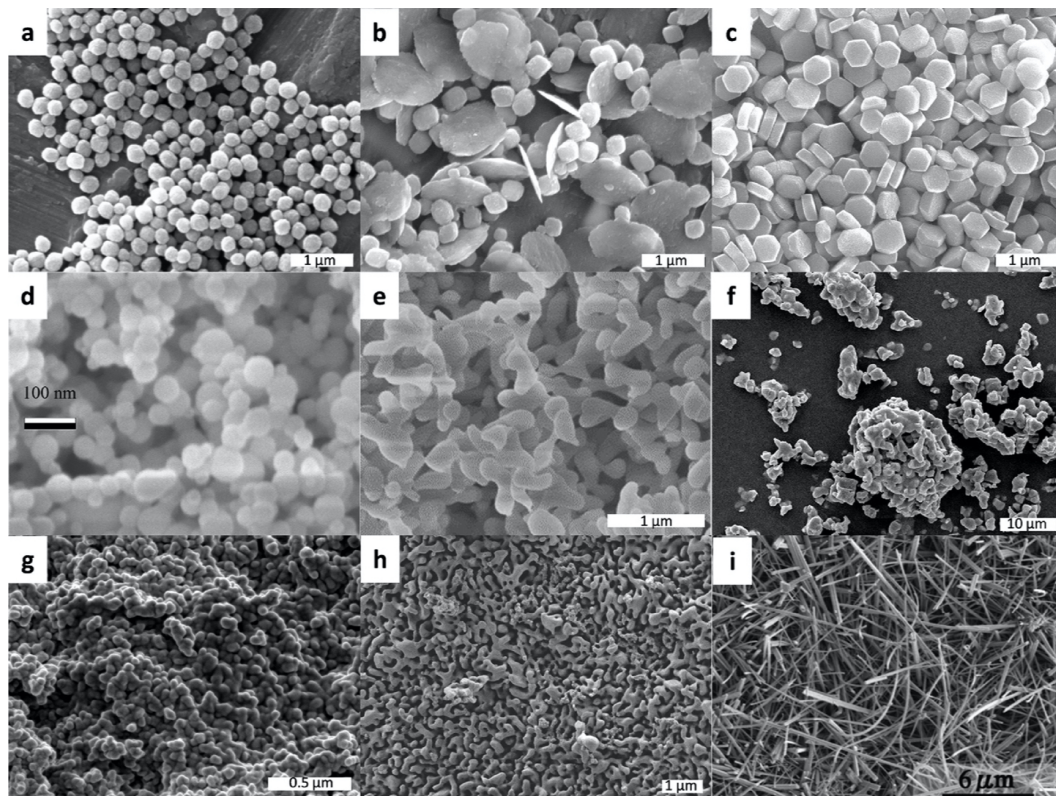
Figure 6.5 – SEM images as presented in Reference [68] of β-TCP particle morphologies. Uses of the catalogue are the CDHA and β-TCP powders presented in (g) and (h), respectively.

surface topology. Not only does the evident resorption appear to depend on Ca:P ratio, as concluded in Reference [69] the images reveal that "the resorption of β-TCP cylinders was inhomogeneous, regardless of Ca/P molar ratio".

The full catalogue of documented β-TCP powders and ceramics will be made available on an online database.
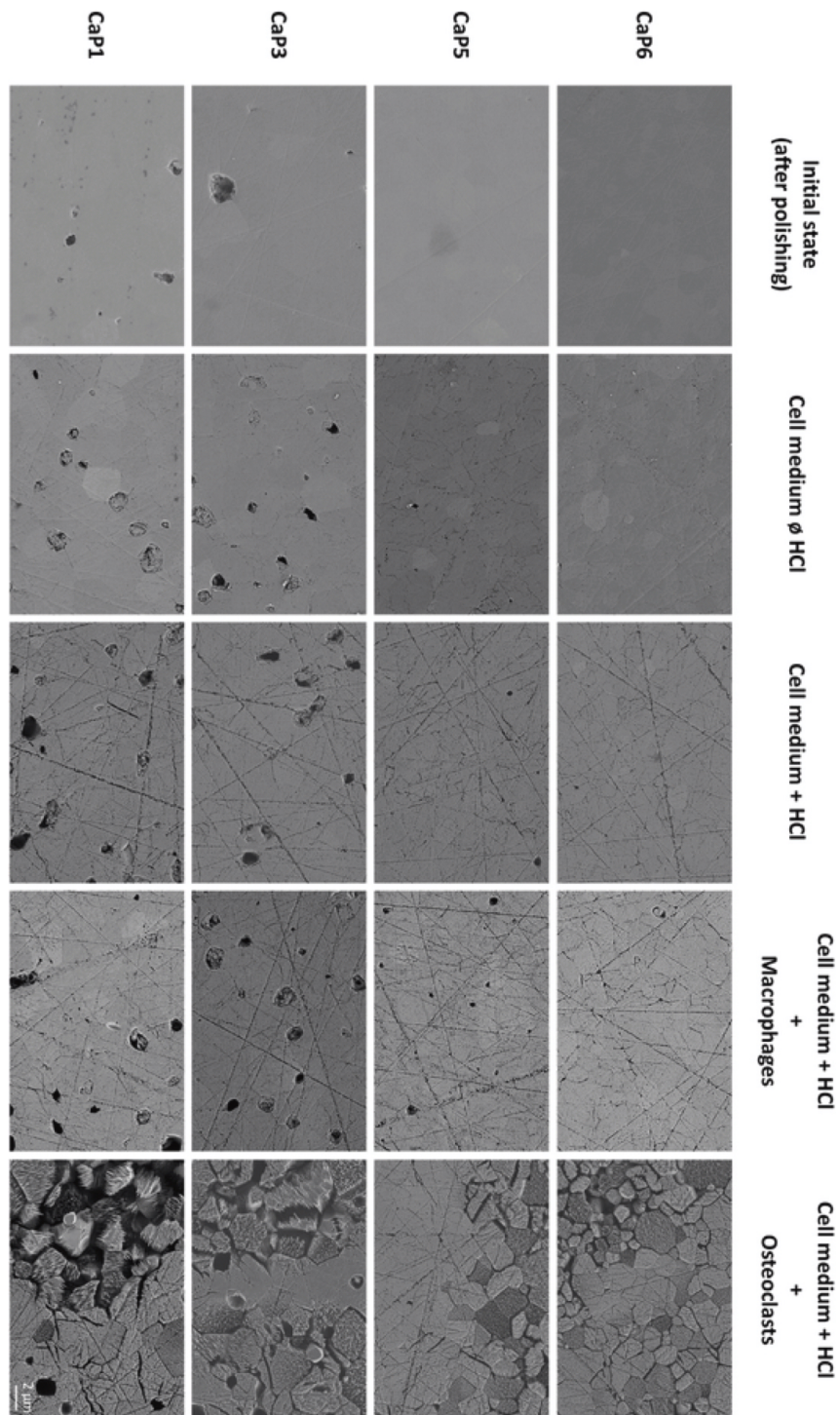
Figure 6.6 – SE SEM images as presented in Reference [69] of β-TCP surfaces synthesized under pH conditions: CaP1 (Ca/P = 1.496), CaP3 (Ca/P = 1.497), CaP5 (Ca/P = 1.500), and CaP6 (Ca/P = 1.502).

6.2 Characterization of a 5.00% Cu-doped β-TCP ceramic by electron microscopy

6.2.1 Introduction

The leading cause of orthopaedic implant removals is post-operative infection [70–73]; approximately 20% of implant failures are attributed to infection [70, 74]. Despite the biocompatibility of bone graft implants, bacteria easily and readily colonize these surfaces. Once bacteria adhere to the surface, they are substantially more difficult to eradicate than individual suspended bacteria floating around the body [75, 76]. Adherent bacteria are largely resistant to antibiotics, immune cells, and other potential infection defense mechanisms [77]. Therefore, it is crucial to minimize the chance of high-density bacterial formation as early as possible. One of the potential design strategies to address the challenge of bacterial infection of implants is the use of copper doping. Various studies have shown that Cu^{2+} ions can increase the antibacterial and antimicrobial activity of tricalcium phosphate or other medical implants [75, 78, 79]. In addition, Cu also shows a positive influence on wound healing and angiogenesis [80].

In doping studies, Cu^{2+} has been shown to incorporate into the β-TCP crystal structure, with a preference to substitute first at the Ca(5) site [81]. However, unlike other small divalent ions, like Mg^{2+} ($r = 0.72$ Å) and Zn^{2+} ($r = 0.74$ Å), Cu^{2+} ($r = 0.73$ Å) does not occupy the Ca(4) site when the Ca(5) site is filled [81]. Following the filling of the Ca(5) site, Cu^{2+} has been shown to substitute for Ca^{2+} at the Ca(3) site; the last site occupied is the Ca(2) site, at doping levels between 12–15 at.% Cu [82–84]. Spaeth et al. [81] did not detect any CuO in their samples by Rietveld refinement analysis of their XRD, and therefore assumed that all Cu^{2+} ions were incorporated in β-TCP . The first appearance of a copper containing secondary phase, $Ca_3Cu_3(PO_4)_4$, was at Cu^{2+} content of 15 at%. The presence of $Ca_3Cu_3(PO_4)_4$ was also detected in the co-doping study performed by Matsumoto et al. [85].

We are limited in our ability to explore Cu-doped β-TCP using atomistic simulations, because Cu^{2+} potentials have not yet been developed for calcium phosphate systems, including β-TCP . Therefore, considering the potential utility of Cu-doped β-TCP, in this section we investigate such synthesized ceramics using analytical electron microscopy.

We first look at polished cross-sections of β-TCP slip cast and sintered ceramics doped with varying Cu-concentrations (0.10%, 1.00%, 2.92%, and 5.00% Cu), in order to determine the distribution of the Cu-dopants within them. These Cu-doped samples were prepared by Dr. Bastien Le Gars Santoni during his PhD thesis research [19]. This analysis was performed by scanning electron microscopy (SEM) combined with energy dispersive X-ray spectroscopy (EDXS) using the Zeiss Merlin instrument and Oxford Instruments X-Max Extreme EDXS detector (see Chapter 3). SEM-EDXS maps were acquired with an 8.00 kV electron beam and 1 nA probe current at a 5.5 mm working

distance. Each map was acquired for $\sim$20 min. over a 24.2 µm $\times$ 24.2 µm area (pixel size of 0.06 µm) with a pixel dwell time of 170 µs. Figure 6.7 shows secondary electron (SE) SEM images of regions mapped in 0.10%, 1.00%, 2.92% and 5.00% Cu-doped β-TCP ceramics, along with Cu maps integrated from the Cu Lα (0.93 keV) peak. While the 0.10%, 1.00% and 2.92% Cu-doped samples appear to show uniform distributions for the Cu dopants (as much as can be ascertained when accounting for signal and random noise fluctuations), surprisingly the 5.00% Cu-doped sample reveals a distinct spatial segregation of Cu into small localized regions on the map. Given that the same localized regions also show a brighter signal in the SE-SEM image, it suggests the presence of a Cu-rich secondary phase.

In order to study this possibility in more detail, further analysis was made by STEM investigation of a FIB-prepared lamella. This investigation had two aims: (1) to characterize the Cu-rich secondary phase, and (2) to determine the distribution of Cu across grain boundaries. Understanding of these two factors is relevant for evaluating the release of Cu^{2+} ions during medical applications of Cu-doped β-TCP. If the potential of Cu^{2+} doping for preventing bacterial infections is going to be realized, it is necessary to manage the Cu^{2+} release in order to maintain good bioactivity and biocompatibility. In particular, the "burst release" of Cu^{2+} ions coming from the dissolution of Cu-rich phases must be avoided. Instead an ideal dissolution profile would be the gradual release of Cu^{2+} ions over long periods of time [85].

6.2.2   FIB sample preparation

The FIB lamella, prepared by Dr. Barbora Bártová, was produced by the standard lift-out process following the procedure detailed in Chapter 3. It was mounted on a Si-half grid in order to prevent having an artifact Cu signal arising from X-ray fluorescence from the support grid, as would occur with using a standard Cu-half grid. Because the β-TCP ceramics are not highly conductive, prior to FIB milling, the sample was coated with 5 nm OsO$_4$ to alleviate charging during the milling process. Using imaging with the SEM column of the FIB, a site of interest for lamella preparation was chosen containing one of the secondary phase precipitates with a bright contrast. This region of interest was further coated with an electron beam and then ion beam deposited carbon protective layer to prevent FIB-induced surface damage or modification. The HAADF-STEM image overview of the final lamella, presented in Figure 6.8, shows that, in addition to sectioning one of the Cu-rich precipitates at the surface, a number of grain boundaries are also captured within the lamella.

(a)

(b)

(c)

(d)
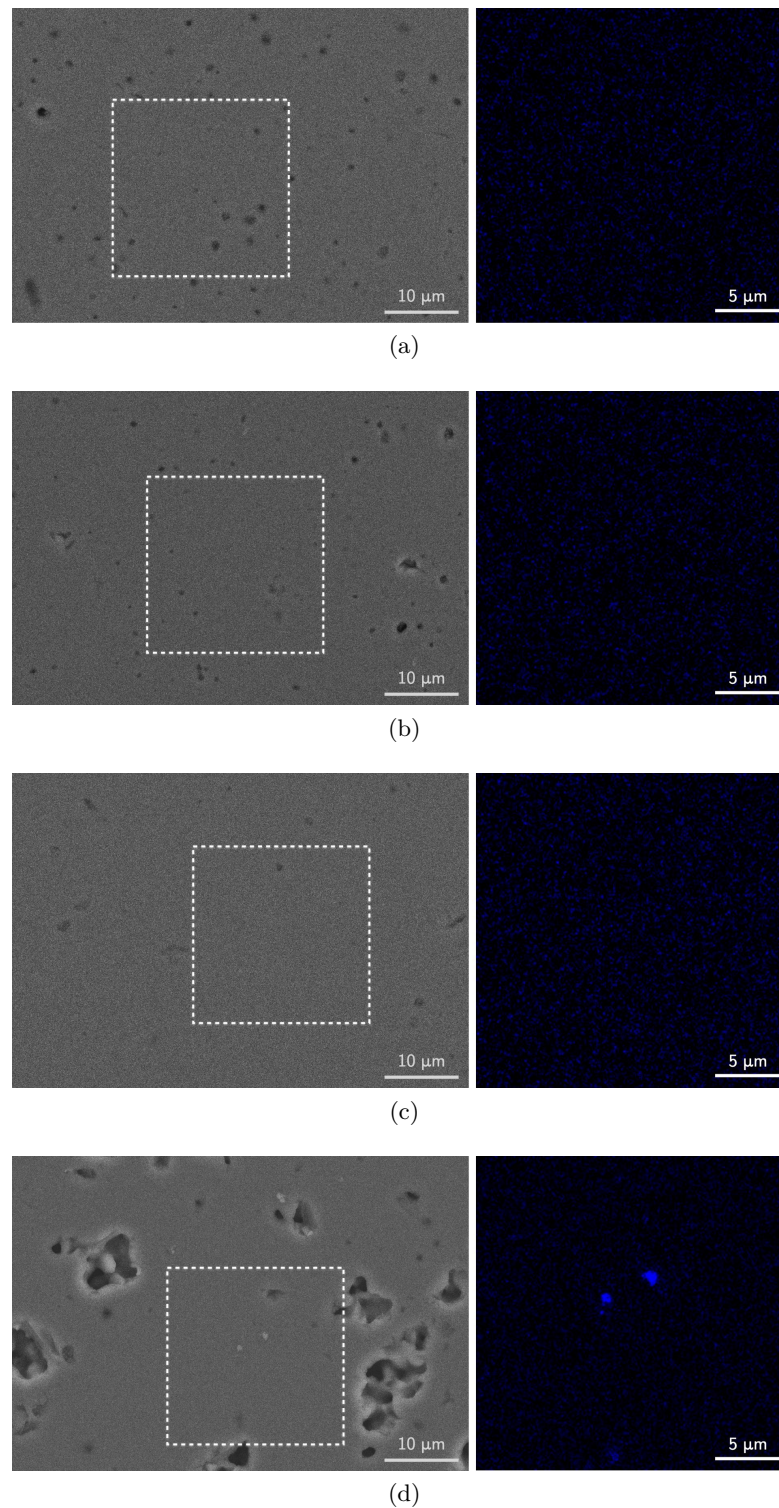
Figure 6.7 – SE-SEM images and EDXS elemental maps integrated from the Cu-Lα series X-ray peak for the (a) 0.10%, (b) 1.00%, (c) 2.92%, and (d) 5.00% Cu-doped β-TCP sectioned and polished samples. Dotted, white squares on the SE-SEM images indicate the mapped regions.
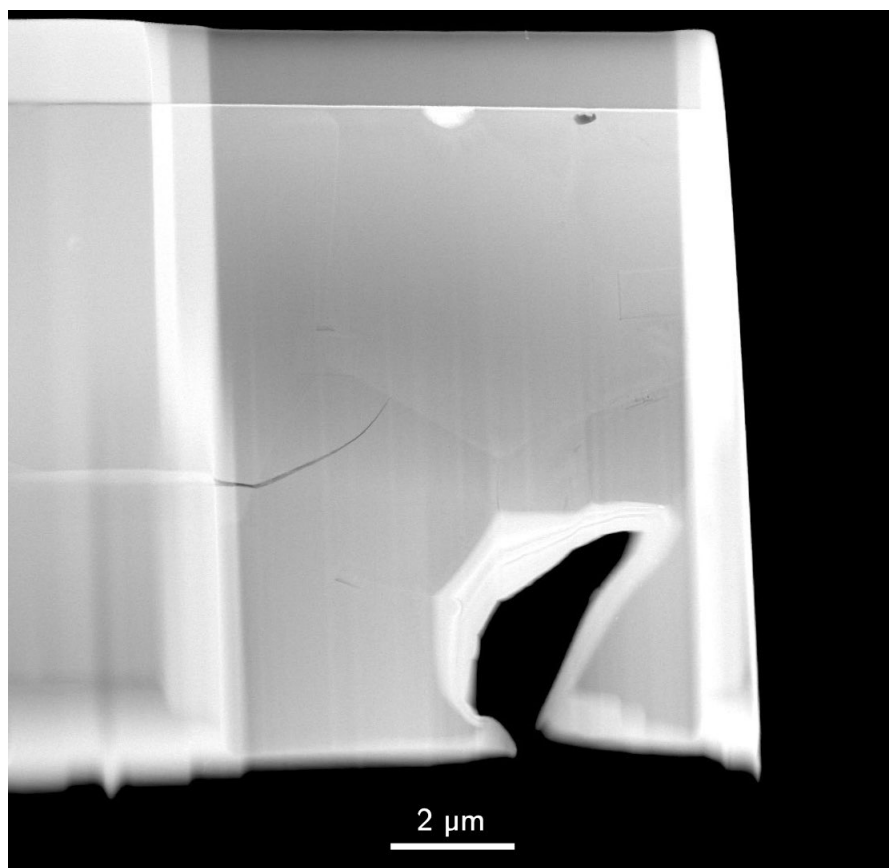
Figure 6.8 – HAADF-STEM overview of the 5.00% Cu-doped β-TCP lamella. The bright inclusion at the top surface of the lamella, just under the deposited carbon protection layer, is the secondary phase that was selected for analysis.

6.2.3   Characterizing the Cu-rich precipitate

The analysis of the secondary phase by STEM-EDXS is now be presented. Characterization was performed with the Tecnai Osiris microscope equipped with four windowless "ChemiSTEM" Super-X SDD EDXS detectors. STEM EDXS maps were acquired around the region of the precipitate. The HAADF-STEM image of the precipitate and the corresponding EDXS elemental maps are shown in Figure 6.9. A depletion of the Ca and P signals are seen within the region of the secondary phase. While the O signal shows no change in signal in the precipitate as compared to the matrix, a much stronger Cu signal is seen in the precipitate.

STEM-EDX spectra, each integrated from a large number of pixel spectra from the precipitate and from the matrix, were calculated in order to compare their elemental compositions. These spectra, shown in Figure 6.10, follow the observations seen in the EDXS maps. The integrated spectra show elements expected in Cu-doped β-TCP: Ca, P, O, and Cu. The Si Kα (1.74 keV) peak is attributed to the Si-half grid. The Ca-Kα,β
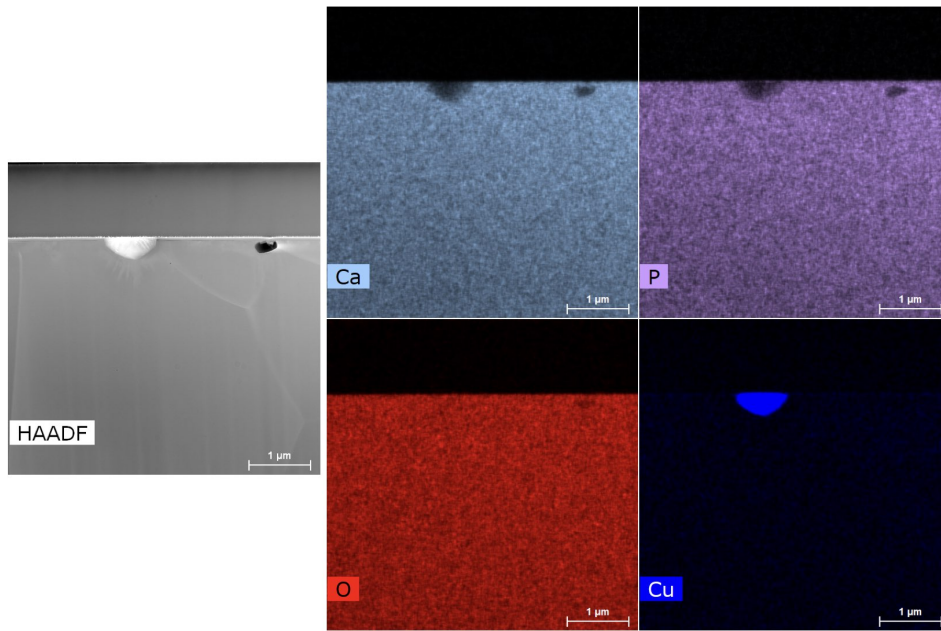
Figure 6.9 – HAADF-STEM image and EDXS elemental maps of a secondary phase precipitate in the 5.00% Cu-doped ceramic: Ca-Kα (3.69 keV), P-Kα (2.01 keV), O-Kα (0.52 keV), and Cu-Kα (8.04 keV).
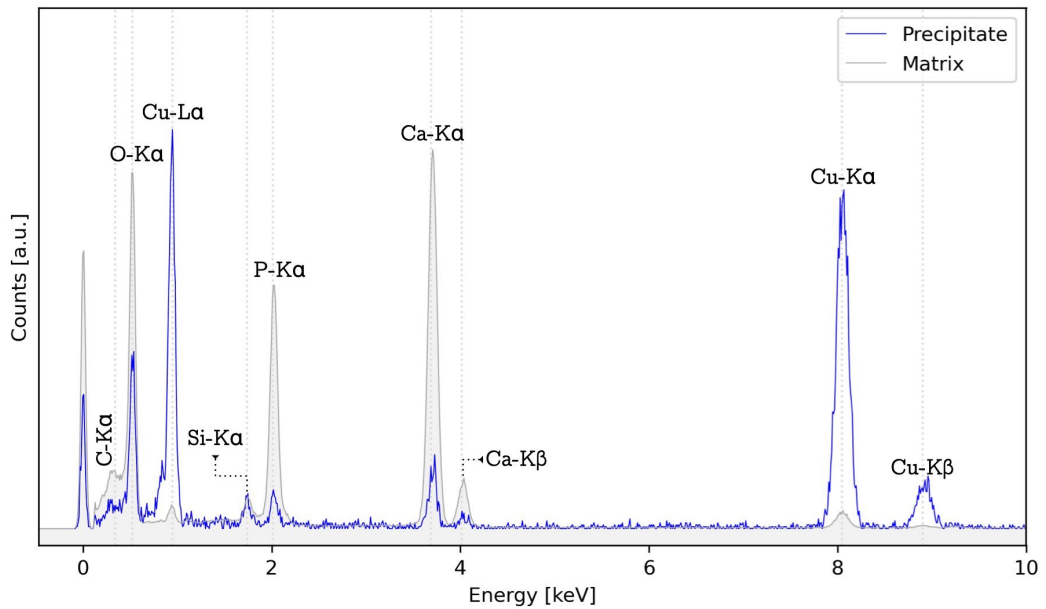
Figure 6.10 – STEM-EDX spectra integrated from regions of the secondary phase precipitate and the matrix, normalized to their total number of counts for easier comparison.
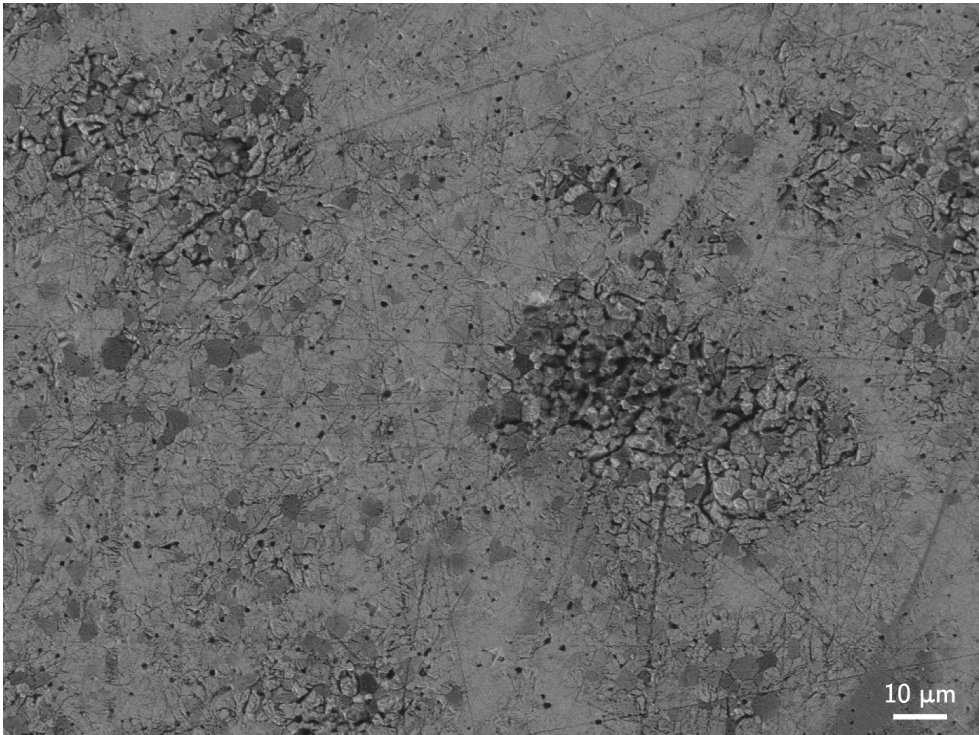
(a)
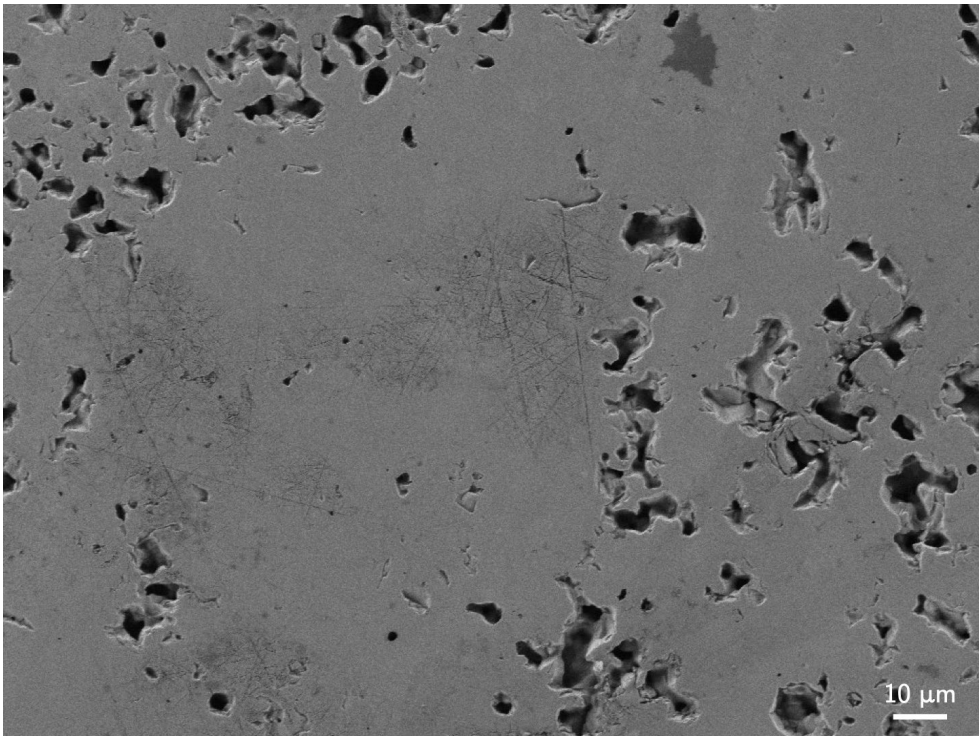
(b)

Figure 6.11 – SE-SEM images of the (a) 0.10% and (b) 5.00% Cu-doped β-TCP polished surfaces after 24 h in cell culture medium with osteoclasts.

and P-Kα signals are stronger in the matrix than in the region of the precipitate. The O-Kα, in addition to the Cu-Kα,β and Cu-Lα signals, are significantly stronger in the precipitate region than in the matrix. These findings suggest that the precipitate is a copper oxide (CuO) phase.

When used as an implant, the presence of a CuO secondary phase could prove to be detrimental to host cells. This is because one could infer that the Cu-rich secondary phase could result in the burst release of Cu^{2+} ions, giving a locally-high concentration of Cu^{2+} ions that is cytotoxic not only to bactericidal cells, but also to host cells. Here, we can further strengthen this inference by correlating these electron microscopy results to the osteoclast resorption tests performed by Le Gars Santoni et al. Figure 6.11 presents two SE-SEM images selected from the catalogue described in Section 6.1. Figure 6.11a shows the image of the surface of a 0.10% Cu-doped β-TCP sample after 24 h of exposure to a cell culture medium containing osteoclasts. The pitted regions correspond to resorption pits created by a healthy osteoclast activity. The outcome of a similar test on a 5.00% Cu-doped β-TCP sample, as shown in Figure 6.11b, is strikingly different. The ceramic surface shows minimal signs of attack and resorption of the osteoclasts. In fact, on this sample, the osteoclast cells were mostly found to be dead by the end of the 24 h test. This can clearly be correlated to the presence of the CuO precipitates in this sample, and the resulting burst releases of Cu^{2+} ions of high cytotoxicity.

6.2.4   Cu distribution across the grain boundaries

The FIB lamella discussed earlier presented clear grain boundaries. This gave us the opportunity to analyze the sample in order to determine the distribution of Cu across the boundaries. In order to prevent too strong an electron beam damage during mapping (see Chapter 3), the multi-frame mapping used acquisition parameters of a pixel size of 1.295 nm and pixel dwell time of 20.0 µs, together with a beam current of ∼0.8 nA. Figure 6.12 shows example elemental maps from a region containing one approximately end-on and two tilted grain boundaries. Across all of them, a uniform distribution of Ca, P, O, and Cu is observed.

Figure 6.13 shows EDXS line profiles across the end-on grain boundary, integrated across a width of 135 nm for increased signal to noise. The profiles for the Ca-Kα, P-Kα, and O-Kα, and Cu-Lα intensities fluctuate uniformly, with relative errors of ±3.0%, ±3.5%, ±2.9%, and ±12.0%, respectively. No significant change is observed outside of these fluctuations. Based on these results, it is concluded that the Cu dopant does not segregate to the grain boundary. Similar to the analysis of the 5.00% Sr-doped β-TCP sample presented in Section 5.4, this conclusion must be considered within the measurement precision allowed by the acquired STEM-EDXS data. Nevertheless, the similar conclusion in both cases can potentially be linked to the ease with which these two dopants can substitute for Ca in the bulk lattice, albeit to a lower preferential limit
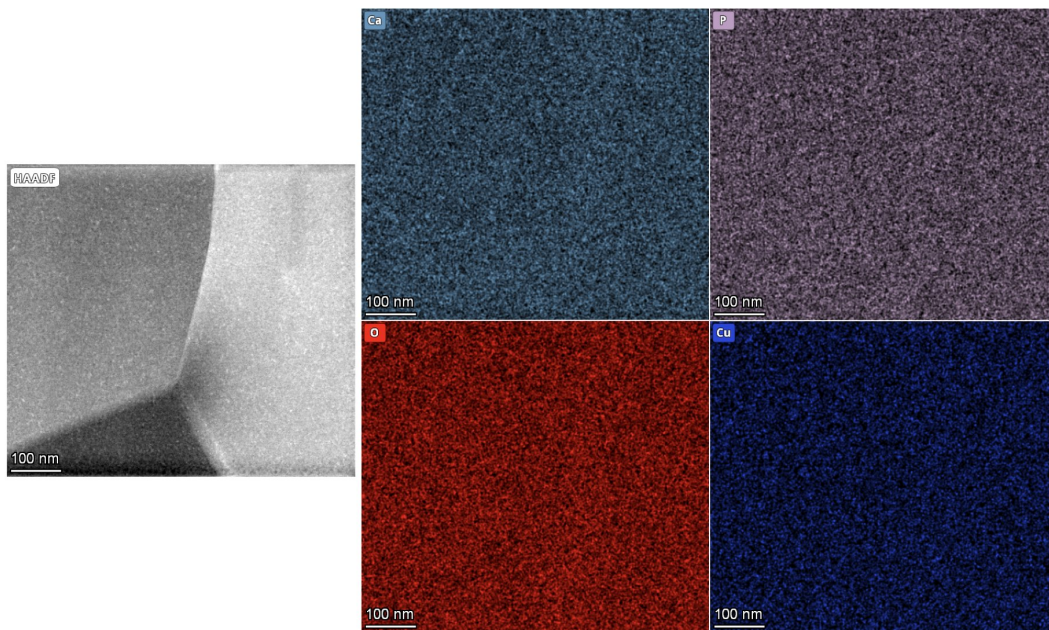
Figure 6.12 – HAADF-STEM image and EDXS elemental maps across grain boundaries in the 5.00% Cu-doped ceramic: Ca-Kα (3.69 keV), P-Kα (2.01 keV), O-Kα (0.52 keV), and Cu-Kα (8.04 keV). The upper, roughly vertical grain boundary is close to end-on.
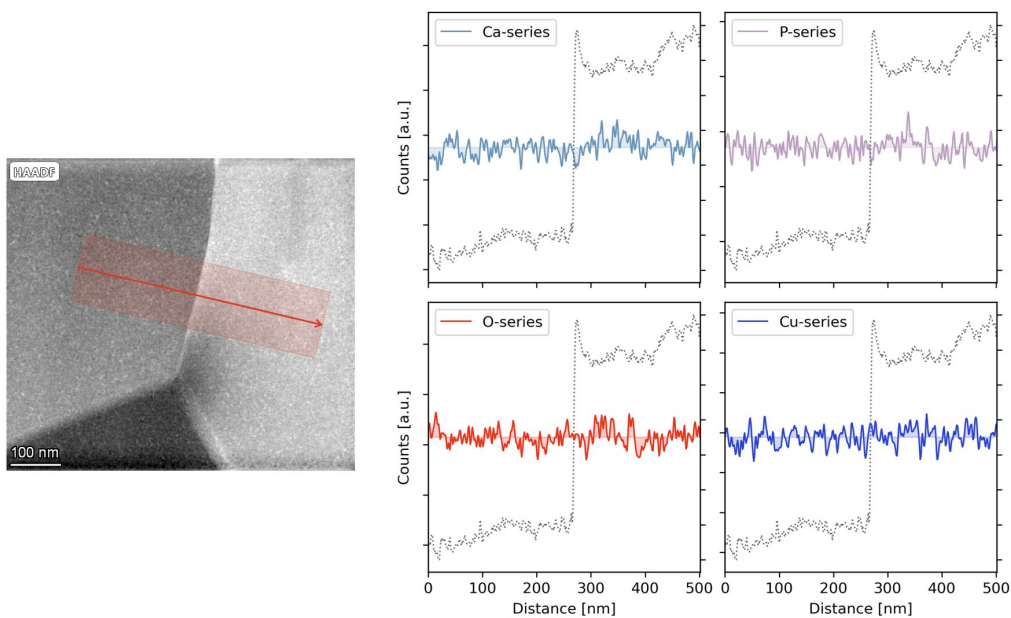
Figure 6.13 – EDXS intensity line profiles across a grain boundary of the 5.00% Cu-doped β-TCP ceramic: Ca-Kα (3.69 keV), P-Kα (2.01 keV), O-Kα (0.52 keV), and Cu-Kα (8.04 keV). The line profile is indicated by the red arrow

in the case of the Cu-doping that leads to the formation of the CuO secondary phase precipitates in the most heavily doped β-TCP ceramic.

6.2.5   Summary of critical findings

The analytical electron microscopy characterization of Cu-doped samples, both by SEM-EDXS and STEM-EDXS, indicates some similarities but also differences relative to the Sr-doping studied in Chapter 5. The similarity comes in the observation of uniform dopant distributions across grain boundaries by STEM-EDXS, within the measurement precision and limited number of sampled grain boundaries. However, while the large Sr^{2+} ion preferentially substitutes into the most spacious Ca^{2+} sites, and can substitute up to 80% of the Ca ions in the β-TCP lattice, the small Cu^{2+} ions preferentially replace Ca^{2+} ions in the most tightly-caged sites. Further, even going from 2.92% to 5.00% doping induces the formation of secondary CuO precipitates, implying a much lower limit to substitution into the lattice. These secondary precipitates prove catastrophic for the biocompatibility of the ceramic. While a low level of Cu-dopants may provide some useful cytotoxicity to prevent bacterial infections, it appears that burst release of Cu^{2+} ions from the precipitates can kill "friendly" cells such as osteoclasts.

7 Summary & Outlook

In this thesis, we explored the following themes: obtaining a better understanding of the β-TCP crystal structure; developing and applying a first approach to simulating doped β-TCP interfaces; relating these results to experimentally characterized β-TCP samples. This has been achieved by applying a combination of atomistic scale simulations and analytical electron microscopy techniques. Significant progress has been made on all fronts, even if definitive and/or quantitative conclusions are still difficult to reach. The first steps and parameter exploration have already given several interesting insights that paves the pathway towards stimulating future work — which in turn will lead towards the design of better β-TCP ceramics for biomedical applications.

7.1 Further understanding of the β-TCP crystal structure

The first objective explored was to improve the understanding of the β-TCP crystal structure, as it remains incommensurate with diffraction analyses. This suggests that the Ca(4) site occupancy is neither fully random, nor fully ordered, on the scale of the single unit cell. Atomistic simulations were performed to gain insights on the complicated nature of the Ca(4) site occupancy in the β-TCP crystal structure. From previous literature, a Ca(4) site occupancy of 50% was assumed for the overall studies.

The Ca(4) site was first considered on the level of the β-TCP unit cell. This shows that, at 50% occupancy, the β-TCP unit cell presents twenty possible variations of Ca(4) site occupancy. Exploration of the β-TCP unit cell using molecular dynamics (MD) simulations found that the twenty configurations could be grouped into three energetic classes: the low (LEC, $n = 2$), intermediate (IEC, $n = 12$), and high (HEC, $n = 6$) energy configurations. While these simulations are fully consistent with other computational studies and identify the LEC to be the most favorable on the level of the single unit cell, this does not in itself explain the mystery of the Ca(4) site. The Ca(4) site as arranged in the LEC would be identified by diffraction studies, since the defined periodicity would be described by an alternative unit cell with different symmetry.

Therefore, I investigated the β-TCP unit cell over larger length scales, first by MD equilibrating systems that "patched" together combinations of the twenty β-TCP unit cell variations. Even within the limited sample size investigated for these "patched" systems, numerous configurations that combined LEC, IEC, and HEC unit cells were identified to be as energetically stable as the supercell system composed solely of LECs. This implies that a single unit cell definition is an inaccurate description of the Ca(4) site in the β-TCP crystal structure.

I then set out on a new approach, guided by a new perspective of the β-TCP unit cell. Stimulated by recent experimental findings, supercell systems were explored that preserved the 50% partial occupancy on the global scale by: (1) constructing 3D-checkerboard arrangements of the Ca(4) site by considering unit cells that each have variable Ca(4) site occupancy, and (2) exploring long range supercell systems by Monte Carlo (MC) simulations that fully removed pre-existing constraints of the checkerboard model. The 3D-checkerboard simulations showed that deviations from a 50% cell-by-cell Ca(4) site occupancy can lead to an energetic stabilization of the supercell. Moreover, in the energetic-structural parameter space, defined regions of energetic stability were found having different lattice parameters which might reflect an experimentally-observed lattice parameter discontinuity. These defined regions had characteristic arrangements of Ca(4) site occupancy.

While interesting, it was not clear whether this was a by-product of repetitions defined by the patchwork supercells. The MC simulations allowed such a constraint to be

released, while also releasing the constraint of 50% cell-by-cell Ca(4) site occupancy. The MC results, using large supercells, showed the presence of seven unit cell types having a range of Ca(4) site occupancies going from zero to fully occupied. These seven unit cells are represented in a manner that mirrors the number of possible unit cell combinations, which must be linked to the configurational entropy. In an effort to understand if and how these domains had any underlying order, I developed tools to study potential long-range ordering of the Ca(4) sites. However, no long-range ordering or patterning of the MC simulations were observable with the tools developed. Rather, it appears that the Ca^{2+} ions are randomly arranged on the available Ca(4) sites, but on the scale of the supercell, rather than the traditionally-assumed scale of the individual unit cell.

Outlook. For the moment, the core challenge with probing longer range ordering is being able to appropriately segment the structures such that the Ca(4) site occupancy can be interpreted. Further analysis that can be pursued includes: evaluating if there is either a repeating pattern of the Ca(4) site occupancy that extends beyond the dimensions of the simulation box, or that the Ca(4) site occupancy is pseudo-random (i.e. random on the scale of the supercell); verification of the lack of localized regions of ordered site occupancy within a supercell. In addition to the development of a suitable metric or algorithm to identify local or large scale Ca(4) site occupancy patterning, another possible avenue for future studies is the acquisition of, and correlation to, experimental pair distribution function (PDF) data from total scattering experiments acquired using synchrotron radiation.

7.2   A first approach to simulating doped β-TCP interfaces

With these insights from Chapter 4 about the Ca(4) site occupancy kept in mind, I developed a framework for studying dopant incorporation at β-TCP interfaces in Chapter 5. This was done for the case of Sr-doped β-TCP as a model system for a resorbable bone substitute with possible beneficial properties in application. The framework used energy minimization (EM) and Monte Carlo (MC) simulations with validated potentials for Sr^{2+} in β-TCP to give the following results:

- Potentials developed for hydroxyapatite (HA) can be applied to other calcium phosphate systems, including β-TCP.

- A 'reduced' β-TCP unit cell can be appropriately used to create the interface structures in order to create reasonably sized simulation boxes for Monte Carlo simulations.

- Insights about the Ca(4) site occupancy were integrated into the framework. Except for the low Sr-content surfaces ($< 2\%$), the chosen Ca(4) site occupancy had no significant impact on the dopant behavior in the interface structures. Therefore, the occupied Ca(4) sites can be selected randomly in layers perpendicular to the interface in order to avoid the formation of dipoles within the solid slab, and simulating one interface structure is normally sufficient.

With the framework developed, the first reported interface energies (γ) and segregation enthalpies (ΔH_{seg}) for $(1\,\overline{2}\,0)$ and $(1\,0\,0)$ systems were presented. The results of these simulations show different segregation tendencies between the $(1\,\overline{2}\,0)$ and $(1\,0\,0)$ grain boundaries: a pronounced segregation of Sr^{2+} is expected at the $(1\,0\,0)$ grain boundary at low Sr content, while limited or no segregation of Sr^{2+} is expected to the $(1\,\overline{2}\,0)$ grain boundary. Also, the relative degree of segregation was concentration dependent, actually decreasing as total dopant concentration increases. Overall, these preliminary results therefore suggest that Sr-segregation can be expected at certain "special" β-TCP grain boundaries, but perhaps not others, and that the strength of segregation could depend critically on the absolute amount of dopant.

Outlook. Currently five other surfaces and grain boundaries are being simulated to see how they compare to the two presented in the thesis. These have all been shown to be possible crystal surfaces of interest in different experimental approaches. This will allow further insight into Sr^{2+} segregation to be gained and perhaps help guide further experimental approaches that, as discussed below, have been found to have certain challenges. The general framework can be used for other dopant systems and the use of Monte Carlo methods for such grain boundary investigations show great potential.

7.3 Analytical electron microscopy of ion-doped β-TCP samples

First studies were made to characterize dopant behavior across grain boundaries in sintered, ion-doped β-TCP samples using STEM-EDXS, in an effort to make correlations between experiments and atomistic simulations. Measurements were made on samples prepared by FIB, which include: 5.00% Sr-doped, 5.00% Cu-doped ceramics, along with a ceramic prepared from a commercial powder containing low levels of Sr, Na and Mg as impurities. No segregation behavior was observed at the grain boundaries of either of the well-controlled 5.00% ion-doped samples. In comparison, while Mg was similarly found to be uniformly distributed in the commercial-impurity sample, there was insufficient X-ray signal from the low levels of Sr and Na dopants (each $\sim$300 ppm) such that no information could be concluded about their distributions. While no particular behavior of dopants across grain boundaries was seen for the 5.00% Cu-doped β-TCP, importantly this sample was found to contain CuO precipitates that are concluded to give a strong cytotoxicity to osteoclasts that was observed during *in vitro* tests.

Outlook. The STEM-EDXS technique presents certain limitations to elemental mapping measurement precision and sensitivity, owing in large part to degradation of the beam-sensitive samples during data acquisition. While grain boundary dopant segregation of the degree found for simulation of the (1 0 0), 5.00% Sr-doped sample should be near-definitively measurable with the acquisition parameters applied, this may not be true for more subtle fluctuations. Furthermore, it is impossible to measure dopants at very low levels. In order to adequately address simulation-experiment correlations, various avenues are therefore suggested. Firstly, the effect of the limited size of the simulation box ($\sim$10 nm) on segregation behavior, as compared to the size of grains ($\sim$1–2 μm), should be explored and verified, for instance to see if expected segregation maintains or reduces its level as the box size is increased. Secondly, as already planned, more grain boundary configurations should be simulated, in order to obtain an idea of what fraction of boundaries are expected to show segregation, and then compare to a greater number of experimentally-measured boundaries. Thirdly, with the first grain boundary simulations suggesting that the lower dopant contents may be associated with greater relative dopant segregation to grain boundaries, and given preliminary atom probe tomography results, correlated TEM and atom probe tomography is suggested as a more suitable experimental strategy for investigating grain boundary dopant segregation.

7.4 Scanning electron microscopy documentation of synthesized samples and cell culture tests

A significant experimental part of this thesis was the SEM imaging and documentation of β-TCP samples during various stages of their synthesis, and sintered ceramics after cell culture test, working in close collaboration with Dr. Bastien Le Gars Santoni, who was the other PhD student engaged in the Sinterphos project. In this work, suitable sample preparation protocols and image acquisition parameters had to first be developed for the different types of samples. Then, a cataloguing effort resulted in the documentation of $\sim$224 samples, over the course of two years.

Outlook. So far, the image data recorded in this endeavor have contributed to the scientific development and figures for three peer-reviewed journal publications, with two also in preparation. The parameters developed for acquiring the high-quality images can also be applied by future researchers working on similar bioceramic systems. Finally, in order for other researchers to fully leverage the potential of this catalogued data-set, the complete electron microscopy documentation linked to the project will be provided in an online repository in the future.

A Simulation Files

A.1 LAMMPS

The LAMMPS program was used to run molecular dynamics simulations in this thesis. The program runs from an `input.in` file from which a series of actions are defined. These actions can include: (1) commands that set global variables, (2) modifying commands that are executed during the "run", and (3) commands that perform other operations. Listing A.1 shows the structure of a LAMMPS input script used to run an undoped β-TCP crystal structure.

Listing A.1 – An example LAMMPS input script

```
1  # BASIC SETTINGS
2  units   metal
3  atom_style   full
4  boundary   p p p
5  timestep   0.005
6  neighbor   1.0 bin
7  neigh_modify   delay 0 every 10 check yes
8
9  # ATOM CREATION
10 read_data data.data
11 replicate 3 3 1
12
13 # BONDED FORCE FIELD
14 bond_style harmonic
15 bond_coeff 1 15.831 1.5946
16 angle_style class2
17 angle_coeff 1 109.5 8.9168 0.0 0.0
18 angle_coeff 1 bb 2.5983 1.5946 1.5946
19 angle_coeff 1 ba 3.0 3.0 1.5946 1.5946
20
21 # NONBONDED FORCE FIELD
22 pair_style hybrid/overlay buck/coul/long 13.0 buck 13.0
23 pair_coeff * * buck/coul/long 0.00 1.00 0.00
24 pair_coeff 1 2 buck/coul/long 2132.9786 0.342800 0.00 # Ca-P
```

```
25 pair_coeff 1 3 buck/coul/long 2510.8780 0.276289 0.00 # Ca-O
26 pair_coeff 3 3 buck 12534.455 0.202000 0.00 # O-O
27 pair_modify tail yes
28 kspace_style ewald 1e-5
29
30 # OUTPUT CONTROL
31 thermo_style      custom step time temp press etotal pe ke enthalpy cella
      cellb cellc cellalpha cellbeta cellgamma vol density
32 thermo            1000
33
34 # RELAX BOX
35 fix          1 all box/relax tri 0.0 vmax 0.001
36 minimize     1.0e-4 1.0e-6 100 1000
37 unfix        1
38
39 # HEATING THE SYSTEM
40 fix 2 all nvt temp 300.0 300.0 0.9
41 fix 3 all temp/rescale 1 0.0 300.0 0.05 1.0
42 run 1000000
43 unfix 2
44 unfix 3
45
46 # BAROSTAT
47 fix 4 all npt temp 300.0 300.0 0.9 tri 27271.421 1.0 9.0
48 run 1000000
49 unfix 4
50
51 # EQUILIB
52 fix 5 all npt temp 300.0 300.0 0.9 tri 1.0 1.0 9.0
53 run 2000000
54 unfix 5
55
56 # DATA PROD REGION
57 fix 5 all npt temp 300.0 300.0 0.9 tri 1.0 1.0 9.0
58 run 2000000
59 unfix 5
```

Listing A.1 can be customized in a number of ways. Within the context of the thesis, the listed `Bonded Force Field` and `Nonbonded Force Field` is appropriately chosen for the system of interest. The force field in Listing A.1 is the reported force field by Demichellis et al. [30] for calcium phosphate systems. For the Sr-substitution study in Chapter 5, the `Sr-O` and `Sr-P` interactions are added to the `Nonbonded Force Field` section of the input script.

The second typical modification of the input script is within the `data.data` file that is read in from Line 10 of Listing A.1. The structure of the `data.data` file is presented in Listing A.2. This example is set-up for reading the data of a single β-TCP unit cell with 50% of the Ca(4) sites defined. As the `replicate 3 3 1` command is called in Line 11 of Listing A.1, extra care must be taken in defining the image flags

(`dx dy dz`) in the `Atoms # full` section of Listing A.2 to ensure the bonded species are simulated correctly.A tutorial for creating LAMMPS data files can be found in the technical post "Python For Scientists And Researchers: Solving Common Problems".

Listing A.2 – Structure of a LAMMPS data file

```
1  # LAMMPS data input file via convert-vasp-to-data script
2
3  273 atoms
4  3 atom types
5  168 bonds
6  1 bond types
7  252 angles
8  1 angle types
9
10  0.0000000000 10.4351997375 xlo xhi
11  0.0000000000  9.0371480663 ylo yhi
12  0.0000000000 37.4029006958 zlo zhi
13 -5.2175998687  0.0000000000  0.0000000000 xy xz yz
14
15 Masses
16
17 1 40.0780
18 2 30.9738
19 3 15.9950
20
21 Atoms # full
22 # Format: index molid atomid charge x y z dx dy dz
23
24 Bonds
25 # Format: index id atom_i atom_j
26
27 Angles
28 # Format: index id atom_i atom_j atom_k
```

A.2   DL_MONTE

The DL_MONTE program was used to run Monte Carlo simulations in this thesis. The program requires three input files to run correctly: (1) CONFIG, (2) FIELD, and (3) CONTROL. In this section, the files used for simulating doped β-TCP systems (Chapter 5) are presented as examples.

The CONFIG file contains details of the simulation configuration, such as the dimensions of the simulation box and the atoms present. In the following cell block, the atomic coordinates for each Ca^{2+} and Sr^{2+} ions are collected in their respective `MOLECULE` sections. As the phosphate tetrahedra are considered rigid bodies in the Monte Carlo simulations of this thesis, each phosphate group must have its own `MOLECULE` section.

Listing A.3 – The DL__MONTE CONFIG file template for a Sr-doped β-TCP system.

```
1  5.0% Sr: ./surf/surf-1_0_0.CONFIG
2  0       1
3     20.5698761514    0.0000000000    0.0000000000
4     0.0000000000    18.6483028915    0.0000000000
5     0.0000000000     0.0000000000   143.0000000000
6  NUMMOL 338 1 1 336
7  MOLECULE Calcium 479 479
8  Ca core
9     -8.4337846356    -3.7695286552    -34.9829625957
10          .
11          .
12          .
13 MOLECULE Strontium 25 25
14 Sr core
15    -7.6804791318     3.7333352358    -34.5153280850
16          .
17          .
18          .
19 MOLECULE Phosphate 5 5
20 P core
21    -0.6074177945     5.0418404846     8.0759725469
22 O core
23     0.6510941950     4.5729814386     7.3211767094
24 O core
25    -0.8944883289     6.5161173168     7.7140064235
26 O core
27    -1.9299401261     4.3008092376     7.7507097258
28 O core
29    -0.3869446431     4.7900579929     9.5868798606
```

The FIELD file provides information on the implemented force field. In this example, It is within this file that the phosphate groups labelled in Listing A.3 are defined to be rigid-bodies with the `RIGID` command called in Line 22. The force field implemented in the `VDW 6 ecap 1.0E10` section is the combined force field presented in Section 5.1.

Listing A.4 – An example FIELD file for DL__MONTE

```
1  bTCP with Sr-dopants
2  CUTOFF 13.0  # cut-off radius (must be the 2nd line - after the title)
3  UNITS eV  # energy unit (must be the 3rd line - after CUTOFF)
4  NCONFIGS 1  # number of configs in CONFIG file (must be the 4th line)
5  ATOM TYPES 4  # number of atom types or 'elements' (must be the 5th line)
6  Ca core  40.078  2.0000 # mass and charge of Ca
7  P  core  30.973  0.9700 # mass and charge of P
8  O  core  15.999 -0.9925 # mass and charge of O
9  Sr core  87.621  2.0000 # mass and charge of Sr
10 MOL TYPES 3 # number of molecular types
11 Calcium
12 MAXATOM 1007
13 Strontium
```

```
14  MAXATOM 1
15  Phosphate
16  ATOMS 5 5
17  P   core    0.00000000    0.00000000    0.00000000
18  O   core   -0.43013382   -1.24351102   -0.77742304
19  O   core   -0.43013382   -0.05151063    1.46562375
20  O   core   -0.43013382    1.29502332   -0.68820137
21  O   core    1.57466316    0.00000000    0.00000000
22  RIGID
23  EXCLUDE
24  FINISH
25  FINISH
26  VDW 6 ecap 1.0E10   # non-bonded VdW section
27  Ca core   P core    buck     2132.9786 0.342800 0.00
28  Ca core   O core    buck     2510.8780 0.276289 0.00
29  O core    O core    buck    12534.4550 0.202000 0.00
30  Sr core   P core    buck     1405.4387 0.387208 0.00
31  Sr core   O core    buck     1654.4400 0.312081 0.00
32  P core O core       12-6     1000.0000 0.00 0.00
33  CLOSE   # closing FIELD
```

Lastly, the CONTROL file defines the simulation parameters, such as the thermodynamic conditions, statistical ensemble, sampling schemes, output frequencies, etc.

Listing A.5 – An example FIELD file for DL_MONTE

```
1   5.0% Sr: SURF-100-2.CONFIG. bTCP with Sr in surface structure
2
3   # 'USE' SECTION
4   use orthogonal
5   finish
6
7   ranseed
8
9   # THERMODYNAMIC CONDITIONS
10  temperature   1400.0   # T *= 1.1876; T (in K) = T*/BOLTZMAN
11
12  # TECHNICAL SPECS
13  nbrlist auto   # Use a neighbour list to speed up energy calculations
14  maxnonbondnbrs 1000   # Maximum number of neighbours in neighbour list
15
16  steps   22000000   # Number of MC moves to perform in the simulation
17
18  # SAMPLING FREQUENCY
19  print   1000000
20  stat   1000000
21  check   300000
22  sample coords 22000
23  yamldata   2200
24
25  # SIMULATION OUTPUT
26  revconformat   dlpoly4
```

```
27  archiveformat dlpoly4
28
29  # MONTE CARLO MOVES
30  move atom 2 1400
31  Ca core
32  Sr core
33
34  move molecule 1 800
35  Phosphate
36
37  move rotatemol 1 800
38  Phosphate
39
40  move swapatoms 1 600
41  Ca core    Sr core
42
43  move volume orthoani 1
44
45  start
```

A.3   METADISE

The METADISE program was used to create β-TCP interface structures. The program uses an `poten.txt` and `input.txt` file to run successfully. Here we present the commands used to create the structures presented in Chapter 5.

A.3.1   Potential field file

The `poten.txt` file below is the file used to define the potentials reported by Jay et al. [34] for a core-shell model of β-TCP. This file is used with all other input files associated with METADISE.

```
1   # b-TCP potential set (Jay et al.)
2   potential
3     species
4       ca   core +2.000
5       ca_f  core +1.000
6       p   core +1.180
7       o   core +0.587
8       o   shell -1.632
9     ends
10
11  buck
12    ca core    o shell 1550.00   0.2970   0.00 0.0 13.0
13    ca_f core o shell 1540.00   0.269355   0.00 0.0 13.0
14    o   shell  o shell 16372.0   0.2130   3.47 0.0 13.0
15  ends
16
```

```
17 harm    o   core o   shell 1114.8
18
19 mors
20   p   core o   core   3.47 2.03 1.60   0.0 1.6
21 ends
22
23 boha    1 1.322626 109.47
24 ends
```

A.3.2   The 'reduced' β-TCP unit cell

A 'reduced' form of the β-TCP unit cell was the chosen crystallographic representation for creating interface structures. This structure is catalogued in the Crystallography Open Database as entry number 1517238.

The structure treated by splitting the cell across the c-axis. The Ca(4) sites of the 'reduced' structure must be identified (Ca_F) to preserve the six Ca(4) sites of the original unit cell. Because a core-shell potential form is used in File A.3.1, the oxygen coordinates are duplicated to have an O CORE and O SHELL component.

The following shows the coordinate structure of the 'reduced' β-TCP unit cell in METADISE:

```
CA CORE 3.0783839230 7.7882146840 6.2201023100      CA CORE 5.0934214590 5.4831390380 14.7529516220
CA CORE -3.0663836000 7.8090000150 6.2201023100      CA CORE 0.1241789910 8.4955224990 8.5191335680
CA CORE -0.0120002850 2.4770824910 6.2201023100      CA CORE 2.0776486400 4.6818451880 8.5191335680
CA CORE 3.0783841610 1.7634488340 18.6877365110      CA CORE -2.2018275260 4.8969292640 8.5191335680
CA CORE 7.3688168530 1.7842342850 18.6877365110      CA CORE 0.0000000000 0.0000000000 8.7373180390
CA CORE 5.2055997850 5.4894652370 18.6877365110      CA CORE 5.2175998690 3.0123829840 2.5035030840
CA CORE 0.0119999780 8.5018482210 12.4539194110      CA CORE -0.0000000240 6.0247659680 14.9711332320
CA CORE 2.1392161850 4.7758321760 12.4539194110      P CORE 0.0000000000 0.0000000000 0.0000000000
CA CORE -2.1512167450 4.7966170310 12.4539194110      P CORE 5.2175998690 3.0123829840 12.4676342010
CA CORE -0.1680068670 3.4449610710 17.4596748350      P CORE -0.0000000240 6.0247659680 6.2338171010
CA CORE -2.1501727100 7.4601659770 17.4596748350      P CORE -0.1773983390 2.8268198970 13.7829685210
CA CORE 2.3181798460 7.1691694260 17.4596748350      P CORE -2.6808028220 7.7773699760 13.7829685210
CA CORE 2.1501724720 1.4354008440 11.2258577350      P CORE 2.8582010270 7.4701070790 13.7829685210
CA CORE 8.1170206070 1.1444040540 11.2258577350      P CORE 2.6808028220 1.7526046040 7.5491533280
CA CORE 5.3856072430 6.4573435780 11.2258577350      P CORE 7.5769982340 1.4453414680 7.5491533280
CA CORE 5.0495934490 0.4325785040 4.9920406340      P CORE 5.3949990270 5.8392024040 7.5491533280
CA CORE 3.0674266820 4.4477839470 4.9920406340      P CORE -0.1773978770 8.8515853880 1.3153336050
CA CORE 7.5357794760 4.1567869190 4.9920406340      P CORE 2.5367963310 4.7649879460 1.3153336050
CA CORE 3.1399517060 7.6942281720 2.2853171830      P CORE -2.3593988420 4.4577245710 1.3153336050
CA CORE -3.0157728200 7.9093122480 2.2853171830      P CORE -0.2076606600 3.1358904840 9.9790906910
CA CORE -0.1241786410 2.4707565310 2.2853171830      P CORE -2.3980085850 7.6490426060 9.9790906910
CA CORE 3.1399517060 1.6694630380 14.7529516220      P CORE 2.6056697370 7.2893638610 9.9790906910
CA CORE 7.4194269180 1.8845465180 14.7529516220      P CORE 2.3980081080 1.6242773530 3.7452759740
```

```
P CORE 7.8295307160 1.2645981310 3.7452759740        O SHELL 3.8537194730 6.5157837870 13.0386476520
P CORE 5.4252605440 6.1482739450 3.7452759740        O CORE 2.3520944120 3.0919098850 6.8048324580
P CORE 7.6156082150 4.6366605760 16.2129116060       O SHELL 2.3520944120 3.0919098850 6.8048324580
P CORE 2.6119308470 4.2769808770 16.2129116060       O CORE 6.5814809800 0.4910183550 6.8048324580
P CORE 5.4252610210 0.1235079020 16.2129116060       O SHELL 6.5814809800 0.4910183550 6.8048324580
O CORE -0.4466265140 2.4797935490 15.2716035840      O CORE 6.7192254070 5.4542207720 6.8048324580
O SHELL -0.4466265140 2.4797935490 15.2716035840     O SHELL 6.7192254070 5.4542207720 6.8048324580
O CORE -2.8467223640 8.1840419770 15.2716035840      O CORE -1.5016254190 8.4666032790 0.5710172650
O SHELL -2.8467223640 8.1840419770 15.2716035840     O SHELL -1.5016254190 8.4666032790 0.5710172650
O CORE 3.2933492660 7.4104619030 15.2716035840       O CORE 2.8655068870 6.1042923930 0.5710172650
O SHELL 3.2933492660 7.4104619030 15.2716035840      O SHELL 2.8655068870 6.1042923930 0.5710172650
O CORE 2.8467233180 2.1592760090 9.0377874370         O CORE -1.3638805150 3.5034015180 0.5710172650
O SHELL 2.8467233180 2.1592760090 9.0377874370        O SHELL -1.3638805150 3.5034015180 0.5710172650
O CORE 7.1418509480 1.3856958150 9.0377874370         O CORE 0.0026085860 4.3188533780 13.5660314560
O SHELL 7.1418509480 1.3856958150 9.0377874370        O SHELL 0.0026085860 4.3188533780 13.5660314560
O CORE 5.6642270090 5.4921765330 9.0377874370         O CORE -1.4786676170 6.8754625320 13.5660314560
O SHELL 5.6642270090 5.4921765330 9.0377874370        O SHELL -1.4786676170 6.8754625320 13.5660314560
O CORE -0.4466265440 8.5045595170 2.8039708140        O CORE 1.4760587220 6.8799810410 13.5660314560
O SHELL -0.4466265440 8.5045595170 2.8039708140       O SHELL 1.4760587220 6.8799810410 13.5660314560
O CORE 2.3708770280 5.1716589930 2.8039708140         O CORE 1.4786680940 0.8506972790 7.3322162630
O SHELL 2.3708770280 5.1716589930 2.8039708140        O SHELL 1.4786680940 0.8506972790 7.3322162630
O CORE -1.9242503640 4.3980789180 2.8039708140        O CORE 8.9591407780 0.8552153110 7.3322162630
O SHELL -1.9242503640 4.3980789180 2.8039708140       O SHELL 8.9591407780 0.8552153110 7.3322162630
O CORE 1.0476943250 2.1020405290 13.2705488200        O CORE 5.2149910930 7.3312368390 7.3322162630
O SHELL 1.0476943250 2.1020405290 13.2705488200       O SHELL 5.2149910930 7.3312368390 7.3322162630
O CORE -3.9210267070 7.0787982940 13.2705488200       O CORE 5.2202091220 1.3064708710 1.0983965400
O SHELL -3.9210267070 7.0787982940 13.2705488200      O SHELL 5.2202091220 1.3064708710 1.0983965400
O CORE 2.8733325000 8.8934583660 13.2705488200        O CORE 3.7389328480 3.8630793090 1.0983965400
O SHELL 2.8733325000 8.8934583660 13.2705488200       O SHELL 3.7389328480 3.8630793090 1.0983965400
O CORE 3.9210276600 1.0540324450 7.0367331500         O CORE 6.6936588290 3.8675982950 1.0983965400
O SHELL 3.9210276600 1.0540324450 7.0367331500        O SHELL 6.6936588290 3.8675982950 1.0983965400
O CORE 7.5618677140 2.8686926360 7.0367331500         O CORE -1.5845850710 3.6266078950 10.4503698350
O SHELL 7.5618677140 2.8686926360 7.0367331500        O SHELL -1.5845850710 3.6266078950 10.4503698350
O CORE 4.1699056630 5.1144237520 7.0367331500         O CORE -1.2845728400 8.5961360930 10.4503698350
O SHELL 4.1699056630 5.1144237520 7.0367331500        O SHELL -1.2845728400 8.5961360930 10.4503698350
O CORE 1.0476938490 8.1268062590 0.8029136060         O CORE 2.8691580300 5.8515534400 10.4503698350
O SHELL 1.0476938490 8.1268062590 0.8029136060        O SHELL 2.8691580300 5.8515534400 10.4503698350
O CORE 1.2965732810 4.0664157870 0.8029136060         O CORE 1.2845730780 2.5713701250 4.2165546420
O SHELL 1.2965732810 4.0664157870 0.8029136060        O SHELL 1.2845730780 2.5713701250 4.2165546420
O CORE -2.3442673680 5.8810753820 0.8029136060        O CORE 2.3484420780 8.8639364240 4.2165546420
O SHELL -2.3442673680 5.8810753820 0.8029136060       O SHELL 2.3484420780 8.8639364240 4.2165546420
O CORE 8.9335737230 2.4418375490 13.0386476520        O CORE -3.6330144410 6.6389904020 4.2165546420
O SHELL 8.9335737230 2.4418375490 13.0386476520       O SHELL -3.6330144410 6.6389904020 4.2165546420
O CORE 2.8655064110 0.0795269090 13.0386476520        O CORE 6.5021729470 5.5837531090 16.6841850280
O SHELL 2.8655064110 0.0795269090 13.0386476520       O SHELL 6.5021729470 5.5837531090 16.6841850280
O CORE 3.8537194730 6.5157837870 13.0386476520        O CORE 2.3484418390 2.8391706940 16.6841850280
```

```
O SHELL 2.3484418390 2.8391706940 16.6841850280      O SHELL -2.2863523960 7.4628772740 8.4829769130
O CORE 6.8021850590 0.6142251490 16.6841850280       O CORE 2.3886172770 7.2857494350 8.4829769130
O SHELL 6.8021850590 0.6142251490 16.6841850280      O SHELL 2.3886172770 7.2857494350 8.4829769130
O CORE 0.9798651930 3.8516323570 10.6598300930        O CORE 2.2863528730 1.4381114240 2.2491612430
O SHELL 0.9798651930 3.8516323570 10.6598300930       O SHELL 2.2863528730 1.4381114240 2.2491612430
O CORE -2.3719210620 6.2627439500 10.6598300930       O CORE 8.0465822220 1.2609838250 2.2491612430
O SHELL -2.3719210620 6.2627439500 10.6598300930      O SHELL 8.0465822220 1.2609838250 2.2491612430
O CORE 1.3920561080 7.9599204060 10.6598300930        O CORE 5.3198647500 6.3380532260 2.2491612430
O SHELL 1.3920561080 7.9599204060 10.6598300930       O SHELL 5.3198647500 6.3380532260 2.2491612430
O CORE 2.3719213010 0.2379782350 4.4260101320         O CORE 7.5039520260 4.4504947660 14.7167959210
O SHELL 2.3719213010 0.2379782350 4.4260101320        O SHELL 7.5039520260 4.4504947660 14.7167959210
O CORE 9.0431442260 1.9351549150 4.4260101320         O CORE 2.8289823530 4.2733669280 14.7167959210
O SHELL 9.0431442260 1.9351549150 4.4260101320        O SHELL 2.8289823530 4.2733669280 14.7167959210
O CORE 4.2377352710 6.8640151020 4.4260101320         O CORE 5.3198652270 0.3132877350 14.7167959210
O SHELL 4.2377352710 6.8640151020 4.4260101320        O SHELL 5.3198652270 0.3132877350 14.7167959210
O CORE 7.5895209310 3.2503614430 16.8936443330        O CORE -3.7519760130 8.9856367110 18.2713165280
O SHELL 7.5895209310 3.2503614430 16.8936443330       O SHELL -3.7519760130 8.9856367110 18.2713165280
O CORE 3.8255436420 4.9475378990 16.8936443330        O CORE 4.4401774410 7.7936367990 18.2713165280
O SHELL 3.8255436420 4.9475378990 16.8936443330       O SHELL 4.4401774410 7.7936367990 18.2713165280
O CORE 4.2377347950 0.8392497900 16.8936443330        O CORE -0.6882014270 1.2950233220 18.2713165280
O SHELL 4.2377347950 0.8392497900 16.8936443330       O SHELL -0.6882014270 1.2950233220 18.2713165280
O CORE -3.7446713450 8.3114652630 10.3643474580       O CORE 5.9950227740 1.7688709500 12.0375003810
O SHELL -3.7446713450 8.3114652630 10.3643474580      O SHELL 5.9950227740 1.7688709500 12.0375003810
O CORE 3.8526754380 8.1243963240 10.3643474580        O CORE 5.9058022500 4.3074059490 12.0375003810
O SHELL 3.8526754380 8.1243963240 10.3643474580       O SHELL 5.9058022500 4.3074059490 12.0375003810
O CORE -0.1080044960 1.6384353640 10.3643474580       O CORE 3.7519760130 2.9608712200 12.0375003810
O SHELL -0.1080044960 1.6384353640 10.3643474580      O SHELL 3.7519760130 2.9608712200 12.0375003810
O CORE 6.5825247760 2.0996305940 4.1305270200         O CORE 1.4656234980 5.9732542040 5.8036837580
O SHELL 6.5825247760 2.0996305940 4.1305270200        O SHELL 1.4656234980 5.9732542040 5.8036837580
O CORE 5.3256044390 4.6508188250 4.1305270200         O CORE -0.7774226670 4.7812542920 5.8036837580
O SHELL 5.3256044390 4.6508188250 4.1305270200        O SHELL -0.7774226670 4.7812542920 5.8036837580
O CORE 3.7446703910 2.2866997720 4.1305270200         O CORE -0.6882014270 7.3197894100 5.8036837580
O SHELL 3.7446703910 2.2866997720 4.1305270200        O SHELL -0.6882014270 7.3197894100 5.8036837580
O CORE 1.3649243120 5.1120138170 16.5981616970        O CORE 0.0000000000 0.0000000000 1.5746622090
O SHELL 1.3649243120 5.1120138170 16.5981616970       O SHELL 0.0000000000 0.0000000000 1.5746622090
O CORE 0.1080037280 7.6632013320 16.5981616970        O CORE 5.2175998690 3.0123829840 14.0422964100
O SHELL 0.1080037280 7.6632013320 16.5981616970       O SHELL 5.2175998690 3.0123829840 14.0422964100
O CORE -1.4729284050 5.2990822790 16.5981616970       O CORE -0.0000000240 6.0247659680 7.8084788320
O SHELL -1.4729284050 5.2990822790 16.5981616970      O SHELL -0.0000000240 6.0247659680 7.8084788320
O CORE -0.1022648740 3.3256704810 8.4829769130        CA_F CORE 0.0000000000 0.0000000000 15.5184640880
O SHELL -0.1022648740 3.3256704810 8.4829769130       CA_F CORE 5.2175998690 3.0123829840 9.2846469880
O CORE -2.2863523960 7.4628772740 8.4829769130        CA_F CORE -0.0000000240 6.0247659680 3.0508301260
```

A.3.3   Input file structure

The following file creates the base slab by cleaving the 'reduced' unit cell in a given (hkl) direction. This is cleavage direction is defined in Line 15 (`miller h k l`).

```
1  TITLE
2   (h k l) plane of half bTCP w all Ca(4)
3  ENDS
4  CELL 10.435200 10.435200 18.70145 90.000000 90.000000 120.000000
5  BASIS
6  # Section B.2
7  ENDS
8
9  @include poten.txt # Section B.1
10 bulk
11 press.0
12 conp
13 rdf
14 slab
15 miller h k l
16 start
17 stackgen systematic
18 coord p core o shell 1.6
19 coord p core o core 1.6
20 split
21 bfgs 0
22 newt 0
23
24 start
25 stop
```

A.3.4   Interface structure commands

The use of Files A.3.1 and A.3.3 with the coordinates of Section A.3.2 create a number of possible terminations that can be considered for creating interface structures. The terminations are accessible as `staco.000` output files. For simplicity, the lowest energy termination `staco.000` file becomes the `input.txt` file for creating surface and grain boundary structures. The `staco.000` file requires slight modification following the section that defines the coordinates. These modifications are listed in the following sections:

      Surface creation. The lines below are added to the lowest energy termination `staco.000` file for creating surfaces. The constants `N`, `M`, `P`, `Q` are appropriately chosen to create orthogonal systems.

```
1  # Surface generation in metadise
2  @include poten.txt
3  surf
4  vscale1
5  N M
```

```
 6  P Q
 7  print dlpoly 1
 8  start
 9  minimise
10  conj 0
11  bfgs            0
12  newt            0
13  maxu           20
14  nokill
15  start
16  stop
```

Grain boundary creation. The lines below are added to perform a 2D-scan between the two bodies to determine the ideal displacement vector for energy minimizing the grain boundary interface.

```
 1  # Grid scan between two surfaces
 2  @include poten.txt
 3  bulk
 4  reflect
 5  displace 0 0 0
 6
 7  start
 8  scan
 9  conf
10  frac 0.1
11  conj 0
12  bfgs 5
13  newt 00
14  maxu 1
15  nokill
16  start
17
18  stop
```

The lines below are added to energy minimize the grain boundary interface, where Line 5 (`displace ## ## ##`) is the displacement vector determined from the grid scan.

```
 1  # Grid scan between two surfaces
 2  @include poten.txt
 3  bulk
 4  reflect
 5  displace ## ## ##
 6
 7  regchk
 8  start
 9  minimise
10  conj 0
11  bfgs 20
12  newt 600
13  maxu 20
```

```
14 nokill
15 start
16
17 stop
```

B | Python scripts

A series of functional Python scripts were developed during this thesis to aid in the processing and analysis of simulation results. Examples of the most vital code chunks are provided below.

B.1   Calculating bond lengths

Methodology for collecting bond distances between central atom (`a1Type`) and oxygen atoms (`type = 3`).

```python
import numpy as np

dict_bond = {}
for key in timestep:
    df_a1 = timestep[key][timestep[key]['type']==a1Type].reset_index(drop
     = True)
    df_a2 = timestep[key][timestep[key]['type']==3.].reset_index(drop =
    True)
    a1 = np.array(df_a1[['x','y','z']].values.tolist())
    a2 = np.array(df_a2[['x','y','z']].values.tolist())

    group = []
    tree = KDTree(a2,leaf_size = 2)
    for i in range(len(a1)):
        ind,dist = tree.query_radius(np.array([a1[i]]), r=5,
    return_distance = True)
        ind = ind[0].tolist()
        dist = dist[0].tolist()
        for j in range(len(dist)):
            group.append([df_a1['labels'].iat[i], df_a2['labels'].iat[ind
    [j]], dist[j]])
    group = pd.DataFrame(group, columns = ['a1','a2','d'])

    for a1label in df_a1['labels'].unique():
        if a1label in dict_bond: pass
```

```
22            else: dict_bond[a1label] = {}
23        for a2label in df_a2['labels'].unique():
24            if a2label in dict_bond[a1label]: pass
25            else:
26                dict_bond[a1label][a2label] = {}
27                dict_bond[a1label][a2label]['distances'] = []
28
29                t = group.loc[(group['a1'] == a1label) & (group['a2'] ==
   a2label)]
30                if t.shape[0] == 0: pass
31                else: dict_bond[a1label][a2label]['distances'].append(t)
32
33 for a1 in dict_bond:
34     for a2 in dict_bond[a1]:
35         if len(dict_bond[a1][a2]['distances']) == 0: pass
36         else:
37             dict_bond[a1][a2]['distances'] = pd.concat(dict_bond[a1][a2][
   'distances']).reset_index(drop = True)
```

B.2   Dopant incorporation

The script below is used to introduce dopants into surface structures created by METADISE.
The 50%-partial occupancy of the Ca(4) is maintained by randomly selecting half of the
`Ca_F` atoms to be vacant Ca(4) sites (`Ca_vac`) in layers through the bulk.

```
1 FILE,seedidx = os.path.join('surface.CONFIG'),1234567890
2
3 lines = open(FILE,'r').readlines()
4 xshift = float(lines[2].split()[1])
5 yshift = float(lines[3].split()[2])
6 zshift = float(lines[4].split()[0])
7
8 # Define dopant and dopant amount into the CONFIG file
9 values = ['Sr', 0.05]
10 random.seed(seedidx) # remove 'seedidx' for random generation
11
12 data = []
13 for i in range(5,len(lines)):
14     if i % 2 == 1:
15         if 'O(S)' in lines[i] : pass
16         else:
17             data.append([lines[i].split()[0].replace('CA','Ca')] + [float
   (thing) for thing in lines[i+1].split()])
18     else : pass
19 atomData = pd.DataFrame(data, columns = ['type','z','x','y'])
20 atomData['sub'] = atomData.type
21
22 select_occ = []
23 for k,v in atomData.loc[(atomData.type == 'Ca_F')].groupby(['z']):
```

130

```
24      select_idx = [v.iloc[x].name for x in random.sample(range(v.shape[0])
        ,int(0.5*v.shape[0]))]
25      select_occ += select_idx
26      atomData.loc[select_occ,'sub'] = 'Ca_vac'
27
28  a1 = atomData.loc[(atomData['sub'] != 'Ca_vac') & (atomData.type != 'P')
        & (atomData.type != 'O')]
29  select_dop = random.sample(a1.index.tolist(),int(len(a1)*values[1]))
30  atomData.loc[select_dop,'sub'] = 'Sr'
```

The script above requires slight modification for handling cif-file formats for grain boundary structures.

B.3   Determining interface properties

The following subroutines were used to analyze the MC simulations of the doped interfaces.

Listing B.1 – Subroutine for processing surface simulations

```
1  result = histories['result']
2  df_matrix = histories['matrix']
3
4  x,y = sns.distplot(result[(result.type == 'Sr')].z, bins = 100, kde =
       True, hist = True).get_lines()[0].get_data()
5  df1 = pd.DataFrame({'x':x,'y':y})
6
7  tot_mean = df1.y.mean() ; tot_std = df1.y.std()
8  bulk_mean = df1[np.abs(df1.x) < 0.2].y.mean()
9  bulk_std = df1[np.abs(df1.x) < 0.2].y.std()
10 intersect = df1[np.abs(df1.x).between(0.2,0.45)]
11 intersect = intersect.iloc[(intersect.y-(bulk_mean+bulk_std)).abs().
       argsort()[:40]].sort_values(by = 'x')
12 bound2 = intersect.x.iat[0]
13 bound1 = intersect.x.iat[-1]
14
15 dop = result[result.type == 'Sr']
16
17 surfA = dop[dop.z >= bound1]
18 depthA = (0.5 - bound1)*df_matrix.z.mean()
19 nA = surfA.shape[0]/df_matrix.shape[0]
20 volA = 0.001 * (df_matrix.x.mean()*df_matrix.y.mean()*depthA)
21
22 surfB = dop[dop.z <= bound2]
23 depthB = (bound2 + 0.5)*df_matrix.z.mean()
24 nB = surfB.shape[0]/df_matrix.shape[0]
25 volB = 0.001 * (df_matrix.x.mean()*df_matrix.y.mean()*depthB)
26
27 bulk = dop[dop.z.between(bound2,bound1)]
28 depthBulk = (bound1 - bound2)*df_matrix.z.mean()
29 nBulk = bulk.shape[0]/df_matrix.shape[0]
```

```
30  volBulk = 0.001 * (df_matrix.x.mean()*df_matrix.y.mean()*depthBulk)
31
32  conc_bulk = nBulk/volBulk
33  conc_surf = (nA+nB)/(volA+volB)
34  conc_A = nA/volA ; conc_B = nB/volB
35  names = ['conc_bulk','conc_surf','conc_A','conc_B','surf:bulk','A:bulk','
      B:bulk','depth_A','depth_B']
36  values = [conc_bulk,conc_surf,conc_A, conc_B, conc_surf/conc_bulk,conc_A/
      conc_bulk, conc_B/conc_bulk, depthA, depthB]
37  stats = pd.DataFrame([values], columns = names)
```

Listing B.2 – Subroutine for processing grain boundary simulations

```
1   result = histories[conc][rand]['result']
2   df_matrix = histories[conc][rand]['matrix']
3
4   x,y = sns.distplot(result[(result.type == 'Sr')].z, bins = 100, kde =
      True, hist = True).get_lines()[0].get_data()
5   df1 = pd.DataFrame({'x':x,'y':y})
6
7   bulk_mean = df1[np.abs(df1.x).between(0.15,0.35)].y.mean()
8   bulk_std = df1[np.abs(df1.x).between(0.15,0.35)].y.std()
9   intersect1 = df1[df1.x.between(-0.48,-0.01)]
10  intersect1 = intersect1.iloc[(intersect1.y-(bulk_mean+bulk_std)).abs().
      argsort()[:35]].sort_values(by = 'x')
11  intersect2 = df1[df1.x.between(0.01,0.48)]
12  intersect2 = intersect2.iloc[(intersect2.y-(bulk_mean+bulk_std)).abs().
      argsort()[:35]].sort_values(by = 'x')
13  bound1 = intersect1.x.iat[0] ; bound2 = intersect2.x.iat[-1]
14  bound3 = intersect1.x.iat[-1] ; bound4 = intersect2.x.iat[0]
15
16  dop = result[result.type == 'Sr']
17
18  gbA = dop[(dop.z <= bound1) | (dop.z >= bound2)]
19  depthA = (1 - bound2 + bound1)*df_matrix.z.mean()
20  nA = gbA.shape[0]/df_matrix.shape[0]
21  volA = 0.001 * (df_matrix.x.mean()*df_matrix.y.mean()*depthA)
22
23  gbB = dop[dop.z.between(bound3,bound4, inclusive = 'both')]
24  depthB = (bound4-bound3)*df_matrix.z.mean()
25  nB = gbB.shape[0]/df_matrix.shape[0]
26  volB = 0.001 * (df_matrix.x.mean()*df_matrix.y.mean()*depthB)
27
28  bulk = dop[dop.z.between(bound1,bound3) | dop.z.between(bound4,bound2)]
29  depthBulk = (bound3 - bound1) + (bound2 - bound4)
30  nBulk = bulk.shape[0]/df_matrix.shape[0]
31  volBulk = 0.001 * (df_matrix.x.mean()*df_matrix.y.mean()*(depthBulk *
      df_matrix.z.mean()))
32
33  conc_bulk = nBulk/volBulk
34  conc_gb = (nA+nB)/(volA+volB)
35  conc_A = nA/volA ; conc_B = nB/volB
```

```
36 names = ['conc_bulk','conc_gb','conc_A','conc_B','gb:bulk','A:bulk','B:
     bulk','depth_A','depth_B']
37 values = [conc_bulk,conc_gb,conc_A, conc_B, conc_gb/conc_bulk,conc_A/
     conc_bulk, conc_B/conc_bulk, depthA, depthB]
38 stats = pd.DataFrame([values], columns = names)
```

C Supplementary material: Sr-doped β-TCP

C.1 Calculated properties

Code B.1 determines various properties of the surface structures. One of these properties includes the interface depth, d_{interf}, summarized in Tables C.1. In this thesis, d_{interf} is defined as the point where dopant behavior deviates from bulk-like behavior.

Table C.1 – Determined interface depths, d_{interf}, of the $(1\,\overline{2}\,0)$ and $(1\,0\,0)$ surfaces doped with various Sr content.

Sr content [%]	$(1\,\overline{2}\,0)$		$(1\,0\,0)$	
	Surf-A	Surf-B	Surf-A	Surf-B
1.00	7.5446	7.8566	4.6371	6.6610
1.71	6.4025	9.3298	7.1098	10.9387
2.92	6.1001	6.7161	6.3709	8.0315
5.00	6.2257	6.6856	3.8707	11.9430
10.00	6.2282	6.7011	9.2413	7.7658
20.00	6.0318	6.7073	4.3533	7.4055
40.00	4.6037	5.9667	4.2655	4.2604

Sr content [%]	$(1\,\overline{2}\,0)$		$(1\,0\,0)$	
	GB-A	GB-B	GB-A	GB-B
1.00	10.9164	12.2156	12.7849	6.8339
1.71	11.7909	6.1115	6.1148	5.5813
2.92	19.6262	6.1143	5.2412	4.3934
5.00	11.1460	5.2366	3.8208	3.8108
10.00	11.1809	8.7469	2.2262	2.9517
20.00	13.9174	8.7779	2.1848	1.8724
40.00	7.9103	4.4296	1.0895	1.2540

Once the interface depths are defined, dopant concentrations can be calculated for given regions of interest, summarized in Table C.2.

Table C.2 – Determined χ_{region} values of the $(1\,\bar{2}\,0)$ and $(1\,0\,0)$-interfaces.

(hkl)	Sr content [%]	χ_{region} [Sr at. nm^{-3}]				Surf:Bulk
		Bulk	Surf	Surf-A	Surf-B	
	1.00	0.06	0.64	0.45	0.83	10.95
	1.71	0.11	0.95	0.89	0.99	9.07
	2.92	0.25	1.61	1.38	1.82	6.44
$(1\,\bar{2}\,0)$	5.00	0.44	2.88	2.38	3.34	6.55
	10.00	1.00	5.06	4.52	5.55	5.06
	20.00	2.52	6.64	7.88	5.53	2.64
	40.00	5.68	8.57	7.62	9.29	1.51
	1.00	0.03	0.93	1.31	0.67	34.27
	1.71	0.05	0.92	0.94	0.90	17.72
	2.92	0.12	1.88	1.90	1.87	16.30
$(1\,0\,0)$	5.00	0.30	2.73	5.02	2.00	9.16
	10.00	0.83	4.24	3.84	4.71	5.12
	20.00	2.50	6.44	5.43	7.03	2.58
	40.00	5.73	8.13	7.29	8.96	1.42

(hkl)	Sr content [%]	χ_{region} [Sr at. nm^{-3}]				GB:Bulk
		Bulk	GB	GB-A	GB-B	
	1.00	0.14	0.34	0.51	0.19	2.46
	1.71	0.24	0.68	0.79	0.46	2.89
	2.92	0.40	0.92	0.94	0.85	2.28
$(1\,\bar{2}\,0)$	5.00	0.74	1.65	1.75	1.43	2.23
	10.00	1.52	2.51	2.84	2.09	1.65
	20.00	3.11	3.95	4.08	3.73	1.27
	40.00	6.12	7.26	6.70	8.26	1.19
	1.00	0.06	0.59	0.77	0.41	9.71
	1.71	0.13	0.75	0.79	0.72	5.87
	2.92	0.29	1.38	1.50	1.26	4.82
$(1\,0\,0)$	5.00	0.52	1.99	1.99	1.99	3.82
	10.00	1.19	3.04	2.65	3.51	2.56
	20.00	2.67	5.29	5.84	5.01	1.98
	40.00	6.00	6.86	6.54	7.52	1.14

C.2   Enthalpy of segregation calculation details

The $n\Delta H_{\mathrm{b}}$ term can be evaluated from the bulk energetics trend as a function of strontium content, shown in Figure C.1.

Figure C.1 – Energy of the bulk system
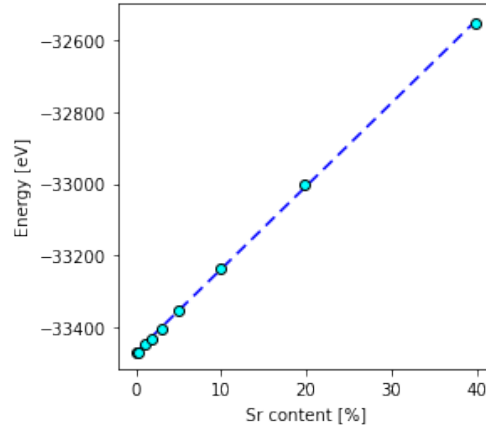
The fitted slope, m_{bulk}, of the linear regression can be equated to the $n\Delta H_{\mathrm{b}}$ term with the following expression:

$$n\Delta H_{\mathrm{b}} = [\mathrm{conc} \times m_{\mathrm{bulk}}] \times \frac{n_{\mathrm{surf}}}{n_{\mathrm{bulk}}} \tag{C.1}$$

$$= [4.9603 \times 23.14] \times \frac{8}{16} \tag{C.2}$$

$$= 57.3896 \tag{C.3}$$

The benefit of this method is that the $n\Delta H_{\mathrm{b}}$ term can accurately be evaluated for the precise concentration of the system.

C.3 Microscopy details

Table C.3 – X-ray energies [keV] of K- and L-emission lines, with possible source

	Kα	Kβ	Lα	Lβ	Lγ	Source
C	0.277					FIB
O	0.535					Plasma Biotal
F	0.535					Unknown
Na	1.041	1.071				Plasma Biotal
Mg	1.254	1.302				Plasma Biotal
Al	1.487	1.557				Vacuum chamber (?)
Si	1.740	1.836				SDD
P	2.014	2.139				Plasma Biotal
Ca	3.692	4.013				Plasma Biotal
Fe	6.404	7.649	0.705	0.719		Unknown
Cu	8.048	8.905	0.930	0.950		Half-grid
Ga	9.252	10.264	1.098	1.125		FIB process
Sr	14.165	15.836	1.807	1.872		Plasma Biotal
Zr	15.775	17.667	2.042	2.124	2.303	Collimator
Pb			10.552	12.614	14.764	SDD

Bibliography

1. Bauer, T. W. & Muschler, G. F. Bone Graft Materials An Overview of the Basic Science. *Clinical Orthopaedics and Related Research* **4,** 201–213 (2000).

2. Banwart, J. C., Asher, M. A. & Hassanein, R. S. Iliac crest bone graft harvest donor site morbidity. A statistical evaluation. *Spine* **20,** 1055–1060 (1995).

3. Linhart, W., Briem, D., Amling, M., Rueger, J. M. & Windolf, J. Mechanical failure of a porous hydroxyapatite ceramic 7.5 years after treatment of a fracture of the proximal tibia. *Unfallchirurg* **107,** 154–157 (2004).

4. Van Hemert, W. L. W., Willems, K., Anderson, P. G., van Heerwaarden, R. J. & Wymenga, A. B. Tricalcium phosphate granules or rigid wedge preforms in open wedge high tibial osteotomy: a radiological study with a new evaluation system. *Knee* **11,** 451–456 (2004).

5. LeGeros, R. Z. Biodegradation and bioresorption of calcium phosphate ceramics. *Clinical Materials* **14,** 65–88 (1993).

6. Kalita, S. J., Bhatt, H. A. & Dhamne, A. A MgO-Na2O-P2O5-based sintering additives of tricalcium phosphate bioceramics. *Journal of the American Ceramic Society* **89,** 875–881 (2006).

7. Bhatt, H. A. & Kalita, S. J. Influence of oxide-based sintering additives on densification and mechanical behavior of tricalcium phosphate (TCP). *Journal of Materials Science: Materials in Medicine* **18,** 883–893 (2007).

8. Groot, K. D. Effect of porosity and physicochemical properties on the stability, resorption, and strength of calcium phosphate ceramics. *Annals of the New York Academy of Sciences* **523,** 227–233 (1988).

9. Koerten, H. K. & van der Meulen, J. Degradation of calcium phosphate ceramics. *Journal of Biomedical Materials Research* **44,** 78–86 (1999).

10. Seo, D. S., Hwang, K. H. & Lee, J. K. Particle loosening on the surface of dense hydroxyapatite in water. *Applied Mechanics and Materials* **217-219,** 983–987 (2012).

11. Carlisle, E. M. Silicon: a possible factor in bone calcification. *Science* **167,** 279–280 (1970).

12. Pietak, A. M., Reid, J. W., Stott, M. J. & Sayer, M. Silicon substitution in the calcium phosphate bioceramics. *Biomaterials* **28,** 4023–4032 (2007).

13. Bohner, M. Silicon-substituted calcium phosphates - a critical view. *Biomaterials* **30,** 6403–6406 (2009).

14. Gasquères, G. *et al.* Revisiting silicate substituted hydroxyapatite by solid-state NMR. *Magnetic Resonance in Chemistry* **46,** 342–346 (2008).

15. Hayakawa, S. *et al.* Heterogeneous structure and in vitro degradation behavior of wet-chemically derived nanocrystalline silicon-containing hydroxyapatite particles. *Acta Biomaterialia* **9,** 4856–4867 (2013).

16. Balas, F., Pérez-Pariente, J. & Vallet-Regí, M. In vitro bioactivity of silicon-substituted hydroxyapatites. *Journal of Biomedical Materials Research* **66A,** 364–375 (2003).

17. Putlayev, V., Veresov, A., Pulkin, M., Soin, A. & Kuznetsov, V. Silicon-substituted hydroxyapatite ceramics (Si-HAp): Densification and grain growth through the prism of sintering theories. *Materialwissenschaft und Werkstofftechnik* **37,** 416–421 (2006).

18. Bojarski, S. A., Stuer, M., Zhao, Z., Bowen, P. & Rohrer, G. S. Influence of Y and La additions on grain growth and the grain boundary character distribution of alumina. *Journal of the American Ceramic Society* **97,** 622–630 (2014).

19. Santoni, B. L. G. *Ion-doped grain boundaries to control the dissolution as well as the osteoclastic and macrophage response of sintered calcium phosphate ceramics* PhD thesis (University of Bern, 2020).

20. Watson, G. W., Parker, S. C. & Kresse, G. Ab initio calculation of the origin of the distortion of α-PbO. *Physical Review B* **59,** 8481–8486 (13 1999).

21. LAMMPS: Large-scale Atomic/Molecular Massively Parallel Simulator. http://lammps.sandia.gov (2017).

22. Brukhno, A. V. *et al.* DL_MONTE: a multipurpose code for Monte Carlo simulation. *Molecular Simulation* **47,** 131–151 (2019).

23. Purton, J. A., Crabtree, J. C. & Parker, S. C. DL_MONTE: a general purpose program for parallel Monte Carlo simulation. *Molecular Simulation* **39,** 1240–1252 (2013).

24. Metropolis, N., Rosenbluth, A. W., Rosenbluth, M. N. & Teller, A. H. Equation of State Calculations by Fast Computing Machines. *Journal of Chemical Physics* **21,** 1087–1092 (1953).

25. Swendsen, R. H. & Wang, J.-S. Replica Monte Carlo simulation of spin glasses. *Physical Review Letters* **57,** 2607–2609 (1986).

26. Hansmann, U. H. E. Parallel tempering algorithm for conformational studies of biological molecules. *Chemical Physics Letters* **281,** 140–150 (1997).

27. Egerton, R. F. Control of radiation damage in TEM. *Ultramicroscopy* **127,** 100–108 (2013).

28. Yashima, M., Sakai, A., Kamiyama, T. & Hoshikawa, A. Crystal structure analysis of β-tricalcium phosphate $Ca_3(PO_4)_2$ by neutron powder diffraction. *Journal of Solid State Chemistry* **175,** 272–277 (2003).

29. Dickens, B., Schroeder, L. W. & Brown, W. E. Crystallographic Studies of the Role of Mg as a Stabilizing Impurity in β-$Ca_3(PO_4)_2$. *Journal of Solid State Chemistry* **10,** 232–248 (1974).

30. Demichelis, R. *et al.* Simulation of Calcium Phosphate Species in Aqueous Solution: Force Field Derivation. *Journal of Physical Chemistry B* **122,** 1471–1483 (2018).

31. Polak, E. & Ribiere, G. Note on the convergence of conjugate direction methods. *ESAIM: Mathematical Modeling and Numerical Analysis - Mathematical Modeling and Numerical Analysis* **3,** 35–43 (1969).

32. Hoover, W. G. Canonical dynamics: Equilibrium phase-space distributions. *Physical Review A* **31,** 1695–1697 (1985).

33. Martyna, G. J., Tobias, D. J. & Klein, M. L. Constant pressure molecular dynamics algorithms. *Journal of Chemical Physics* **101,** 4177–4189 (1994).

34. Jay, E. E., Mallinson, P. M., Fong, S. K., Metcalfe, B. L. & Grimes, R. W. Partitioning of dopant cations between β-tricalcium phosphate and fluorapatite. *Journal of Nuclear Materials* **414,** 367–373 (2011).

35. Matsunaga, K., Kubota, T., Toyoura, K. & Nakamura, A. First-principles calculations of divalent substitution of Ca^{2+} in tricalcium phosphates. *Acta Biomaterialia* **23,** 329–337 (2015).

36. Liang, L., Rulis, P. & Ching, W. Y. Mechanical properties, electronic structure and bonding of α- and β-tricalcium phosphate with surface characterization. *Acta Biomaterialia* **6,** 3763–3771 (2010).

37. Yin, X., Stott, M. J. & Rubio, A. α- and β-tricalcium phosphate: a density functional study. *Physical Review B* **68,** 205205 (2003).

38. Santoni, B. L. G. *et al.* Chemically pure β-tricalcium phosphate powders: Evidence of two crystal structures. *Journal of the European Ceramic Society* **41,** 1683–1694 (2021).

39. Nosé, S. A united formulation of the constant temperature molecular dynamics methods. *Journal of Chemical Physics* **81,** 511–519 (1984).

40. Silverman, B. W. *Density Estimation for Statistics and Data Analysis* (Chapman and Hall CRC, London, 1986).

41. Ester, M., Kriegel, H.-P., Sander, J. & Xu, X. *A Density-based algorithm for discovering clusters in large spatial databases with noise* in (1996), 226–231.

42. Billinge, S. J. L. The rise of the X-ray atomic pair distribution function method: a series of fortunate events. *Philosophical Transactions of the Royal Society A* **377,** 20180413 (2019).

43. Plattner, N. *et al.* An infinite swapping approach to rare-event sampling problems. *Journal of Chemical Physics* **135,** 134111 (2011).

44. Kofke, D. A. On the acceptance probability of replica-exchange Monte Carlo trials. *Journal of Chemical Physics* **117,** 6911 (2002).

45. Swendsen, R. H. & Wang, J.-S. Replica Monte Carlo simulation of spin glasses. *Physical Review Letters* **57,** 2607–2609 (1986).

46. Hukushima, K. & Nemoto, K. Exchange Monte Carlo Method and Application to Spin Glass Simulations. *Journal of the Physical Society of Japan* **65,** 1604–1608 (1996).

47. Tesi, M. C., van Rensburg, E. J. J., Orlandini, E. & Whittington, S. G. Monte carlo study of the interacting self-avoiding walk model in three dimensions. *Journal of Statistical Physics* **82,** 155–181 (1996).

48. Lapczyna, H. *et al.* Effect of grain size and microporosity on the in vivo behavior of β-tricalcium phosphate scaffolds. *European Cells and Materials* **28,** 299–319 (2014).

49. Sözen, T., Özışık, L. & Başaran, N. Ç. An overview and management of osteoporosis. *European Journal of Rheumatology* **4,** 46–56 (2017).

50. Marie, P. J. Strontium ranelate: a dual mode of action rebalancing bone turnover in favour of bone formation. *Current Opinion in Rheumatology* **18,** S11–S15 (2006).

51. Teitelbaum, S. L. Bone resorption by osteoclasts. *Science* **289,** 1504–1508 (2000).

52. Ammann, P. Strontium ranelate: a novel mode of action leading to renewed bone quality. *Osteoporosis International* **16,** S11–S15 (2005).

53. Neuprez, A., Hiligsmann, M., Scholtissen, S., Bruyere, O. & Reginster, J.-Y. Strontium ranelate: the first agent of a new therapeutic class in osteoporosis. *Advances in Therapy* **25,** 1235–1256 (2008).

54. Marie, P. J., Felsenberg, D. & Brandi, M. L. How strontium ranelate, via opposite effects on bone resorption and formation, prevents osteoporosis. *Osteoporosis International* **22,** 1659–1667 (2011).

55. Saidak, Z. & Marie, P. J. Strontium signaling: molecular mechanisms and therapeutic implications in osteoporosis. *Pharmacology & Therapeutics* **136,** 216–226 (2012).

56. Kaygili, O. *et al.* Strontium substituted hydroxyapatites: Synthesis and determination of their structural properties, in vitro and in vivo performance. *Materials Science and Engineering C* **55,** 538–546 (2015).

57. Capuccini, C. *et al.* Strontium-substituted hydroxyapatite coatings synthesized by pulsed-laser deposition: In vitro osteoblast and osteoclast response. *Acta Biomaterialia* **4,** 1885–1893 (2008).

58. Raucci, M. G., Giugliano, D., Alvarez-Perez, M. A. & Ambrosio, L. Effects on growth and osteogenic differentiation of mesenchymal stem cells by the strontium-added sol–gel hydroxyapatite gel materials. *Journal of Materials Science: Materials in Medicine* **26,** 90 (2015).

59. Glenske, K. *et al.* Applications of metals for bone regeneration. *International Journal of Molecular Sciences* **19,** 826 (2018).

60. Banerjee, S. S., Tarafder, S., Davies, N. M., Bandyopadhyaya, A. & Bose, S. Understanding the influence of MgO and SrO binary doping on mechanical and biological properties of b-TCP ceramics. *Acta Biomaterialia* **6,** 4167–4174 (2010).

61. Bose, S., Tarafder, S., Banerjee, S. S., Davies, N. M. & Bandyopadhyay, A. Understanding in vivo response and mechanical property variation in MgO, SrO and SiO2 doped b-TCP. *Bone* **48,** 1282–1290 (2011).

62. Pedone, A. *et al.* An ab initio parameterized interatomic force field for hydroxyapatite. *Journal of Materials Chemistry* **17,** 2061–2068 (2007).

63. Rabone, J. A. L. & de Leeuw, N. H. Interatomic potential models for natural apatite crystals: Incorporating strontium and the lanthanides. *Journal of Computational Chemistry* **27,** 253–266 (2006).

64. Boanini, E. *et al.* Strontium and Zinc Substitution in β-Tricalcium Phosphate: An X-ray Diffraction, Solid State NMR and ATR-FTIR Study. *Journal of Functional Biomaterials* **10,** 20 (2019).

65. Bigi, A., Foresti, E., Gandolfi, M., Gazzano, M. & Roveri, N. Isomorphous substitutions in b-tricalcium phosphate: the different effects of zinc and strontium. *Journal of Inorganic Biochemistry* **66,** 259–265 (1997).

66. Zachariasen, W. H. The crystal structure of the normal orthophosphates of barium and strontium. *Acta Crystallographica* **1,** 263–265 (1948).

67. Tao, J. *et al.* Controls of tricalcium phosphate single-crystal formation from its amorphous precursor by interfacial energy. *Crystal Growth & Design* **9,** 3154–3160 (2009).

68. Bohner, M., Santoni, B. L. G. & Döbelin, N. β-tricalcium phosphate for bone substitution: Synthesis and properties. *Acta Biomaterialia* **113,** 23–41 (2020).

69. Santoni, B. L. *et al.* Effect of minor amounts of β-calcium pyrophosphate and hydroxyapatite on the physico-chemical properties and osteoclastic resorption of β-tricalcium phosphate cylinder. *Bioactive Materials,* 1–14 (2021).

70. Bozic, K. J. *et al.* The epidemiology of revision total knee arthroplasty in the United States. *Clinical Orthopaedics and Related Research* **468,** 45–51 (2010).

71. Oussedik, S., Gould, K., Stockley, I. & Haddad, F. S. Defining peri-prosthetic infection: do we have a workable gold standard? *Journal of Bone and Joint Surgery, British volume* **94,** 1455–1456 (2012).

72. Jafari, S. M., Coyle, C., Mortazavi, S. M. J., Sharkey, P. F. & Parvizi, J. Revision hip arthroplasty: infection is the most common cause of failure. *Clinical Orthopaedics and Related Research* **468,** 2046–2051 (2010).

73. Le, D. H., Goodman, S. B., Maloney, W. J. & Huddleston, J. I. Current modes of failure in TKA: infection, instability, and stiffness predominate. *Clinical Orthopaedics and Related Research* **472,** 2197–2200 (2014).

74. Bozic, K. J. *et al.* The epidemiology of revision total hip arthroplasty in the United States. *Journal of Bone and Joint Surgery, American volume* **91,** 128–133 (2009).

75. Costerton, J. W., Stewart, P. S. & Greenberg, E. P. Bacterial biofilms: a common cause of persistent infections. *Science* **284,** 1318–1322 (1999).

76. Hall-Stoodley, L., Costerton, J. W. & Stoodley, P. Bacterial biofilms: from the natural environment to infectious diseases. *Nature Reviews Microbiology* **2,** 95–108 (2004).

77. Kargupta, R. *et al.* Coatings and surface modifications imparting antimicrobial activity to orthopedic implants. *WIREs Nanomedicine and Nanobiotechnology* **6,** 475–495 (2014).

78. Knetsch, M. L. W. & Koole, L. H. New strategies in the development of antimicrobial coatings: the example of increasing usage of silver and silver nanoparticles. *Polymers* **3,** 340–366 (2011).

79. Simchi, A., Tamjid, E., Pishbin, F. & Boccaccini, A. R. Recent progress in inorganic and composite coatings with bactericidal capability for orthopaedic applications. *Nanomedicine* **7,** 22–39 (2011).

80. Sen, C. K. *et al.* Copper-induced vascular endothelial growth factor expression and wound healing. *American Journal of Physiology-Heart and Circulatory Physiology* **282,** H1821–H1827 (2002).

81. Spaeth, K., Goetze-Neunhoeffer, F. & Hurle, K. Cu^{2+} doped β-tricalcium phosphate: Solid solution limit and crystallographic characterization by rietveld refinement. *Journal of Solid State Chemistry* **285,** 121225 (2020).

82. Kumar, P. N., Boovarasan, M., Singh, R. K. & Kannan, S. Synthesis, structural analysis and fabrication of coatings of the Cu^{2+} and Sr^{2+} co-substitutions in β-$Ca_3(PO_4)_2$. *RSC Advances* **3,** 22469–22479 (2013).

83. Enderle, R., Goetz-Neunhoeffer, F., Goebbels, M., Mueller, F. A. & Greil, P. Influence of magnesium doping on the phase transformation temperature of β-TCP ceramics examined by Rietveld refinement. *Biomaterials* **26,** 3379–3384 (2005).

84. Gomes, S., Nedelec, J.-M., Jallot, E., Sheptyakov, D. & Renaudin, G. Unexpected mechanism of Zn^{2+} insertion in calcium phosphate bioceramics. *Chemistry of Materials* **23,** 3072–3085 (2011).

85. Matsumoto, N., Sato, K., Yoshida, K., Hashimoto, K. & Toda, Y. Preparation and characterization of β-tricalcium phosphate co-doped with monovalent and divalent antibacterial metal ions. *Acta Biomaterialia* **5,** 3157–3164 (2009).

Gabrielle Anne Sblendorio · Lausanne, CH · glsblendorio@gmail.com

Education

École Polytechnique Fédérale de Lausanne (EPFL) - Lausanne, CH — Nov. 2021
PhD in Materials Science and Engineering
Dissertation: Atomistic simulation and electron microscopy to characterize grain boundaries in ion-doped β-tricalcium phosphate ceramics

University of California, Berkeley - Berkeley, CA — May 2016
M.Eng in Nuclear Engineering

University of San Francisco (USF) - San Francisco, CA — May 2015
B.S. in Physics and Chemistry (dual degree), Minor in Mathematics

Experience

Powder Technology Laboratory, EPFL — 2017 - Present · Lausanne, CH
Graduate Researcher for Prof. Paul Bowen
- Performed molecular dynamics and Monte Carlo simulations to investigate the behavior of ion-doped ceramics for biomedical applications.
- Utilized Python to automate data pipeline, and achieved a tenfold increase in speed.
- STEM-EDX measurements were correlated to atomistic simulation results to validate predictive capabilities of the developed computational framework.
- Deliverables: 2 international conferences, 3 co-author, 2 manuscripts currently in preparation

Fixate IO, LLC — 2020-Present · Remote
Subject Matter Expert
- Co-authored technical content on programming with Python, including various machine learning algorithms, in an academic and scientific context.

Positron Dynamics, Inc. — 2016 - 17 · Livermore, CA
Lead Engineer
- Oversaw multiple experiments with novel geometries of semiconductor materials to test positron moderation efficiency for antimatter cooling and capture.
- Designed and maintained a time-of-flight mass spectrometer to characterize the formation of deuterium clusters.
- Fabricated custom containment vessels for radioactive materials using 3D CAD and CNC milling.
- Co-authored proposals for grants and small business vouchers resulting in $200,000 investment.

Lawrence Berkeley National Laboratory — 2012 - 15 · Berkeley, CA
Undergraduate Researcher for Prof. Giovanni Meloni
- Operated and analysed mass spectrometry experiments to identify biofuel reaction products and intermediates.
- Selected as the only undergraduate researcher to conduct experiments at the Paul Scherrer Institute to characterise biofuel reaction pathways.
- Performed DFT calculations and electronic structure modelling to correlate identified products to reaction pathway.

Skills and Interests

Computational: Python, R, Matlab, molecular dynamics (LAMMPS), Monte Carlo (DLMONTE), DFT, Bash scripting
Technical: microscopy (SEM, TEM, EDX, FIB), mass spectrometry (TOF, PEPICO), 3D CAD (Fusion360), CNC milling, UHV vacuum maintenance, analog signal processing, rapid prototyping

Honors and Awards

1st Place innosuise Business Concept Pitch, EPFL Innovation Park, May 2018
Big Ideas@Berkeley Finalist, University of California, Berkeley, April 2016
Innovations and Entrepreneurship Award in Chemistry, NovaBay Pharma and USF, May 2014